APPLIED COMPUTATIONAL ELECTROMAGNETICS SOCIETY JOURNAL

Novel CEM/Hybrid/Intelligent Methods and their Applications

Guest Editors:

Bin Wei, Xidian University, China
Li-Xia Yang, Anhui University, China
Zheng-Yu Huang, Nanjing University of Aeronautics and Astronautics, China

February 2025
Vol. 40 No. 2
ISSN 1054-4887

The ACES Journal is abstracted in INSPEC, in Engineering Index, DTIC, Science Citation Index Expanded, the Research Alert, and to Current Contents/Engineering, Computing & Technology.

The illustrations on the front cover have been obtained from the ARC research group at the Department of Electrical Engineering, Colorado School of Mines

Published, sold and distributed by: River Publishers, Alsbjergvej 10, 9260 Gistrup, Denmark

FEBRUARY 2025 REVIEWERS

Billel Bentouhami
Zheng-Yu Huang
Ulrich Jakobus
Ming Jin
Chunyu Li
Singaram Manokaran
Edis Mekic
Michel M. Ney
Andrew Peterson
Kannadhasan S.
Ehsan Akbari Sekehravani
Manthan Shah
Chaofan Shi
Siyu Yang
Erdem Yazgan
Xiaoyan Zhang
Xuanru Zhang

THE APPLIED COMPUTATIONAL ELECTROMAGNETICS SOCIETY JOURNAL

Vol. 40 No. 2 February 2025

TABLE OF CONTENTS

Introduction to the Special Issue

Novel CEM/Hybrid/Intelligent Methods and their Applications

Guest Editors:

Bin Wei, Xidian University, China

Li-Xia Yang, Anhui University, China

Zheng-Yu Huang, Nanjing University of Aeronautics and Astronautics, China

Welcome to the special issue of Applied Computational Electromagnetics Society Journal (ACES). The papers included here are related to the novel computational electromagnetic (CEM) methods, hybrid methods, intelligent computing methods and their applications.

Higher-order Method of Moments Analysis of Waveguide with Irregular Cross-sections

Ning Ding[1,2], Zhongchao Lin[1,2], Lei Yin[1,2], Xunwang Zhao[1,2], and Yu Zhang[1,2]

[1]School of Electronic Engineering
Xidian University, Xi'an 71000, China

[2]Shaanxi Key Laboratory of Large-Scale Electromagnetic Computing
Xi'an 71000, China
nding@stu.xidian.edu.cn, zclin@xidian.edu.cn, yyparrot@126.com, xdzxw@126.com, yuseexidian@163.com

***Abstract* –** Antennas fed by waveguides with irregular cross-sections are efficiently simulated through the hybridization of the mode-matching (MM) method and the higher-order method of moments (HOMoM). To obtain the waveguide modes required in the MM method, a 2-D finite element method (FEM) is utilized and combined with the hybrid MM/HOMoM method, which enables the proposed method to model irregular waveports. The accuracy and efficiency of the proposed method are demonstrated by simulating log-periodic antennas (LPAs) and an asymmetric single-ridge slot waveguide antenna.

***Index Terms* –** Eigenvalues, finite element method (FEM), higher-order method of moments (HOMoM), irregular cross-sections, mode-matching (MM), waveports.

I. INTRODUCTION

Waveguides are widely used in antennas due to their high power capabilities and low loss properties. With the development of microwave technology, the structures of microwave devices and waveport aperture surfaces tend to become increasingly complicated. Therefore, the accurate and efficient simulation of microwave devices with waveports has attracted much attention.

For the analysis of waveguide problems, the method of moments (MoM) is widely considered numerically accurate [1]. On the other hand, due to the high efficiency of the mode-matching (MM) method, it has been widely used to design waveguide components. As a result, the MoM and MM method are hybridized to analyze waveguide coupling and radiation problems [2]. In 2000, the MM/MoM hybrid method was applied to analyze the metallic N-port waveguide structures, where the RWG basis functions were used for modeling, and the electric field integral equation (EFIE) was adopted for construction of the impedance matrix [3]. The Piggio-Miller-Chang-Harrington-Wu-Tsai (PMCHWT) formulation was utilized for analyzing dielectric loaded waveguides [4]. Later, the higher-order vector basis functions modeled with curvilinear triangles were used to improve the simulation efficiency of non-rotationally symmetric structures [5]. In 2015, the MM method was introduced to the higher-order method of moments (HOMoM) for constructing perfectly matching terminators for waveports. The higher-order basis functions modeled with quadrilaterals further reduced the number of unknowns [6]. Recently, a set of coupled integral formulations were derived to handle the loading problem of the metal-dielectric composite structures, and the orders of the basis functions were adaptively adjusted, yielding accurate and effective results [7].

However, the majority of previous investigations focused on regular waveguides, such as rectangular and circular ones. The previous method is no longer applicable when the cross-section of the waveport becomes irregular due to fabrication or architectural requirements, e.g. the coaxial center conductor may be eccentric or non-cylindrical [8]. Therefore, modeling of waveguides with irregular cross-sections based on the hybrid MM/MoM method is worth discussing.

In this paper, the MM/HOMoM method and FEM are hybridized to solve the coupling and radiation problems fed by waveports with irregular cross-sections. The use of higher-order basis function defined on the bilinear quadrilaterals can greatly improve efficiency while maintaining numerical accuracy, and the adoption of FEM extends the flexibility.

II. THEORY AND FORMULATION

A. MM/HOMoM hybrid method

Let us consider an arbitrarily shaped cavity containing several objects connected by N waveports, as depicted in Fig. 1. The object surfaces are classified into three categories: metallic, dielectric, and composite metal-dielectric surfaces [9].

Submitted On: May 29, 2023
Accepted On: October 15, 2024

https://doi.org/10.13052/2025.ACES.J.400201

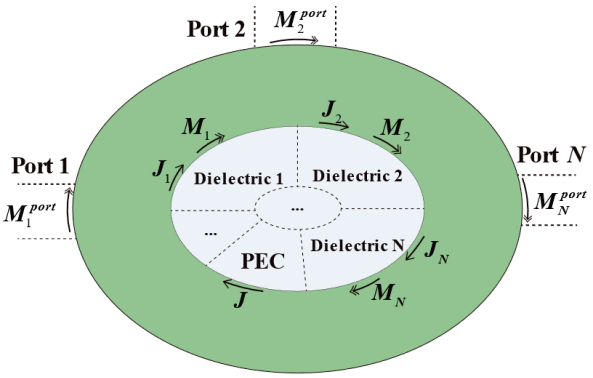

Fig. 1. Multiport cavity structure containing composite objects connected by N waveports.

The unknown current densities are expanded by a set of linearly independent basis functions $\boldsymbol{f}_n$ and $\boldsymbol{g}_n$ as:

$$\begin{cases} \boldsymbol{J}^l = \sum_{n=1}^{N_J} \alpha_n \boldsymbol{f}_n & \text{metal/dielectric surfaces} \\ \boldsymbol{M}^l = \sum_{n=1}^{N_M} \beta_n \boldsymbol{f}_n & \text{dielectric surfaces} \\ \boldsymbol{M}^{port} = \sum_{n=1}^{N_p} \eta_0 \nu_n \boldsymbol{g}_n & \text{waveguide apertures} \end{cases}, \quad (1)$$

where η_0 denotes the wave impedance of free space, and N_J, N_{M}, and N_p represent the number of unknowns in the scattering body and waveguide apertures, respectively. α_n, β_n, and ν_n represent the unknown coefficients. $\boldsymbol{f}_n$ is the higher-order basis functions defined on the quadrilaterals, and the definition is given in [10]. $\boldsymbol{g}_n$ denotes the waveguide basis functions defined on the apertures of waveguides, which is expanded using the eigenvectors of different waveport modes.

Since the analysis of conventional scattering problems has been discussed in detail previously [9, 11], this paper discusses only the matrix associated with the waveguide basis functions. According to the equivalence principle, the surface integral equation of the electromagnetic field could be established. The integral equations can be written as follows by applying boundary conditions to the waveguide apertures, the metallic surfaces, and the dielectric surfaces, respectively:

$$\begin{cases} \hat{\mathbf{n}}_i \times \boldsymbol{E}_i = \hat{\mathbf{n}}_i \times \sum_{j=1}^{\infty} [\eta_0 L(\boldsymbol{J}_j) - K(\boldsymbol{M}_j)] = -\zeta \boldsymbol{M}_i \\ \hat{\mathbf{n}}_i \times \boldsymbol{H}_i = \boldsymbol{J}_i \end{cases}, \quad (2)$$

where the real number ζ equals 1.0 when modeling the dielectric surfaces or waveguide apertures and 0 otherwise. The integral operators L and K are the same as [6]. $\boldsymbol{J}_i$ and $\boldsymbol{M}_i$ denote the electric and magnetic currents defined on the i-th surface of the elements, which are discretized with the higher-order basis functions defined on bilinear quadrilateral elements, and $\hat{\mathbf{n}}_i$ (i = 1,2,3 ...) is the unit normal vector on the i-th surface.

Adopting the MM technique, the electromagnetic field outside the waveport can be written as [6]:

$$\begin{cases} E^{port} = -\sum_{i=1}^{\infty} \boldsymbol{e}_i \int_A (\hat{\mathbf{n}} \times \boldsymbol{e}_i) \cdot \boldsymbol{M}\, ds \\ H^{port} = \frac{2\hat{\mathbf{n}} \times \boldsymbol{e}_j}{\eta_j} + \sum_{i=1}^{\infty} \frac{\hat{\mathbf{n}} \times \boldsymbol{e}_i}{\eta_i} \int_A (\hat{\mathbf{n}} \times \boldsymbol{e}_i) \cdot \boldsymbol{M}\, ds \end{cases}, \quad (3)$$

where $\hat{\mathbf{n}}$ is the outer normal vector for each waveport, $\boldsymbol{e}_i$ is the normalized eigenvector of the waveport, $\boldsymbol{e}_j$ is the excitation mode, and η_i is the wave impedance of the i-th mode of the waveport.

The whole structure is divided into the scattering body (represented by s) and waveports (denoted by p). Using Galerkin's method to test the above equation with the basis functions of the scatterer body and the basis functions of the waveports, the integral equations of matrix form can be written as:

$$\begin{bmatrix} \boldsymbol{Z}^{ss} & \boldsymbol{Z}^{sp} \\ \boldsymbol{Z}^{ps} & \boldsymbol{Z}^{pp} \end{bmatrix} \cdot \begin{bmatrix} \boldsymbol{I}^s \\ \boldsymbol{I}^p \end{bmatrix} = \begin{bmatrix} \boldsymbol{0} \\ \boldsymbol{V}^p \end{bmatrix}, \quad (4)$$

where $\boldsymbol{I}^{\mathrm{s}}$ is the unknown coefficients vector associated with the scattering body, and $\boldsymbol{I}^p$ is the unknown coefficients vector associated with the waveport aperture. $\boldsymbol{V}^p$ represents the right-hand vector excited by the waveport. $\boldsymbol{Z}^{ab}$ represents the impedance matrix resulting from the interaction of structures a and b. Letters a and b can be replaced by s (the scattering body) or p (the waveport).

The matrix elements in (4) can be expressed as:

$$\boldsymbol{Z}_{mn}^{sp} = \left\langle f_i, \left[\frac{\zeta}{2} \left(\hat{\mathbf{n}} \times \boldsymbol{M}_j^{port} \right) + K \left(\boldsymbol{M}_j^{port} \right) \right] \right\rangle, \quad (5)$$

$$\boldsymbol{Z}_{mn}^{ps} = \left\langle \boldsymbol{M}_i^{port}, \hat{\mathbf{n}} \times \boldsymbol{J}_j \right\rangle, \quad (6)$$

$$\boldsymbol{Z}_{mn}^{pp} = \left\langle \boldsymbol{M}_i^{port}, \frac{\hat{\mathbf{n}} \times \boldsymbol{e}_j}{\eta_j} \int_A (\hat{\mathbf{n}} \times \boldsymbol{e}_j) \cdot \boldsymbol{M}_j^{port}\, ds \right\rangle, \quad (7)$$

$$\boldsymbol{V}_m^p = \left\langle \boldsymbol{M}_i^{port}, \frac{2\hat{\mathbf{n}} \times \boldsymbol{e}_j}{\eta_j} \right\rangle = -\frac{2\eta_0}{\eta_j} \int_A \boldsymbol{e}_i \cdot \boldsymbol{e}_j\, ds, \quad (8)$$

where m and n denote the row and column numbers of the matrix elements, $\langle \cdot \rangle$ denotes inner product operator, and the definition of ζ is the same as in (2).

B. Analysis of waveguide eigenvalue problem

A variety of methods are used to analyze the waveguide cross-sectional field distribution, including MoM, FDTD, and FEM. Among all these methods, 2-D FEM is the most generally applicable and versatile [12].

Here, to facilitate integrated modeling, the 2-D vector FEM is adopted to analyze the waveguide eigenvalue problems. The tangential electric field $\boldsymbol{E}_t$ and longitudinal electric field $\boldsymbol{E}_z$ on the element are defined as follows, where N and $\boldsymbol{W}$ represent the scalar and vector basis functions, respectively [13, 14]:

$$\boldsymbol{E}_z = N e_z = [L_1\, L_2\, L_3]\, \boldsymbol{e}_z, \quad (9)$$

$$\boldsymbol{E}_t = [\boldsymbol{W}] e_t = [\boldsymbol{W}_{12}\, \boldsymbol{W}_{23}\, \boldsymbol{W}_{31}]\, \boldsymbol{e}_t, \quad (10)$$

$$\mathbf{W}_{ij} = l_{ij}(L_i \nabla_t L_j - L_j \nabla_t L_i), \quad (11)$$

where L_i (i = 1,2,3) are area coordinates of the element, l_{ij} is length of edge that starts from node i to node j, ∇_t is the gradient operator, and $\boldsymbol{e}_z$ and $\boldsymbol{e}_t$ represent the coefficients to be solved for the transverse and direction vectors, respectively.

In order to obtain the eigenvector of the waveguide aperture, the generalized eigenmatrix equation is derived from the Helmholtz equation [12]:

$$\begin{bmatrix} \mathbf{A} & \mathbf{0} \\ \mathbf{0} & \mathbf{0} \end{bmatrix} \begin{bmatrix} \mathbf{e}_t \\ \mathbf{e}_z \end{bmatrix} = -\beta^2 \begin{bmatrix} \mathbf{H} & \mathbf{G} \\ \mathbf{G}^T & \mathbf{B} \end{bmatrix} \begin{bmatrix} \mathbf{e}_t \\ \mathbf{e}_z \end{bmatrix}, \tag{12}$$

$$\mathbf{A} = \int_\Omega \left[\frac{1}{\mu_r} (\nabla_t \times \mathbf{W})^{\mathrm{T}} (\nabla_t \times \mathbf{W}) - k_0^2 \varepsilon_r \mathbf{W}^{\mathrm{T}} \mathbf{W} \right] \mathrm{d}\Omega, \tag{13}$$

$$\mathbf{H} = \int_\Omega \left[\frac{1}{\mu_r} \mathbf{W}^{\mathrm{T}} \mathbf{W} \right] \mathrm{d}\Omega, \tag{14}$$

$$\mathbf{B} = \int_\Omega \left[\frac{1}{\mu_r} (\nabla_t N)^{\mathrm{T}} \cdot (\nabla_t N) - k_0^2 \varepsilon_r N^{\mathrm{T}} N \right] \mathrm{d}\Omega, \tag{15}$$

$$\mathbf{G} = \int_\Omega \left[\frac{1}{\mu_r} \mathbf{W}^{\mathrm{T}} (\nabla_t N) \right] \mathrm{d}\Omega, \tag{16}$$

where ε_r and μ_r represent relative permeability and permittivity of the medium corresponding with the waveguide, β is the propagation constant, k_0 is the wave number of free space, Ω is the cross-section of the waveguide apertures, and N and $\mathbf{W}$ represent the scalar and vector basis functions [10, 11].

According to (18), the orthonormal modal field distributions on quadrilaterals are obtained through the operation, $\boldsymbol{e}_i$ is the i-th mode normalized eigenvector of the waveguide, $\boldsymbol{e}_j$ is the excitation mode, and δ_{ij} is Kronecker delta:

$$\int_S \boldsymbol{e}_i \cdot \boldsymbol{e}_j \mathrm{dS} = \delta_{ij} = \begin{cases} 1, i = j \\ 0, i \neq j \end{cases}. \tag{17}$$

Finally, by using nested one-dimensional Gaussian sampling on the quadrilaterals, we obtain the modal field distribution at the Gaussian sampling points of the waveguide aperture. Applying the results to matrix elements, the 2-D FEM is associated with the MM/HOMoM hybrid method, making the method more flexible.

III. NUMERICAL EXAMPLE

Simulation examples are given in this section to validate the accuracy and computational efficiency of the proposed method, and all simulations employ double-precision numerical accuracy. The computational platform used in these examples is a workstation with two Intel Xeon(R) Gold 5118 CPUs and 512 GB RAM.

A. Asymmetrical single-ridged slotted waveguide antenna

Due to the advantages of easy fabrication and low loss, slotted waveguide antennas have been widely used. Among these, the asymmetrical slotted waveguide antenna is not only small in size, but also has good low sidelobe characteristics [15, 16]. Firstly, a slotted antenna fed by an asymmetrical single-ridged waveguide is analyzed to demonstrate the flexibility of the proposed method. As shown in Fig. 2 and Table 1, the dimensions of the waveport aperture and antenna model are given here, and all slots are the same size. The other side of the antenna waveguide port is connected to a matched terminator.

The S11 is computed from 8.5 to 9.5 GHz (11 frequency points). The model is discretized into 7774 quadrilateral elements and expanded into 15418 unknowns using the proposed method. When using triangles for modeling in FEKO, the antenna is discretized into 17187 meshes and 26949 RWG-MoM unknowns when using a $\lambda/12$ mesh size.

The S parameter and computational statistics comparison are depicted in Fig. 3 and Table 2. The proposed method's efficiency is much greater than the RWG-MoM

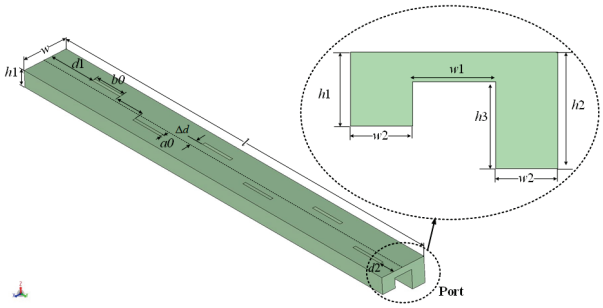

Fig. 2. 3-D model of the slotted waveguide antenna and dimensions of the single-ridged waveport cross-section.

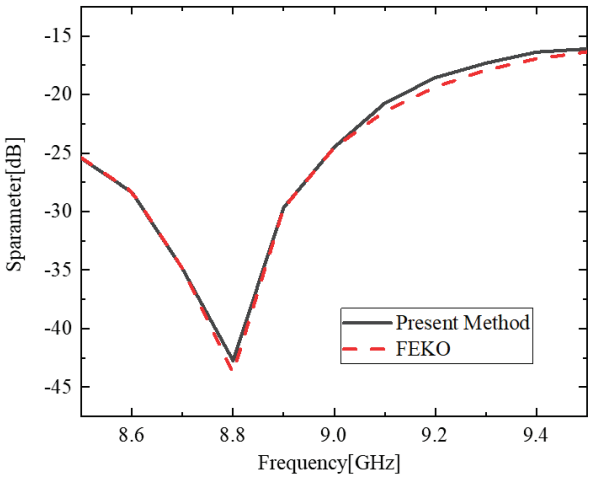

Fig. 3. Comparison of S parameters of the slotted waveguide antenna.

Table 1: Geometrical parameters of the slotted waveguide antenna. All dimensions are in millimeters (mm)

w	$w1$	$w2$	l	$d1$	$d2$
13.72	5.48	4.12	131.9	15.7	4.55
$a0$	$b0$	$h1$	$h2$	$h3$	Δd
0.9	10.15	4.93	7.76	5.79	4.41

Table 2: Computational statistics of the slotted waveguide antenna when 24 cores are used

Method	Present Method	FEKO ($\lambda/12$)
Number of Unknowns	15418	26949
Memory [GB]	3.5	10.8
Time [s]	1071	4554

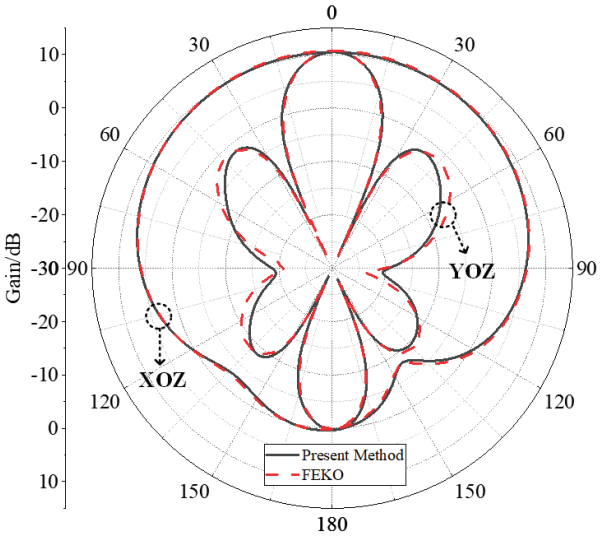

Fig. 4. Radiation pattern of the single-ridged waveguide antenna.

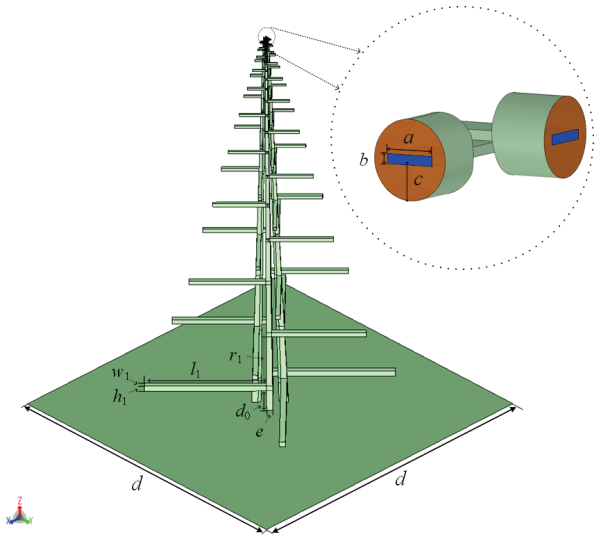

Fig. 5. 3-D model of the log-periodic antenna.

Table 3: Geometrical parameters of the log-periodic antenna. All dimensions are in millimeters (mm)

a	b	c	d	e
2.5	0.5	3.6	1000.0	18.0
l_1	h_1	w_1	r_1	d_0
350.0	17.0	16.8	178.0	66.0

in FEKO. Moreover, the radiation pattern of the slotted antenna is computed. The operating frequency is set to 8.8 GHz, which is the resonant frequency of the waveguide. As seen in the Fig. 4, the gain of the xoz plane and the yoz plane agree well.

B. Log-periodic antennas

A log-periodic antenna (LPA) is then analyzed to illustrate the accuracy and efficiency of the proposed method. The 3-D model of the antenna is shown in Fig. 5, and the dimensions of the antenna are listed in Table 3. The antenna consists of two orthogonal linear polarization elements and a perfect electric conductor (PEC) reflector plane. The antenna has the following parameters: number of elements $N = 18$, scaling factor $\tau = 0.77$, and spacing factor $\sigma = 0.125$. The lengths (l_n), widths (w_n), and spacings (r_n) of the antenna decrease logarithmically as defined by the geometric ratio τ and the spacing factor σ [17, 18]. The top two identical waveguide ports are arranged orthogonally as feeders:

$$\tau = l_{n+1}/l_n = w_{n+1}/w_n, \tag{18}$$

$$\sigma = r_n/4l_n. \tag{19}$$

The operating frequency of the simulation is carried out in 1.0 GHz, and the model is discretized into 6140 bilinear quadrilaterals and 12290 unknowns when using the proposed method. The model was discretized into 13926 triangular patches in FEKO, and the mesh size was $\lambda/12$, yielding 20869 RWG-MoM unknowns. For comparison, the result of FEM is also given to verify the correctness of the proposed method, in which the residual is set to 0.005.

Figure 6 shows a comparison of the radiation pattern results. It can be observed that the presented method in this paper has great agreement with FEKO and FEM within the main lobe, with a small difference below -20 dB. The computational statistics are summarized in Table 4. Due to the use of higher-order basis functions, the number of unknowns can be effectively reduced in the proposed method compared to the RWG-MoM without losing numerical accuracy. Furthermore, the proposed method has advantages in memory and solution time.

To further illustrate the effectiveness of the current approach, we present an example of an LPA array. This array consists of the five antenna elements mentioned above and a PEC reflector with a side length of 2000 mm. Figure 7 and Table 5 show the 3-D model of the array and the distribution in the xoy plane. Figure 8 gives the comparison of the radiation pattern between the present

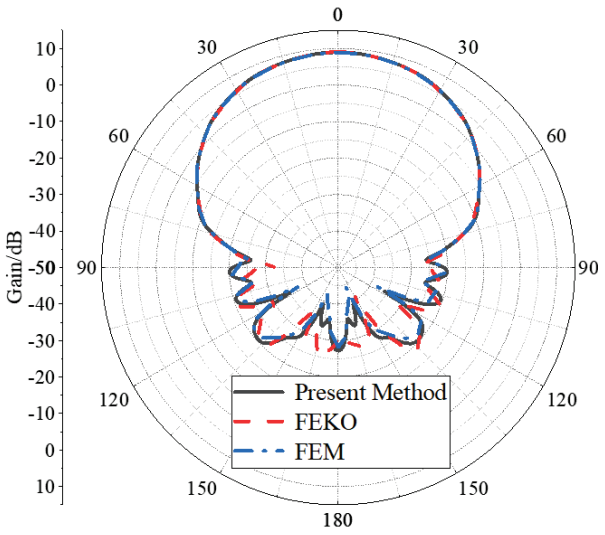

(a)

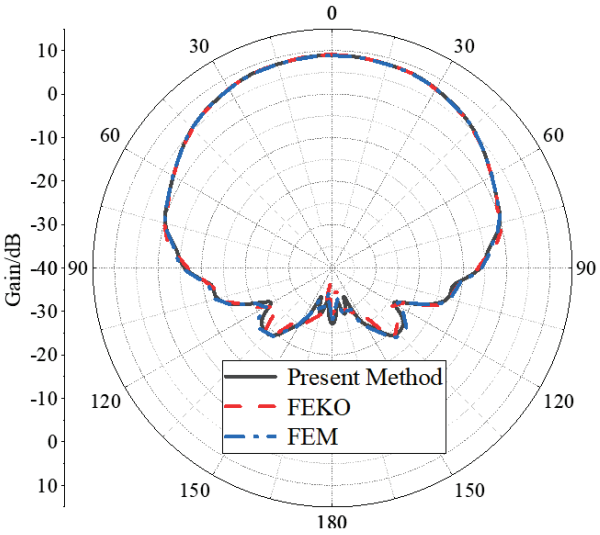

(b)

Fig. 6. Radiation patterns of the log-periodic antenna:(a) xoz plane (b) yoz plane.

Table 4: Computational statistics of the log-periodic antenna when eight cores are used

Method	**Present Method**	**FEKO** ($\lambda/12$)
Number of Unknowns	12290	20869
Memory [GB]	2.3	6.5
Time [s]	119	437

method and FEKO. Additionally, as indicated in Table 6, the proposed method outperforms RWG-MoM in terms of memory usage and time required.

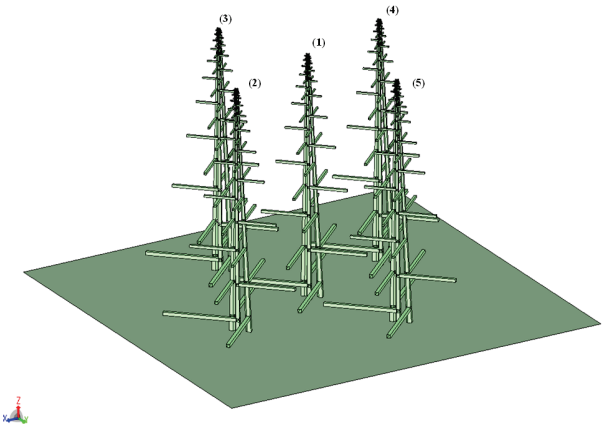

Fig. 7. 3-D model of the log-periodic antenna array.

Table 5: Distribution of the log-periodic antenna in the xoy plane. All dimensions are in millimeters (mm)

Index	**Coordinates**
(1)	$(0,0)$
(2)	$(500,200)$
(3)	$(200,-500)$
(4)	$(-500,-200)$
(5)	$(-200,500)$

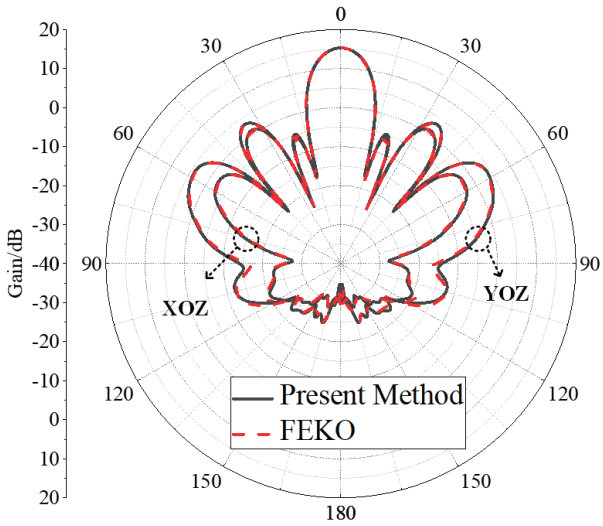

Fig. 8. Radiation pattern of the log-periodic antenna array.

Table 6: Computational statistics of the log-periodic antenna array when 24 cores are used

Method	**Present Method**	**FEKO** ($\lambda/12$)
Number of Unknowns	58332	102799
Memory [GB]	50.7	157.5
Time [s]	1619	14025

IV. CONCLUSION

The MM/HOMoM method and FEM are hybridized to analyze waveguide problems with irregular cross-sections. In order to facilitate integrated modeling, 2-D FEM is used to solve the eigenvalue problem of the waveguide. In addition, higher-order basis functions are used to reduce the unknowns effectively. Results show that the proposed method has the advantage of high efficiency and high numerical accuracy.

ACKNOWLEDGMENT

This work was supported by the Key Research and Development Program of Shaanxi (2022ZDLGY02-03, 2023-ZDLGY-42, 2021GXLH-02) and the Fundamental Research Funds for the Central Universities (QTZX23018).

REFERENCES

[1] A. J. Sangster and H. Wang, "A combined FEM/MOM technique of coupling and radiating apertures in rectangular waveguide," *IEEE Trans. Magn.*, vol. 31, no. 3, pp. 1554-1557, May 1995.

[2] F. Arndt, "Fast CAD and optimization of waveguide components and aperture antennas by hybrid MM/FE/MoM/FD methods-state-of-the-art and recent advances," *IEEE Trans. Microw. Theory Techn.*, vol. 52, no. 1, pp. 292-305, Jan. 2004.

[3] R. Bunger and F. Arndt, "Moment-method analysis of arbitrary 3-D metallic *N*-port waveguide structures," *IEEE Trans. Microw. Theory Techn.*, vol. 48, no. 4, pp. 531-537, Apr. 2000.

[4] V. Catina, F. Arndt, and J. Brandt, "Hybrid surface integral-equation/mode-matching method for the analysis of dielectric loaded waveguide filters of arbitrary shape," *IEEE Trans. Microw. Theory Techn.*, vol. 53, no. 11, pp. 3562-3567, Nov. 2005.

[5] V. Catina and F. Arndt, "Fast method-of-moments analysis of a class of dielectric loaded horns applying higher-order vector basis functions," in *IEEE AP-S Int. Antennas Propag. Symp.*, Honolulu, HI, pp. 3596-3599, 2007.

[6] Y. Wang, X. Zhao, Y. Zhang, S. W. Ting, T. K. Sarkar, and C. H. Liang, "Higher order MoM analysis of traveling-wave waveguide antennas with matched waveports," *IEEE Trans. Antennas Propag.*, vol. 63, no. 8, pp. 3718-3721, Aug. 2015.

[7] Z. Lin, X. Zhao, Y. Zhang, and H. Liu, "Higher order method of moments analysis of metallic waveguides loaded with composite metallic and dielectric structures," *IEEE Trans. Antennas Propag.*, vol. 66, no. 9, pp. 4958-4963, Sep. 2018.

[8] M. Razmhosseini, R. Zabihi, and R. G. Vaughan, "Wideband antennas using coaxial waveguide," *IEEE Trans. Antennas Propag*., vol. 69, no. 10, pp. 6273-6283, Oct. 2021.

[9] K. C. Donepudi, J.-M. Jin, and W. C. Chew, "A higher order multilevel fast multipole algorithm for scattering from mixed conducting/dielectric bodies," *IEEE Trans. Antennas Propag.*, vol. 51, no. 10, pp. 2814-2821, Oct. 2003.

[10] B. M. Kolundzija, "Electromagnetic modeling of composite metallic and dielectric structures," *IEEE Trans. Micro. Theory Techn.*, vol. 47, no. 7, pp. 1021-1032, July 1999.

[11] P. Yla-Oijala and M. Taskinen, "Application of combined field Integral equation for electromagnetic scattering by dielectric and composite objects," *IEEE Trans. Antennas Propag.*, vol. 53, no. 3, pp. 1168-1173, Mar. 2005.

[12] J. F. Lee, D.K. Sun, and Z. J. Cendes, "Full-wave analysis of dielectric waveguides using tangential vector finite elements," *IEEE Trans. Microw. Theory Techn.*, vol. 39, no. 8, pp. 1262-1271, Aug. 1991.

[13] R. D. Graglia, P. Petrini, and A. F. Peterson, "Full-wave analysis of inhomogeneous waveguiding structures containing corners with singular hierarchical curl-conforming vector bases," *IEEE Antennas Wireless Propag. Lett.*, vol. 13, pp. 1701-1704, 2014.

[14] K. Zhang, C.-F. Wang, and J.-M. Jin, "Broadband monostatic RCS and ISAR computation of large and deep open cavities," *IEEE Trans. Antennas Propag.*, vol. 66, no. 8, pp. 4180-4193, Aug. 2018.

[15] W. Wang, S. S. Zhong, Y.-M. Zhang, and X.-L. Liang, "A broadband slotted ridge waveguide antenna array," *IEEE Trans. Antennas Propag*., vol. 54, no. 8, pp. 2416-2420, Aug. 2006.

[16] V. V. Zemlyakov, G. F. Zargano, A. A. Gadzieva, and S. V. Krutiev, "Microwave slot antenna based on asymmetrical ridged waveguide," *Int. Conf. Antenna Theory Techn.*, pp. 193-195, Sep. 2013.

[17] O. Sushko, S. Piltyay, and F. Dubrovka, "Symmetrically fed 1–10 GHz log-periodic dipole antenna array feed for reflector antennas," in *2020 IEEE Ukrainian Microw. Week (UkrMW)*, Kharkiv, Ukraine, pp. 222-225, 2020.

[18] H. Qi, "Elimination of anomalous resonances in coaxial-fed LPDA and its array with integrated Φ-shaped balun," *IEEE Trans. Antennas Propag*., vol. 71, no. 11, pp. 9000-9005, Nov. 2023.

Ning Ding received the B.S. degree from Xidian University, Xi'an, China, in 2017, and is currently working toward the Ph.D. degree at Xidian University. His current research interest is computational electromagnetics.

Zhongchao Lin received the B.S. and Ph.D. degrees from Xidian University, Xi'an, China, in 2011 and 2016, respectively. In 2016, he joined Xidian University as a Post-Doctoral Fellow, where he was lately promoted as an Associate Professor. His research interests include large-scale computational electromagnetics, scattering, and radiation electromagnetic analysis.

Lei Yin was born in Yinchuan, Ningxia, China, in 1995. He received the B.S. degree in electronic and information engineering from Xidian University, Xi'an, China, in 2017. He is currently pursuing the Ph.D. degree with Xidian University, Xi'an, China. His current research interests include computational electromagnetic, parallel computing, and electromagnetic radiation and coupling.

Xunwang Zhao received the B.S. and Ph.D. degrees from Xidian University, Xi'an, China, in 2004 and 2008, respectively. He joined Xidian University in 2008 as a Faculty Member, where he was lately promoted as a Full Professor. He was a Visiting Scholar with Syracuse University, Syracuse, NY, USA, from December 2008 to April 2009. As a Principal Investigator, he works on several projects, including the project of NSFC. His research interests include computational electromagnetics and electromagnetic scattering analysis.

Yu Zhang received the B.S., M.S., and Ph.D. degrees from Xidian University, Xi'an, China, in 1999, 2002, and 2004, respectively. In 2004, he joined Xidian University as a Faculty Member. He was a Visiting Scholar and an Adjunct Professor with Syracuse University, Syracuse, NY, USA, from 2006 to 2009. As a Principal Investigator, he works on projects, including the project of NSFC. He has authored four books, *Parallel Computation in Electromagnetics* (Xidian University Press, 2006), *Parallel Solution of Integral Equation-Based EM Problems in the Frequency Domain* (Wiley IEEE, 2009), *Time and Frequency Domain Solutions of EM Problems Using Integral Equations and a Hybrid Methodology* (Wiley, 2010), and *Higher Order Basis Based Integral Equation Solver* (Wiley, 2012), as well as more than 100 journal articles and 40 conference papers.

A Spatial Modes Filtering FETD Method for 3-D Periodic Structures

Yixin Wang[1,2], Bing Wei[2], Kaihang Fan[3], Xinbo He[2], and Sihan Zhao[4]

[1]Department of Information Technology
Shaanxi Police College, Xi'an, 710021, China
yixwang@stu.xidian.edu.cn

[2]School of Physics
Xidian University, Xi'an 710071, China
bwei@xidian.edu.cn, hexinbo@xidian.edu.cn

[3]School of Information and Communications Engineering
Xi'an Jiaotong University, Xi'an 710049, China
fankaihang@163.com

[4]Science and Technology on Electromechanical Dynamic Control Laboratory
Xi'an, 710065, China
zshanzshan@163.com

Abstract **–** A spatial modes filtering (SMF) finite-element time-domain (FETD) method with periodic boundary condition (PBC) is proposed for efficiently analyzing the electromagnetic characteristics of 3-D periodic structures with partial fine structures. The system matrices of FETD become asymmetrical because of the introduction of PBC, which prevents the system eigenvalue analysis. By decomposing the system matrix into PBC-independent and PBC-related parts, the unstable spatial modes under the given large time step can be found and removed from the symmetrical PBC-independent system matrices. Then the system matrix equation and time marching of the SMF-FETD and SMF-FETD method based on local eigenvalue solution (LES-SMF-FETD) with PBC are obtained. Numerical results illustrate the efficiency and effectiveness of the SMF-FETD method with PBC based on non-uniform mesh for analyzing the transport properties of 3-D periodic structures.

Index Terms **–** 3-D periodic structures, finite-element time-domain (FETD), Floquet theorem, non-uniform mesh, periodic boundary condition (PBC), spatial modes filtering (SMF).

I. INTRODUCTION

Periodic structures [1, 2] are formed by finite or infinite periodic arrangements of identical units and have a vast range of applications, such as gratings [2, 3], photonic bandgap [4, 5] and electromagnetic bandgap [5–8] structures. For infinite periodic structures, the Floquet theorem and periodic boundary condition (PBC) can be applied to approximate the electromagnetic properties of the entire periodic structure by analyzing one unit cell of the periodic structure. However, if the periodic structure contains complex and fine structures, the space step size of finite-element time-domain (FETD) will be tiny to capture them accurately when discretizing the computational domain, increasing the number of grids and memory demand by a considerable amount. At the same time, FETD is limited by the stability condition [9, 10]. The minimum space step restricts the time step and has to be very small, which leads to long calculation time and low efficiency. Recently, the spatial modes filtering (SMF) method has been proposed and introduced to FETD to break through the stability condition [11–12] by filtering out the spatial modes that are unstable under the given larger time step from the numerical system, substantially improving computation efficiency. Later, the spatial modes filtering finite-element time-domain (SMF-FETD) method based on local eigenvalue solution (LES-SMF-FETD) is proposed, also combined with non-uniform grids [13–15]. The use of non-uniform grids not only ensures the discretization quality required by fine structures but also avoids over-division in the region without fine structures, which has a natural advantage in the analysis of periodic structures with complex fine structures. Current research is limited in 2-D periodic structures [16], the study of the transport properties of 3-D periodic structures with higher practical value has not been carried out.

Submitted On: June 30, 2023
Accepted On: November 5, 2024

https://doi.org/10.13052/2025.ACES.J.400202

In this paper, PBC is introduced to the SMF-FETD method with non-uniform grids for efficiently analyzing the electromagnetic characteristics of 3-D periodic structures with partial fine structures. Through the

Floquet theorem, the correspondence of the electric field components of the periodic boundary elements is given in detail. The mass and stiffness matrices of FETD with PBC no longer maintain the symmetric positive definite or symmetric semi-normal definite characteristic, which is a prerequisite for the SMF method. To this end, the new system matrix is split into two parts, PBC-independent and PBC-related, then through the generalized eigenvalue decomposition of the PBC-independent system and the unstable spatial modes are filtered out. Then the system matrix equation and time marching of the SMF-FETD and LES-SMF-FETD with PBC are obtained. PBC effectively reduces the computational domain of the periodic structure to one periodic unit cell then, combined with the non-uniform mesh scheme, the number of unknowns is further reduced while ensuring the mesh accuracy, effectively improving the computational efficiency of the SMF-FETD method for periodic structures. The accuracy of the SMF-FETD with PBC is validated by calculating the transmittance of an infinitely large dielectric plate. Furthermore, the efficiency of the proposed method is demonstrated through analysis of the transmission spectrum of the metallic grating with grooves.

II. NUMERICAL FORMULATIONS

A. Periodic boundary condition in 3-D

A simple periodic structure model with an infinite number of periodic unit cells T along the z-direction is shown in Fig. 1 (a), according to the Floquet theorem:

$$f(x,y,z+T,t) = f(x,y,z,t) \tag{1}$$

which means the physical structure and the field distributions of each unit cell T are the same. The computational domain is restricted to any single T by PBC according to (1), then the electromagnetic characteristics of the entire periodic structure can be equated by this unit cell. Because of the PBC, the boundary elements b and c are located inside the computational domain, and a and d are located outside. Elements a and c differ by one period T in the z-direction, as do b and d. At this time, the electric field distributions on the boundary elements satisfy the following:

$$\begin{aligned}
&E_1^a(t) = E_3^b(t), E_2^a(t) = E_4^b(t)\\
&E_5^a(t) = E_6^b(t), E_7^a(t) = E_8^b(t)\\
&E_i^a(t) = E_i^c(t), i = 3,4,6,8,9,10,11,12\\
&E_3^d(t) = E_1^c(t), E_4^d(t) = E_2^c(t),\\
&E_6^d(t) = E_5^c(t), E_8^d(t) = E_7^c(t)\\
&E_i^d(t) = E_i^b(t), i = 1,2,5,7,9,10,11,12
\end{aligned} \tag{2}$$

where i denotes the edge number of the boundary elements.

The edges at the periodic boundary participate in the construction of the computational domain's inner and outer boundary element matrices. As shown in Fig. 1 (b), take the PBC-Top surface as an example, the edges of the PBC surface not only participate in the b-element matrix construction as the 3#, 4#, 6#, and 8# edges but also participates in the a-element matrix construction as the 1#, 2#, 5#, and 7# edges. When forming the system matrices, according to (2), the coupling relationship of the a-element edges can be directly replaced by the corresponding edges of the c-element. In other words, introduction of PBC is realized by the extra special coupling relationship between the b-elements and c-elements, which will change the number and distribution of the non-zero elements of the original system mass matrix and stiffness matrix of FETD.

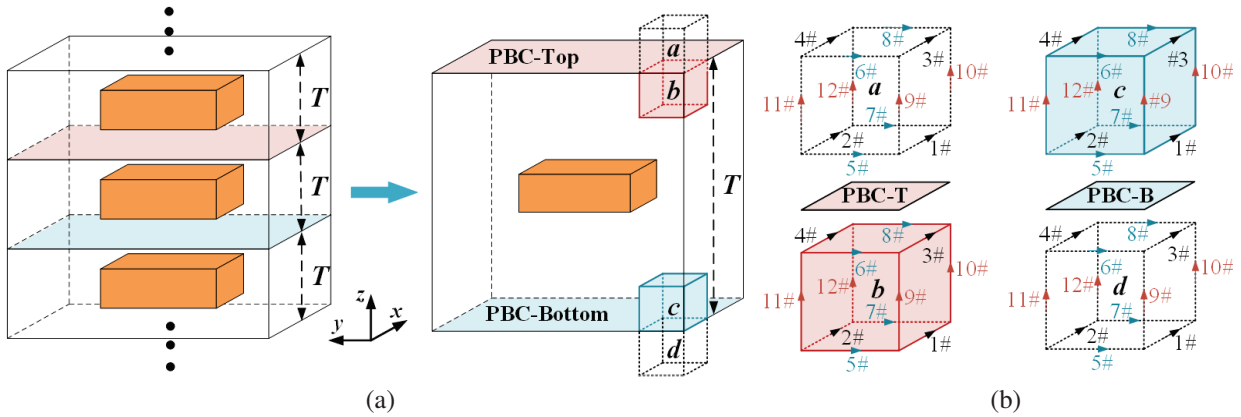

(a) (b)

Fig. 1. (a) Model of a simple periodic structure and its period ***T*** and (b) edges distribution of elements on periodic boundary.

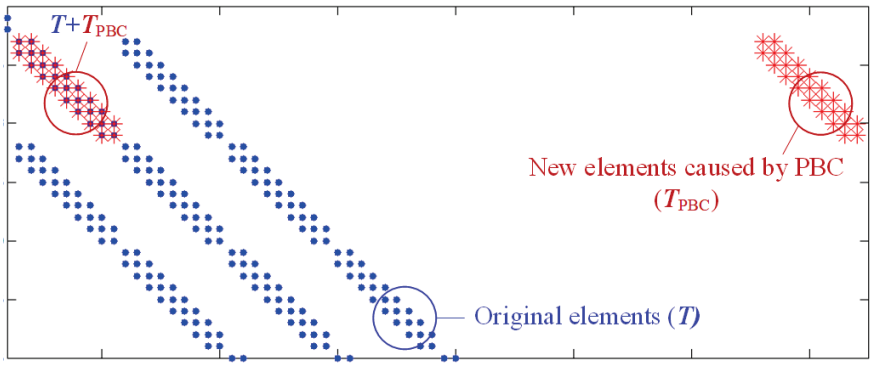

Fig. 2. Partial non-zero elements distribution of T_{new}.

B. SMF-FETD with periodic boundary conditions

With the new system mass matrix $\boldsymbol{T}_{new}$ and stiffness matrix $\boldsymbol{S}_{new}$, the matrix equation of FETD with PBC can be written as:

$$\boldsymbol{T}_{new}\frac{d^2e}{dt^2}+\boldsymbol{S}_{new}e=\boldsymbol{j}, \tag{3}$$

where e denotes the correlation coefficient vector of the edge basis function and j denotes the excitation vector. The core of the SMF-FETD method is the generalized eigenvalue analysis of the numerical system, which requires that the system matrices must be symmetric positive or semi-positive definite [12]. Due to the non-zero elements distribution given in Fig. 2, the new non-zero elements caused by the introduction of PBC may located at the same or different positions with the original non-zero elements of $\boldsymbol{T}$, resulting in the asymmetric characteristic of $\boldsymbol{T}_{new}$. Similar to $\boldsymbol{T}_{new}$, $\boldsymbol{S}_{new}$ is also asymmetric and its non-zero elements distribution is more complex. Split the asymmetric matrices $\boldsymbol{T}_{new}$ and $\boldsymbol{S}_{new}$ into two parts as shown in (4), symmetric matrices $\boldsymbol{T}$ and $\boldsymbol{S}$ are not relevant to PBC, while asymmetric matrices $\boldsymbol{T}_{PBC}$ and $\boldsymbol{S}_{PBC}$ are:

$$\begin{aligned}\boldsymbol{T}_{new}&=\boldsymbol{T}+\boldsymbol{T}_{PBC}\\ \boldsymbol{S}_{new}&=\boldsymbol{S}+\boldsymbol{S}_{PBC}.\end{aligned} \tag{4}$$

Performing a generalized eigenvalue analysis on (3), the matrix composed of the eigenvectors of unstable spatial modes under a given large time step is denoted as Φ_h. Combined with (4), the matrix equation of SMF-FETD with PBC can be obtained:

$$\boldsymbol{T}_{new}\frac{d^2e}{dt^2}+\left(\boldsymbol{S}(\boldsymbol{I}-\Phi_h\Phi_h{}^{\boldsymbol{T}}\boldsymbol{T})+\boldsymbol{S}_{PBC}\right)e=\boldsymbol{j}. \tag{5}$$

The central-difference scheme with the explicit solution is used to discrete time variables of (5), the time marching of SMF-FETD with PBC is as follows:

$$\begin{aligned}\boldsymbol{T}_{new}e^{n+1}=&\,2\boldsymbol{T}_{new}e^{n}-\boldsymbol{T}_{new}e^{n-1}+\Delta t^2\boldsymbol{j}^n\\ &-\Delta t^2\left(\boldsymbol{S}_{PBC}-\boldsymbol{S}(\boldsymbol{I}-\Phi_h\Phi_h{}^{\boldsymbol{T}})\right)e^n.\end{aligned} \tag{6}$$

Further through the LES [13], by replacing Φ_h in (5) and (6) with Ψ_h, which is composed of the eigenvectors of the unstable modes obtained from the local system containing the fine edges and their coupling coarse edges, the matrix equation and time marching of the LES-SMF-FETD with PBC can be obtained.

III. NUMERICAL RESULTS

A. Transmission coefficient of an infinitely large dielectric plate

The planar Gaussian pulse with the relevant parameters $\tau=6\times10^{-9}s$ and $t_0=\tau$ is incident vertically along the y- direction on an infinitely large dielectric plate of thickness 0.1 m and relative permittivity $\varepsilon_r=25$. The mesh distribution of different computational models and boundary settings are shown in Fig. 3, the absorbing boundary condition (ABC) is set in the y-direction while the PBC is set in other directions. The mesh scale of

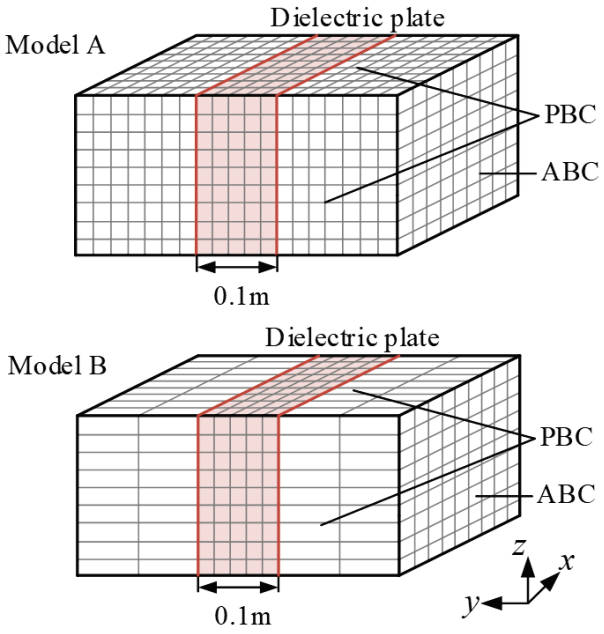

Fig. 3. Mesh distribution of computational domain.

model A is 0.02 m×0.02 m×0.02 m resulting in 45144 unknowns, while the mesh scales of model B are 0.02 m×0.02 m×0.02 m and 0.02 m×0.1 m×0.02 m, resulting in 10044 unknowns. As shown in Fig. 4, the transmission coefficients obtained from different methods are in good agreement with the analytical solution, verifying the correctness of introducing PBC into the SMF-FETD with non-uniform mesh scheme.

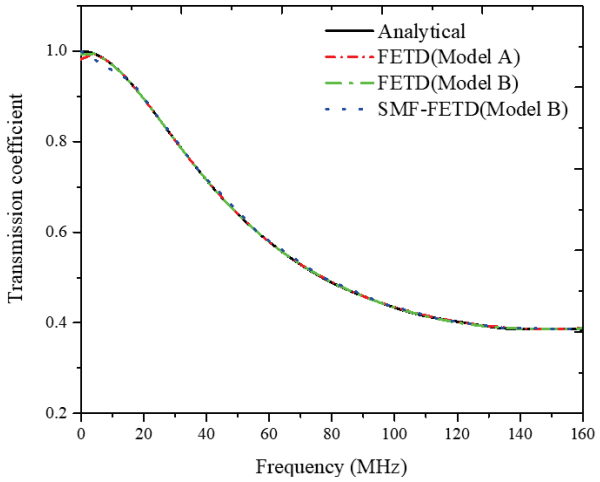

Fig. 4. Transmission coefficient of infinite dielectric plate obtained from different methods.

B. Transmission characteristics of the metallic grating with grooves

As shown in Fig. 5, a metallic grating is composed of periodically arranged metal blocks with grooves. Its geometric parameters are: $C_x = 200$ nm, $C_y = 200$ nm, $C_z = 80$ nm, $a = 80$ nm, $b = 80$ nm, and $T = 400$ nm. The computational domain is discretized by 2300 non-uniform grids, where the scale of fine grid is 40 nm × 8 nm × 40 nm and the coarse grid is 40 nm × 40 nm × 40 nm. The maximum frequency of the planar Gaussian pulse is $f_{\max} = 750$THz with relevant parameters $\tau = 1/(2f_{\max})$ and $t_0 = 3\tau$.

The transmission spectrums of the periodic metallic grating obtained from different methods are in good agreement, as shown in Fig. 6. The computational statistics of different methods are given in Table 1. SMF-FETD effectively expands the time step and improves the efficiency compared with FETD but requires high time and memory for global eigenvalue solution since the size of the system matrix is 8441 × 8441. LES-SMF-FETD effectively improves the deficiency of SMF-FETD through the LES method. The local system matrix of size 3554 × 3554 contains the relationships between fine edges and their coupled coarse edges, which reduces the time and memory requirements for calculation. Thus,

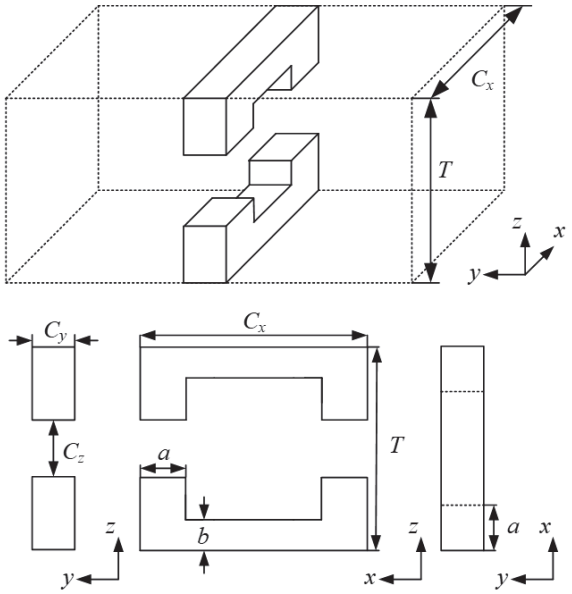

Fig. 5. Schematic diagram of one period of the 3-D metallic grating with an indentation.

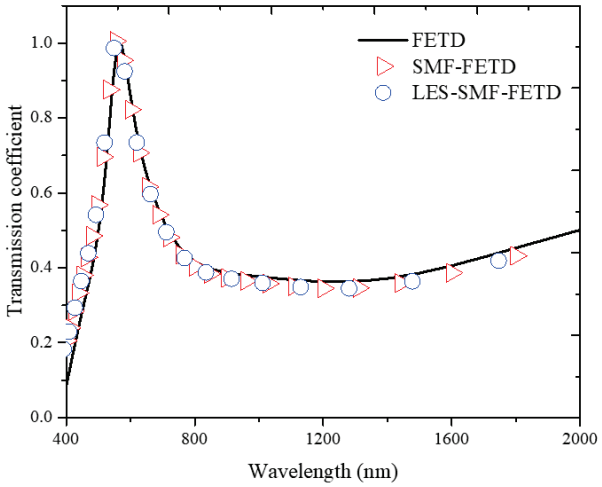

Fig. 6. Transmission spectrums of the metallic grating obtained from different methods.

LES-SMF-FETD takes advantage of the SMF method to a greater extent.

The effect of the variation of geometric parameters on the transmission spectrum of the metallic grating is analyzed. As shown in Fig. 7 (a), when $C_x = 200$ nm, $C_y = 200$ nm, and $C_z = 160$ nm, as T increases, the frequency of the transmission peak becomes lower and the peak value decreases. When $T = 800$ nm, $C_y = 200$ nm, and $C_z = 160$ nm, as shown in Fig. 7 (b), as C_x increases, the frequency of transmission peak becomes higher but the peak value decreases. At the same time, when $C_x = 440$ nm and $C_x = 520$ nm, parts of electromagnetic

Table 1: Simulation parameters of different methods

Method	Time Step (fs)	Total Time/ Eigenvalue Analysis Time (s)	Memory (MB)
FETD	0.0100	425.42/—	34.78
SMF-FETD	0.0468	332.72/167.83	3538.30
LES-SMF-FETD	0.0468	113.76/18.96	629.15

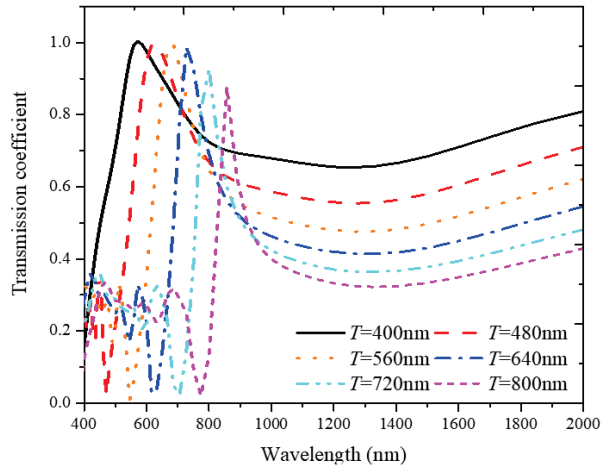

(a)

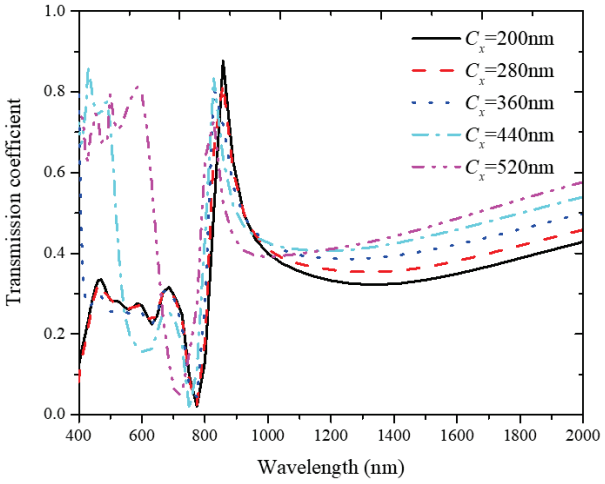

(b)

Fig. 7. (a) Effect of T on the transmission spectrum and (b) effect of C_x on the transmission spectrum.

waves with wavelength ranges of 400 nm to 700 nm are also transmitted.

IV. CONCLUSION

In this paper, the periodic boundary is introduced into the 3-D SMF-FETD and LES-SMF-FETD method with non-uniform meshes by the Floquet theorem. The matrix asymmetry caused by PBC is solved by splitting the system matrix into two parts: PBC-independent and PBC-related. Unstable spatial modes are filtered out from the PBC-independent system through the SMF method. The SMF-FETD and LES-SMF-FETD with PBC are applied to the simulation analysis of the transmission properties of 3-D periodic structures. The correctness of the SMF-FETD method with PBC is verified by calculating the transmission coefficient of an infinite dielectric plate. The calculation of transmission spectrums of the metallic grating with grooves illustrates the efficiency and accuracy of the SMF-FETD and LES-SMF-FETD methods with PBC for simulating 3-D periodic structures.

ACKNOWLEDGMENT

This work was supported by the Shaanxi Natural Science Basic Research Project of Shaanxi Science and Technology Office (No. 2023-JC-QN-0673) and supported by the Key Core Technology Research Project of the 2024 Shaanxi Provincial Key Research and Development Plan (in the field of social development, NO. 2024SF2-GJHX-11).

REFERENCES

[1] Y. F. Mao, B. Chen, R. Xiong, Z. Cai, and Q. Chen, "A novel weakly conditionally stable FDTD method for periodic structures," *IEEE Antennas Wireless Propag. Lett.*, vol. 11, pp. 164-167, Feb. 2012.

[2] T. L. Liang, W. Shao, S. B. Shi, and H. Ou, "Analysis of extraordinary optical transmission with periodic metallic gratings using ADE-LOD-FDTD method," *IEEE Photonics Journal*, vol. 8, no. 5, pp. 1-10, Oct. 2016.

[3] X. K. Wei, W. Shao, and H. Ou, "Domain decomposition CN-FDTD method for analyzing dispersive metallic gratings," *IEEE Photonics Journal*, vol. 9, no. 4, pp. 1-18, Aug. 2017.

[4] V. Radisic and Y. Qian, "Broad-band power amplifier using dielectric photonic bandgap structure," *IEEE Microw. Guided Wave Lett.*, vol. 8, no. 1, pp. 13-14, Jan. 1998.

[5] M. N. Vouvakis, Z. Cendes, and J. F. Lee, "A FEM domain decomposition method for photonic and electromagnetic band gap structures," *IEEE Trans. Antennas Propag.*, vol. 54, no. 2, pp. 721-733, Feb. 2006.

[6] A. Pirhadi, H. Bahrami, and A. Mallahzadeh, "Electromagnetic band gap (EBG) superstrate resonator antenna design for monopulse radiation pattern," *Applied Computational Electromagnetics Society (ACES) Journal*, vol. 27, no. 11, pp. 908-917, Nov. 2012.

[7] P. Bora, P. Pardhasaradhi, and B. Madhav, "Design and analysis of EBG antenna for Wi-Fi, LTE,

and WLAN applications," *Applied Computational Electromagnetics Society (ACES) Journal*, vol. 35, no. 9, pp. 1030-1036, Sep. 2020.

[8] L. Peng, C. L. Ruan, and J. Xiong, "Compact EBG for multi-band applications," *IEEE Trans. Antennas Propag.*, vol. 60, no. 9, pp. 4440-4444, Sep. 2012.

[9] J. F. Lee, R. Lee, and A. Cangellaris, "Time-domain finite-element methods," *IEEE Trans. Antennas Propag.*, vol. 45, no. 3, pp. 430-442, Mar. 1997.

[10] F. L. Teixeira, "Time-domain finite-difference and finite-element methods for Maxwell equations in complex media," *IEEE Trans. Antennas Propag.*, vol. 56, no. 8, pp. 2150-2166, Aug. 2008.

[11] D. Jiao and J. M. Jin, "A general approach for the stability analysis of the time-domain finite-element method for electromagnetic simulations," *IEEE Trans. Antennas Propag.*, vol. 50, no. 11, pp. 1624-1632, Nov. 2002.

[12] W. Lee and D. Jiao, "An alternative explicit and unconditionally stable time-domain finite-element method for electromagnetic analysis," *IEEE J. Multiscale Multiphys. Comput. Tech.*, vol. 3, pp. 16-28, Mar. 2018.

[13] K. H. Fan, B. Wei, and X. B. He, "A subgridding unconditionally stable FETD method based on local eigenvalue solution," *IEEE Trans. Antennas Propag*, vol. 69, no. 8, pp. 4695-4705, Aug. 2021.

[14] Y. X. Wang, B. Wei, and K. H. Fan, "A spatial modes filtering FETD method with non-uniform subgridding mesh," *IEEE Microw. Wireless Tech. Lett.*, vol. 33, no. 6, pp. 635-638, June 2023.

[15] S. H. Zhao, B. Wei, and X. B. He, "Efficient implementation of unconditionally stable FDTD with the local eigenvalue solution," *Journal of Xidian University*, vol. 49, no. 1, pp. 188-193, Feb. 2022.

[16] Y. X. Wang, B. Wei, and K. H. Fan, "Analysis of transmission characteristics of EBG structures by subgridding unconditionally stable FETD," *Applied Computational Electromagnetics Society (ACES) Journal*, vol. 37, no. 9, pp. 921-932, Feb. 2023.

Yixin Wang was born in Xi'an, Shaanxi, China, in 1995. She received the B.S. degree in electromagnetic wave propagation and antenna and the Ph.D. degree in physics from Xidian University, Xi'an, China, in 2017 and 2023, respectively. She is currently working as a physics teacher at Shaanxi Police College. Her current research interests include the finite-element time-domain method and its related methods.

Bing Wei was born in Tianshui, Gansu, China, in 1970. He received the B.S. degree in physics from Beijing Normal University, Beijing, China, in 1993, and the Ph.D. degree in radio science from Xidian University, Xi'an, China, in 2004. From 1993 to 1998, he was a physics teacher at Tianshui Normal University, Tianshui, China. From 1998 to 1999, he was a physics teacher at Baoji University of Arts and Science, Baoji, China. Since 2004, he has been with Xidian University. Currently, he is a professor at Xidian University. His research interests include investigations of electromagnetic field theory, numerical field computation, and short pulse interactions om complex objects.

Kaihang Fan was born in Linfen, Shanxi, China, in 1990. She received the B.S. degree in electronic information science and technology and the Ph.D. degree in radio science from Xidian University, Xi'an, China, in 2014 and 2021, respectively. She is currently working as a postdoctoral researcher at the School of Information and Communications Engineering, Xi'an Jiaotong University, Xi'an, China. Her current research interests include the finite-element time-domain method and the multi-physics problem.

Xinbo He was born in Shaanxi, China, in 1991. He received the B.S. degree in electromagnetic wave propagation and antennae and the Ph.D. degree in radio science from Xidian University, Xi'an, China, in 2014 and 2021, respectively. He is currently a Post-Doctoral Fellow with the School of Physics, Xidian University. His current research interests include the fields of electromagnetic scattering and the finite-difference time-domain method.

Sihan Zhao was born in Xi'an, Shaanxi, China, in 1995. She received the B.S. degree in communication engineering from Xi'an University of Post & Telecommunications, Xi'an, China, in 2017, and the Ph.D. degree in radio science from Xidian University, Xi'an, China, in 2023. She is currently a researcher with Science and Technology on Electromechanical Dynamic Control Laboratory. Her current research interests include the finite-difference time-domain method and its related methods.

Electromagnetic Scattering from a Three-dimensional Object using Physics-informed Neural Network

Yuan Zhang[1], Renxian Li[1], Huan Tang[1], Zhuoyuan Shi[1], Bing Wei[1], Shuhong Gong[1], Lixia Yang[2], and Bing Yan[3,4]

[1]School of Physics, Xidian University
Xi'an 710071, China
zhangyuan9938@163.com, rxli@mail.xidian.edu.cn, 1327441185@qq.com,
zhuoyuans2000@163.com, bwei@xidian.edu.cn, shgong@xidian.edu.cn

[2]Information Materials and Intelligent Sensing Laboratory of Anhui Province
Anhui University, China
lixiayang@yeah.net

[3]School of Information and Communication Engineering
North University of China 030051, China
yanbing122530@126.com

[4]Shanxi Key Laboratory of Signal Capturing and Processing
North University of China, 030051, Shanxi Taiyuan, China
yanbing122530@126.com

***Abstract* –** Prediction of electromagnetic fields scattered from objects is of great significance in various fields. Traditional computational electromagnetic solvers, which are mesh-based, are expensive and time-consuming. The deep learning technique becomes an alternative method of the prediction of scattered fields with high efficiency. However, the data-driven deep learning method requires a large data set and lacks robustness. For complicated scattering problems, the construction of a large training data set is a hard task. By considering physics-constraints, physics-informed neural networks (PINNs) can solve the partial differential equation (PDE) problem with a small data set and also provide a physical explanation. In this paper, the PINNs are employed to solve the scattering of a plane wave by a three-dimensional object with Maxwell's equations being physical constraints. In the calculation, a sphere and an ellipsoid are taken as examples, and the effects of the network parameters (including the number of hidden layers, and the number of data sets) are mainly discussed. The results have practical applications in many fields such as radar detection, biomedical imaging, and satellite navigation.

***Index Terms* –** electromagnetic scattering, Maxwell's equations, physics-informed neural network.

I. INTRODUCTION

Many practical applications in medicine, aerospace, communication, and remote sensing [1–4] involve the electromagnetic scattering by objects. The electromagnetic scattering problem refers to the study of the electromagnetic response resulting from the incident electromagnetic waves given the target and environmental information. Numerical methods can accurately predict the scattered field distribution of an isolated object. In the past developments, computational electromagnetics have provided the basis for solving many practical problems without analytic counterparts, and have become a popular mainstream approach for a wide range of researchers. However, traditional computational electromagnetic solvers such as the finite difference time domain (FDTD) [5, 6], the finite-element method (FEM) [7], and the finite difference frequency domain (FDFD) [8] are based on dividing the solution domain into a network of differences, and replacing the continuous solution domain with a finite number of mesh nodes. This method requires discretization and is solved by meshing the problem area. However, in many practical problems, the region is often not a regular and easy-to-fractionalise geometric region, and it is difficult to generate a mesh. Thus mesh-based methods cannot

Submitted On: July 20, 2023
Accepted On: January 9, 2024

https://doi.org/10.13052/2025.ACES.J.400203

achieve good results and are very time-consuming and computationally expensive [9].

Meanwhile, as artificial intelligence (AI) technology explodes, researchers are trying to apply neural networks to computational electromagnetics as a replacement method for predicting scattered fields. Deep learning (DL) methods such as convolutional neural networks (CNN), recurrent neural networks (RNN), and generative adversarial networks (GANs) have led to amazing advances in the field of computational physics in modeling physical learning agents [10]. Deep learning techniques can identify the hidden rules of the 'action-reaction' behavior of the control system through a certain learning process [11], which is based on the principle of establishing a functional mapping between the input data and the output data. The optimization capabilities and coded boundary conditions of deep learning can improve the accuracy and efficiency of electromagnetic simulations by capturing complex behaviors, providing implicit representations, enabling generalization, reducing computational costs, and enabling efficient parallelization. Deep learning models are capable of capturing the intricate nonlinear relationships in data. By encoding boundary conditions that are critical in electromagnetic simulations, models can learn complex behaviors and interactions at the boundary more efficiently than traditional interpolation techniques. This allows for a more accurate representation of electromagnetic fields and their propagation. At the same time, the deep learning model can generalize from limited training data to unknown scenarios. Once trained on a different set of boundary conditions, the model can accurately predict the electromagnetic field for new boundary conditions outside the training dataset. This generalization capability greatly improves the accuracy of the simulation, especially when it is impractical or costly to obtain a large number of training samples. In contrast, traditional function interpolation techniques typically require a dense grid of points to accurately represent the electromagnetic field, which can lead to costly simulation calculations. Various studies have shown that machine-learning-based algorithms have promising applications in the field of solving partial differential equations [5], which can largely reduce the memory required for computation and are simple and easy to implement and can well meet the needs of electromagnetic properties for engineering applications. Traditional deep learning methods are purely data-driven and require large datasets for training. However, for some complex scatterers, large training data sets are not available. Also, in many physics and engineering fields, these training data often imply partial a priori knowledge (e.g., electric field data satisfying the Maxwell system of equations), but the pure data drive ignores this partial knowledge.

The limitations of the above methods have largely contributed to the emergence of physics-informed neural networks (PINNs). Lagaris et al. [12] pioneered the similarity between neural network training and solving partial differential equations, and neural networks of physics knowledge were proposed for solving Maxwell's set of equations for scattering problems. In this case, the network constructs a mapping of spatial and temporal coordinates to the corresponding electromagnetic field at that point. At the same time, the gradient of the electric field concerning the spatial coordinates can be calculated quickly by using the automatic differentiation algorithm, which speeds up the numerical calculation of the partial differential equation. Compared with the standard numerical methods in traditional computational electromagnetics, the computational efficiency is significantly improved. In 2019, Raissi [13] classifies the model equation as a physical driver as a regularization term and encodes it into the neural network by adding the loss of the control equation and the loss of the boundary conditions and initial conditions to the loss function. Under the condition of the small dataset, we successfully learned a model with stronger generalization ability. It not only learns the distribution law of training data samples like traditional neural networks, but also learns the physical laws described by mathematical equations, and can learn more generalized models with fewer data samples, which solves the difficulties of decision-making and prediction caused by the unavailability of traditional deep neural networks and the scarcity of data. In summary, the PINNs have great advantages in the field of computational electromagnetics, and the development prospects are very promising in saving memory, improving prediction accuracy, and solving high-dimensional complex problems.

In this contribution, we build a fully connected neural network, encode physical information such as Maxwell's equations and boundary conditions as constraints into the neural network, and study the electromagnetic scattering from a three-dimensional object by training the built network model with a sphere and an ellipsoid as examples. We compare the prediction results based on the PINNs method with the analytical solution by Mie theory (for sphere) or numerical results by FDFD (for ellipsoid) to verify the feasibility and accuracy of our work, and the effects of network parameters are mainly discussed. The full paper is divided into four parts, and in the second part, we introduce our proposed PINNs. In the third part, we give the simulation results of PINNs and discuss the effects of network structure and hyperparameters on the results. The fourth part is a summary of the paper.

II. METHODOLOGY AND FORMULATION

A. Deep learning framework

In this paper, we propose a deep learning method for solving Maxwell's equations, using the powerful optimization capability of deep learning to solve the frequency-domain electromagnetic field. In this approach, we encode the boundary conditions (BC), and Maxwell's equations as regularization terms of the network so that it approximates the analytic solution infinitely. According to the electromagnetism uniqueness theorem [14], Maxwell's equations can be solved uniquely for known boundary conditions. Thus, we successfully transformed an electromagnetic forward modeling problem into an optimization process.

B. Details and implementation

Assuming a time dependence $e^{j\omega t}$, the scattered magnetic field satisfies the following vector wave equation:

$$\nabla^2 \mathbf{H_{scat}} + \omega^2 \mu \varepsilon \mathbf{H_{scat}} = \omega^2 (\mu_0 \varepsilon_0 - \mu \varepsilon) \mathbf{H_{inc}}, \quad (1)$$

where, ω is the angular frequency, μ is the magnetic permeability, ε is the electric permittivity, and μ_0 and ε_0 are the magnetic permeability and electric permittivity of a vacuum, respectively. $\mathbf{H_{scat}}$ and $\mathbf{H_{inc}}$ are the scattered and incidence magnetic fields, respectively.

Next, we will use the PINNs to solve the vector wave equation (1). Figure 1 shows a schematic of the neural network layout. We first define a network *NN* with parameters θ to represent the surrogate of the equation solution.

Due to the frequency domain approach, in the PINNs model shown in Fig. 1, the input to the network is the spatial coordinates of the solution area without temporal information, and the output is the real and imaginary parts of the scattered magnetic field, which is denoted by u_{NN} in Fig. 1.

Therefore, the loss function can be divided into three parts, which are $Loss_d$, $Loss_b$, and $Loss_m$:

$$Loss_{total} = Loss_d + Loss_b + Loss_m, \quad (2)$$

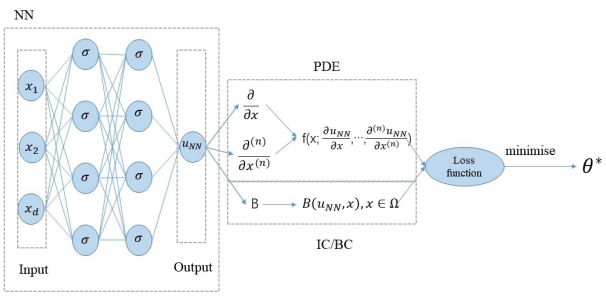

Fig. 1. Representative diagram of the physics-informed neural network model.

where:

$$\begin{cases} Loss_d = \frac{1}{N_d} \sum_{i=1}^{N_d} (|H_i^P| - |H_i^T|), \\ Loss_b = \frac{1}{N_b} \sum_{i=1}^{N_b} (|H_i^P|^2), \\ Loss_m = \frac{1}{N_s} \sum_{i=1}^{N_s} (|g_1|^2 + |g_2|^2 + |g_3|^2), \end{cases} \quad (3)$$

and $Loss_d$ corresponds to the data constraints. H_i^P and H_i^T denote the predicted and true values, respectively. $Loss_b$ corresponds to the boundary condition. Note that, in our model, we only consider the boundary conditions at the outer boundary of the perfectly matched layer (PML), where the scattered magnetic fields vanish and $H_i^P = 0$. $Loss_m$ enforces the vector wave equations at a certain set of points. Unlike traditional deep learning, this loss function considers physical information constraints. N_d, N_b, and N_s denote the residual points for $Loss_d$, $Loss_b$, and $Loss_m$, respectively.

In this paper, we use Mean Absolute Error (MAE) to assess model performance. MAE is a common metric used in regression problems to assess the performance of predictive models. It measures the average absolute difference between the predicted and actual values in the data set. The MAE does not cancel out positively or negatively because the deviation is absolutised, thus, the mean absolute error better reflects the actual situation of the prediction value error.

To define the functions g_1, g_2, and g_3 in equation (3), the object is assumed to be surrounded by a PML to prevent the wave from reflecting from the boundary and re-entering the simulation domain.

In this paper we use the stretched-coordinate PML (SC-PML), and g_1, g_2, and g_3 can be defined as:

$$\begin{cases} g_1 = \frac{1}{s_x}\frac{\partial}{\partial x}\left(\frac{1}{s_x}\frac{\partial H_{scat,x}}{\partial x}\right) + \frac{1}{s_y}\frac{\partial}{\partial y}\left(\frac{1}{s_y}\frac{\partial H_{scat,x}}{\partial y}\right) \\ \quad + \frac{1}{s_z}\frac{\partial}{\partial z}\left(\frac{1}{s_z}\frac{\partial H_{scat,x}}{\partial z}\right) + \omega^2 \mu \varepsilon H_{scat,x} \\ \quad - \omega^2 (\mu_0 \varepsilon_0 - \mu \varepsilon) H_{inc,x}, \\ g_2 = \frac{1}{s_x}\frac{\partial}{\partial x}\left(\frac{1}{s_x}\frac{\partial H_{scat,y}}{\partial x}\right) + \frac{1}{s_y}\frac{\partial}{\partial y}\left(\frac{1}{s_y}\frac{\partial H_{scat,y}}{\partial y}\right) \\ \quad + \frac{1}{s_z}\frac{\partial}{\partial z}\left(\frac{1}{s_z}\frac{\partial H_{scat,y}}{\partial z}\right) + \omega^2 \mu \varepsilon H_{scat,y} \\ \quad - \omega^2 (\mu_0 \varepsilon_0 - \mu \varepsilon) H_{inc,y}, \\ g_3 = \frac{1}{s_x}\frac{\partial}{\partial x}\left(\frac{1}{s_x}\frac{\partial H_{scat,z}}{\partial x}\right) + \frac{1}{s_y}\frac{\partial}{\partial y}\left(\frac{1}{s_y}\frac{\partial H_{scat,z}}{\partial y}\right) \\ \quad + \frac{1}{s_z}\frac{\partial}{\partial z}\left(\frac{1}{s_z}\frac{\partial H_{scat,z}}{\partial z}\right) + \omega^2 \mu \varepsilon H_{scat,z} \\ \quad - \omega^2 (\mu_0 \varepsilon_0 - \mu \varepsilon) H_{inc,z}, \end{cases} \quad (4)$$

where s_x, s_y, and s_z are parameters to define PML. The partial derivative of equation (4) can be obtained using automatic differentiation, which can be achieved by using the function torch.autograd.grad.

Then the network *NN* is trained to find the best *NN* parameters (θ^*) by minimizing the total loss defined by equation (2) via gradient optimizers, such as Adam and L-BFGS, until the loss is smaller than a threshold ε.

In our simulation, a fully connected neural network *NN* is selected, the input of the network is spatial coordinates, and the output is the real and imaginary parts of the magnetic field, i.e., in the case of a sphere, the network input is three-dimensional (x,y,z) and the output is six-dimensional ($\mathrm{Re}(H_i)$ and $\mathrm{Im}(H_i)$ with $i = x,y,z$). The network has many hidden layers and each hidden layer contains several neurons. Meanwhile, we use the L-BFGS algorithm for optimization, and the spatial coordinate points of each random sampling point are generated by Latin hypercube sampling, which is a very practical sampling method that can be achieved by calling function pyDOE, lhs.

III. NUMERICAL RESULTS AND DISCUSSION

In this section, we use the neural network given in Section II to simulate electromagnetic scattering by three-dimensional objects. After the neural network is first verified by the comparison of its results with the analytical results calculated by Mie theory by taking a sphere as the example of an object, the effects of the number of labeled data and network structure are mainly discussed.

Next, the method is used for the electromagnetic scattering by an ellipsoid.

A. Validation

To validate the feasibility of our proposed network, we choose a three-dimensional homogeneous sphere as an example to study the electromagnetic response.

In the calculation, the radius and the refractive index of the particle are $a = 2\lambda$ with λ being the wavelength and $m_1 = 1.51$, respectively.

The incident wave is a transverse magnetic (TM) polarized plane wave propagating along the x-axis, and its wavelength is $\lambda = 2\pi$. We set $N_b = 5000$, $N_s = 20000$, and $N_d = 10000$. The spatial coordinates of all randomly sampled points are generated using Latin hypercube sampling.

All labeled data are calculated using Mie theory. We use a fully connected neural network, which contains four hidden layers and has 250 neurons per layer. In simulation, we take the ratio of training set and test set as 9:1.

Figures 2–4 give the simulated magnetic fields in *xoy*, *xoz*, and *yoz* planes, respectively.

In each figure, the black circle indicates the object boundary.

Each figure includes six sub-figures, which are divided into two rows and three columns. The upper row gives the real part of H_z, and the lower row is the imaginary part. The left column gives the results predicted by PINNs (denoted by superscript P), the middle column gives the ground true results by the Mie theory (denoted by superscript T), and the right column gives the errors.

It can be observed from the first and second columns of Fig. 2 that in the *xoy* plane the results predicted by

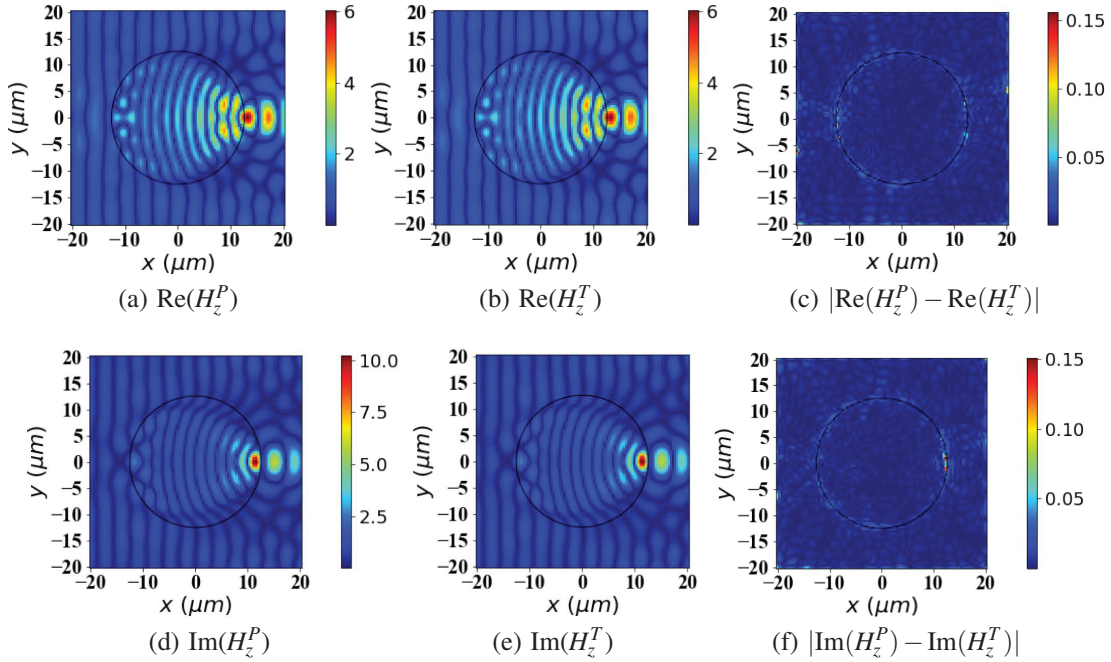

(a) $\mathrm{Re}(H_z^P)$ (b) $\mathrm{Re}(H_z^T)$ (c) $|\mathrm{Re}(H_z^P) - \mathrm{Re}(H_z^T)|$

(d) $\mathrm{Im}(H_z^P)$ (e) $\mathrm{Im}(H_z^T)$ (f) $|\mathrm{Im}(H_z^P) - \mathrm{Im}(H_z^T)|$

Fig. 2. Simulation results of the electromagnetic field in *xoy* plane.

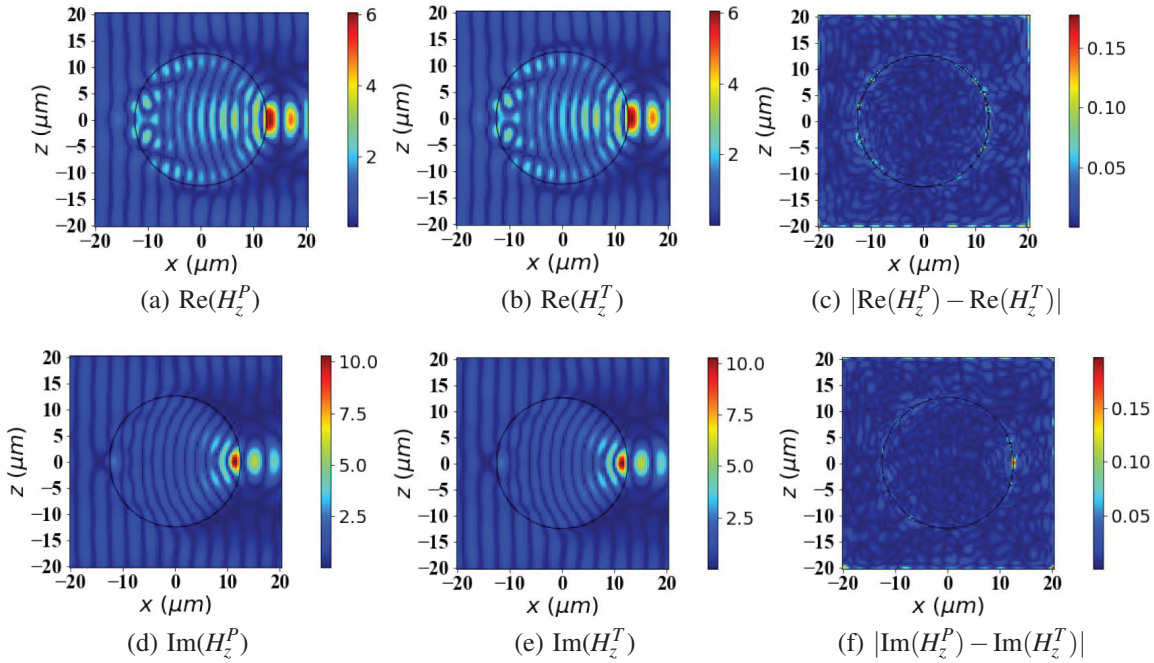

Fig. 3. Simulation results of the electromagnetic field in *xoz* plane.

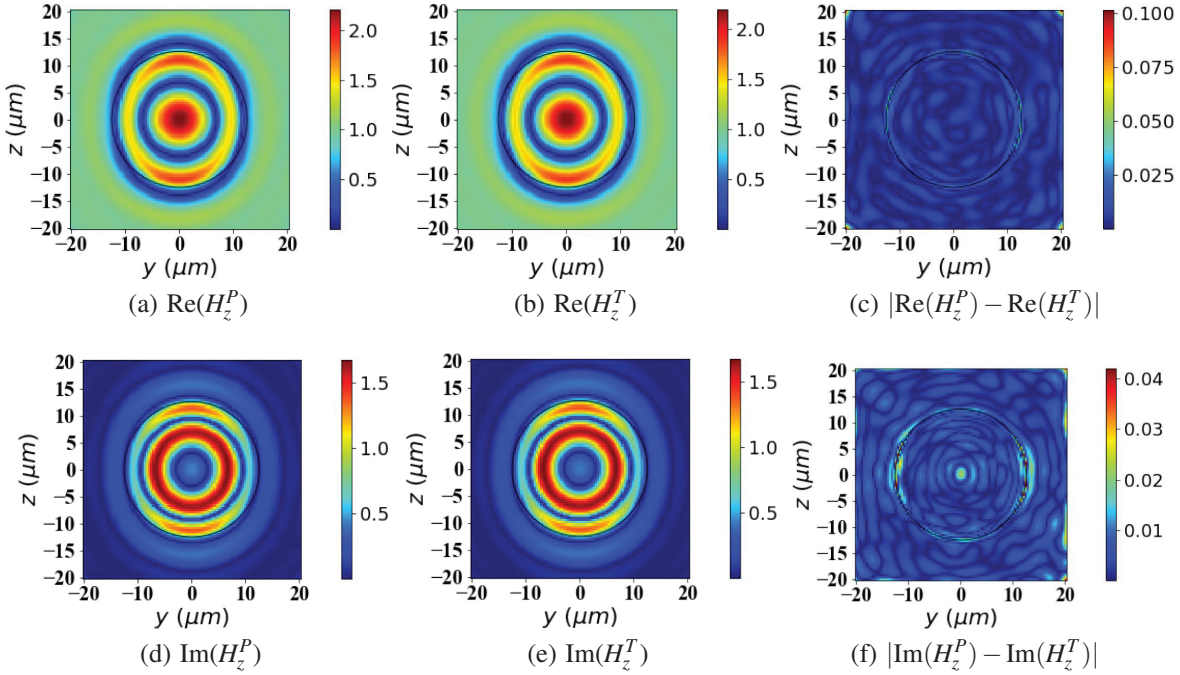

Fig. 4. Simulation results of the electromagnetic field in *yoz* plane.

the PINNs are in good agreement with the ground true values. From the right column of Fig. 2, we can see that the maximum absolute errors for the real and imaginary parts of H_z are respectively about 0.16 and 0.15, which correspond to the maximum relative errors about 2.5% and 1.5%. This indicates that the prediction accuracy of the network structure we built is high enough to achieve the results we expected. From *xoz* (Fig. 3) and

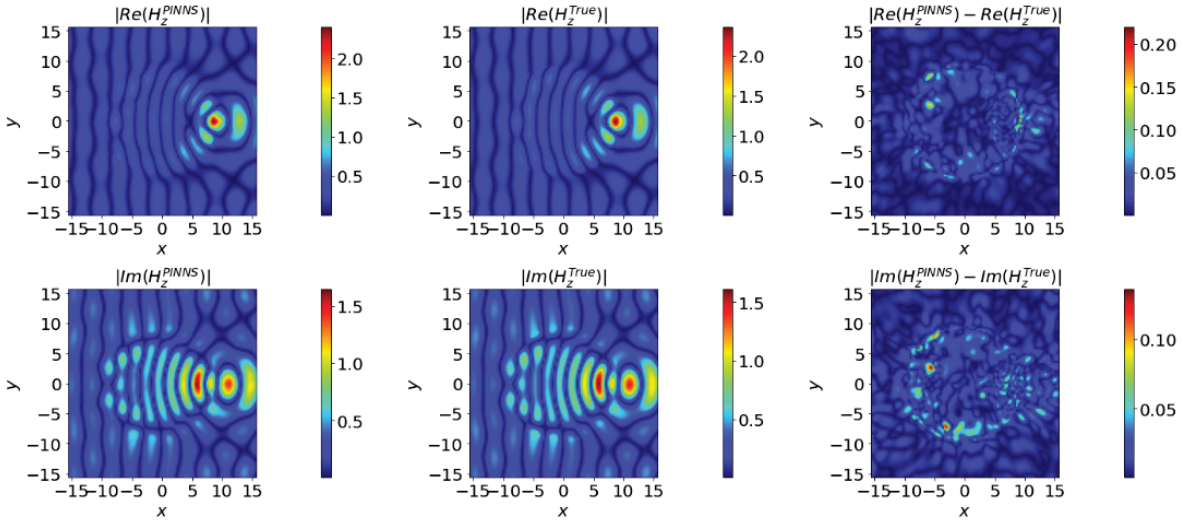

Fig. 5. Simulation results for the *xoy* plane electromagnetic field of an ellipsoid.

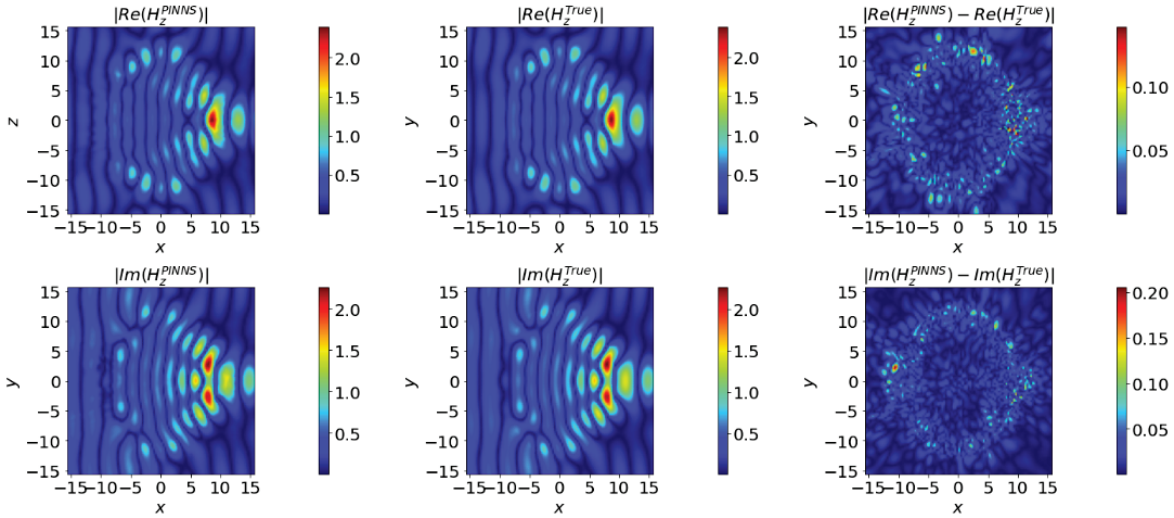

Fig. 6. Simulation results for the *xoz* plane electromagnetic field of an ellipsoid.

yoz (Fig. 4), we can also find the high accuracy of the PINNs.

It can be seen from the third column of Fig. 3 that the maximum absolute errors of the real and imaginary parts of H_z in the *xoz* plane are about 0.18 and 0.19, which correspond to the maximum relative errors 3% and 1.9%. Similar analysis shows that in the *yoz* plane the maximum absolute errors of the real and imaginary parts of H_z are about 0.1 and 0.04, which correspond to the maximum relative errors 5% and 2.5%.

B. Effect of labeled data

Theoretically, increasing the number of labeled data can lead to a more improved approximation of the neural network during training. Therefore, we investigate the effect of different amounts of labeled data on the prediction results by PINNs. In the calculation, all other conditions are consistent, and the number of labeled data varies. All the labeled data are calculated using Mie theory.

Table 1 gives the average absolute errors of results by PINNs with respect to that by Mie theory. The table has three columns. The first column is the number of labeled data. The second and third columns give the errors of the real and imaginary parts of H_z, respectively. From Table 1, we can see that the prediction accuracy gradually increases as the number of labeled data increases. This says that by adding labeled data

Table 1: Average absolute error versus labeled data number

Data	$\text{Error}_{\text{Hzr}}$	$\text{Error}_{\text{Hzi}}$
5000	5.193×10^{-3}	4.746×10^{-3}
10000	4.249×10^{-3}	4.055×10^{-3}
20000	3.523×10^{-3}	3.279×10^{-3}

we can obtain predicted results with higher accuracy. A reminder that in our calculation, the object is a sphere and the ground true results can be easily obtained using Mie theory. However, if the object is very complicated, it is hard to obtain a large number of labeled data.

C. Effect of network architecture

We also need to investigate the effect of parameter settings and the structure of neural networks on prediction accuracy. We vary the number of hidden layers (N_L) and the number of neurons per layer (N_N) to observe the change in prediction accuracy and evaluate the network training effect while keeping other parameters constant. The average absolute errors of H_z are shown in Table 2. The table has four columns and four rows. The first column gives the number of hidden layers N_L, and the second to fourth columns gives the errors for various number of neurons N_N. The first row gives the number of neurons N_N, and the second to fourth rows gives the errors for various number of hidden layers N_L. Note that all cells except the first row and column have two numbers. The upper number is the error of the real part of H_z, and the lower number is that for the imaginary part. As we expected, the network prediction accuracy improves as the number of layers and neurons increases.

Table 2: Average absolute error versus number of hidden layers (N_L) and neurons in each layer (N_N)

N_L \ N_N	150	200	250
3 Layers	1.253×10^{-2}	5.351×10^{-3}	6.674×10^{-3}
	1.167×10^{-2}	5.024×10^{-3}	6.005×10^{-3}
4 Layers	7.924×10^{-3}	5.035×10^{-3}	3.523×10^{-3}
	7.625×10^{-3}	4.625×10^{-3}	3.279×10^{-3}
5 Layers	5.190×10^{-3}	4.692×10^{-3}	3.429×10^{-3}
	4.713×10^{-3}	4.326×10^{-3}	3.248×10^{-3}

D. Further expansion

To explore the applicability of the proposed network in different scenarios, we also briefly investigate the electromagnetic response of 3D ellipsoidal particles. In the calculations, the major axis and minor axis of the ellipsoidal particles are $a = b = 3\pi$ and $c = 4\pi$, respectively, and all other parameters are the same as those of the spherical particles.

The simulated magnetic fields in the *xoy* and *xoz* planes are given in Figs. 5 and 6, respectively. Unlike the plot for the sphere, the middle column shows the true result derived by the FDFD (denoted by superscript T).

It can be seen that the predicted values of PINNs are in better agreement with the true values in the *xoy* and *xoz* planes.

From the right column of Fig. 5, we can see that the maximum absolute errors for the real and imaginary parts of H_z are respectively about 0.2 and 0.1, which correspond to maximum relative errors of about 10% in both cases.

From *xoz* (Fig. 6), we can see that the maximum absolute errors for the real and imaginary parts of H_z are respectively about 0.1 and 0.2, which correspond to the maximum relative errors about 5% and 10%.

The errors are concentrated at the edge positions of the ellipsoid, which we analyse to be due to the discontinuity of the dielectric constant at the edge positions. The PINN predictions match the true values at all positions except the edge position.

This shows that the prediction accuracy of our constructed network structure can reach our expected results.

IV. CONCLUSION

The electromagnetic scattering by a three-dimensional target is investigated using physics-informed neural networks (PINNs). Under the physical constraint of Maxwell's equations, the total magnetic fields of a TM plane wave scattering by a homogeneous sphere is predicted with high accuracy. The effects of the number of labeled data, and network structures on the prediction results are mainly discussed.

ACKNOWLEDGMENT

The authors acknowledge the support from the National Natural Science Foundation of China [62001345, 61901324, 61771375, 92052106], the open fund of Information Materials and Intelligent Sensing Laboratory of Anhui Province [IMIS202103], and the Project of Natural Science Research in Shanxi Province[202203021211095].

REFERENCES

[1] M. S. Zhdanov, *Geophysical Inverse Theory and Regularization Problems*, vol. 36, Amsterdam: Elsevier, 2002.

[2] A. Abubakar, P. M. Van den Berg, and J. J. Mallorqui, "Imaging of biomedical data using a multiplicative regularized contrast source inversion method," *IEEE Transactions on Microwave Theory and Techniques*, vol. 50, no. 7, pp. 1761-1771, 2002.

[3] X. Wang, T. Qin, R. S. Witte, and H. Xin, "Computational feasibility study of contrast-enhanced thermoacoustic imaging for breast cancer detection using realistic numerical breast phantoms," *IEEE Transactions on Microwave Theory and Techniques*, vol. 63, no. 5, pp. 1489-1501, 2015.

[4] C. A. Balanis, *Antenna Theory: Analysis and Design*, New York: Wiley, 2016.

[5] A. Taflove, S. C. Hagness, and M. Piket-May, "Computational electromagnetics: The finite-difference time-domain method," *The Electrical Engineering Handbook*, vol. 3, pp. 629-670, 2005.

[6] K. Yee, "Numerical solution of initial boundary value problems involving Maxwell's equations in isotropic media," *IEEE Transactions on Antennas and Propagation*, vol. 14, no. 3, pp. 302-307, 1966.

[7] J.-M. Jin, *The Finite Element Method in Electromagnetics*, New York: Wiley, 2015.

[8] R. C. Rumpf, "Simple implementation of arbitrarily shaped total-field/scattered-field regions in finite-difference frequency-domain," *Progress In Electromagnetics Research B*, vol. 36, pp. 221-248, 2012.

[9] J. Smajic, C. Hafner, L. Raguin, K. Tavzarashvili, and M. Mishrikey, "Comparison of numerical methods for the analysis of plasmonic structures," *Journal of Computational and Theoretical Nanoscience*, vol. 6, no. 3, pp. 763-774, 2009.

[10] A. Massa, D. Marcantonio, X. Chen, M. Li, and M. Salucci, "DNNs as applied to electromagnetics, antennas, and propagation—A review," *IEEE Antennas and Wireless Propagation Letters*, vol. 18, no. 11, pp. 2225-2229, 2019.

[11] Y. Li, Y. Wang, S. Qi, Q. Ren, L. Kang, S. D. Campbell, P. L. Werner, and D. H. Werner, "Predicting scattering from complex nano-structures via deep learning," *IEEE Access*, vol. 8, pp. 139983-139993, 2020.

[12] I. E. Lagaris, A. Likas, and D. I. Fotiadis, "Artificial neural networks for solving ordinary an partial differential equations," *IEEE Transactions on Neural Networks*, vol. 9, no. 5, pp. 987-1000, 1998.

[13] M. Raissi, P. Perdikaris, and G. E. Karniadakis, "Physics-informed neural networks: A deep learning framework for solving forward and inverse problems involving nonlinear partial differential equations," *Journal of Computational Physics*, vol. 378, pp. 686-707, 2019.

[14] L. D. Landau, *The Classical Theory of Fields*, vol. 2, Amsterdam: Elsevier, 2013.

Yuan Zhang received the B.S. degree from Xidian University, Xi'an, China, in 2021. She is currently working toward the M.S. degree in Optics, Xidian University. Her research interests include machine learning, and computational electromagnetism.

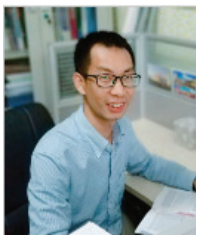

Renxian Li received the Ph.D. degree from Xidian University in 2008. After graduation, he joined the School of Physics, Xidian University. His research interests includes machine learning, electromagnetic scattering, and computational electromagnetism.

Huan Tang received the B.S. degree from Xidian University, Xi'an, China, in 2020. He is currently working toward the Ph.D. degree in Optics, Xidian University. His research interests include neural network, and electromagnetic scattering.

Zhuoyuan Shi received the B.S. degree from Xidian University, Xi'an, China, in 2022. She is currently working toward the M.S. degree in Optics, Xidian University. Her research interests include machine learning, and electromagnetic scattering.

Bing Wei was born in July 1970, graduated from Beijing Normal University in 1993, majoring in Solid State and Ion Beam Physics, and received his Ph.D. degree in Radio Physics from Xidian University of Electronic Science and Technology (XUET) in 2004. He is now a professor of Xidian University of Electronic Science and Technology (XUET), a doctoral supervisor of radio

physics, and a vice dean of the School of Physics. His main research interests include electromagnetic theory, computational electromagnetics, simulation of target time-domain response, and integrated time-domain measurements.

Shuhong Gong was born in Shanxi, China, in 1978. He received the B.S. degree in physics education from Shanxi Normal University, Xi'an, China, in 2001, the M.S. and Ph.D. degrees in radio physics from Xidian University, Xi'an, in 2004 and 2008, respectively. He is currently a Professor at Xidian University. His research work has been focused on novel antenna design, radio wave propagation, and their applications.

Lixia Yang was born in Ezhou, Hubei, China, in 1975. He received the B.S. degree in physics from Hubei University, Wuhan, China, in 1997, and the Ph.D. degree in radio physics from Xidian University, Xi'an, China, in 2007. Since 2010, he has been an Associate Professor with the Communication Engineering Department, Jiangsu University, Zhenjiang, China. From 2010 to 2011, he was a Postdoctoral Research Fellow with the Electro Science Laboratory (ESL), The Ohio State University, Columbus, OH, USA. From 2015 to 2016, he was a Visiting Scholar with the Institute of Space Science, The University of Texas at Dallas, Dallas, TX, USA. From 2016 to 2019, he has been a Professor, a Ph.D. Supervisor, and the Chairman of the Communication Engineering Department, Jiangsu University. Since 2020, he has been a Distinguished Professor, a Ph.D. Supervisor, and the Vice Dean with the School of Electronic and Information Engineering, Anhui University, Hefei, China. His research interests include wireless communication technique, radio sciences, the computational electromagnetic, and the antenna theory and design in wireless communication systems. He is a member of the Editor Board of Radio Science Journal in China.

Bing Yan was born on October 6, 1976. From 2004 to 2009, he studied in the School of Science, Xidian University, and received his doctorate. In recent years, his interesting has been engaged in the research of gas-solid two-phase flow multiparameter measurement based on light scattering method and electrostatic method.

Study on MPI-based Parallel FDTD Method of Moving Target Coated with Time-varying Plasma

Hai-Yan Li[1], Xian-Min Guo[1], Yong Bo[1,2], Wei Chen[1], Li-Xia Yang[1], Zhi-Xiang Huang[1], Jia-Chen Wang[1], and Xin-Jie Duan[1]

[1]Information Materials and Intelligent Sensing Laboratory of Anhui Province
Anhui University, Hefei, 230601, China
p21201066@stu.ahu.edu.cn, p21301162@stu.ahu.edu.cn, boyong@ahu.edu.cn, chenwei1704@126.com, lixiayang@yeah.net, zxhuang@ahu.edu.cn, p02114038@stu.ahu.edu.cn, 1392626588@qq.com

[2]East China Research Institute of Electronic Engineering
Hefei, China
boyong@ahu.edu.cn

***Abstract* –** Analyzing the electromagnetic (EM) scattering properties of high-speed moving objects is a hot research topic in recent years. However, EM calculations for high-speed moving targets always involve challenges of high computational complexity and low computational efficiency. In this paper, we integrate the Message Passing Interface (MPI) based parallel finite difference time domain (FDTD) method and Lorentz transformation to calculate the EM scattering of a moving metal sphere coated with time-varying plasma. Subsequently, by comparing the outcomes of the proposed Parallel FDTD approach with the serial computing results, the validity of the Parallel FDTD method is validated. Additionally, for a moving and time-varying plasma sheath coated object, the impacts of the time-varying parameters and plasma parameters on the EM scattering properties are investigated using the Parallel FDTD approach. The results indicated that the MPI-Based Parallel FDTD approach displays almost identical precision as the serial approach. Furthermore, the Parallel FDTD approach can enhance computation speed and significantly reduce the computation time.

***Index Terms* –** electromagnetic (EM) properties, Lorentz transformation, Message Passing Interface (MPI), moving target, Parallel finite difference time domain (FDTD) method, time-varying plasma.

I. INTRODUCTION

Research on the electromagnetic (EM) scattering of high-speed moving targets is a popular research topic due to its broad range of applications in identifying moving targets and exploring deep space [1–8] such as detection and identification of moving satellites, aircraft, and ships. Furthermore, investigating the interaction between EM and moving targets is crucial for understanding the propagation principle of EM waves in complex media and improving the performance of wireless communication and radar systems. Harfoush et al. [4] utilized relativistic boundary conditions (RBC) based on the finite difference time domain (FDTD) approach to investigate the scattering field from one-dimensional (1-D) and two-dimensional (2-D) conducting moving objects. Zheng et al. [5] proposed the representation of the incident wave in the Lorentz-FDTD method and analyzed the double-Doppler effect from a moving dielectric target. Zhang and Nie [6] proposed the combined method of the RBC and the FDTD to calculate the radar cross-section (RCS) of a moving metal target. Zheng et al. [7] analyzed the scattered fields from a moving conducting target, and the results show that the amplitude and frequency of scattered fields are modulated by the velocity of the target. Zheng et al. [8] studied the micro-motion state of a moving target using the Lorentz-FDTD algorithm, and discussed the effect of the micro-motion state on EM echo. The EM scattering of high-speed moving dielectric or metallic targets has been extensively analyzed. However, there is still a lack of research on the EM scattering analysis of moving dispersive media.

The FDTD method is a widely used approach for solving EM problems and has been extensively applied in EM scattering calculations [9–12]. However, the calculation accuracy and stability are limited by the spatial and temporal discretization sizes in FDTD. Therefore, traditional serial FDTD methods are inadequate for large-scale EM calculations, as they cannot meet the requirements of high computing speed and large memory computation. To address these issues, an increasing number of researchers are adopting the FDTD method

Submitted On: July 27, 2023
Accepted On: December 12, 2023

https://doi.org/10.13052/2025.ACES.J.400204

combined with parallel calculation methods for EM scattering calculations to achieve higher computational efficiency. Varadaraian and Mittra [13] utilized Parallel Virtual Machine (PVM) to implement Parallel FDTD simulations and investigated the three-dimensional (3-D) rectangular resonant cavity problem. Guiffaut and Mahdjoubi [14] developed a Parallel FDTD computations method based on the Message Passing Interface (MPI). Stefanski and Drysdale [15] were the first to implement parallel acceleration in the EM problem calculation of the anisotropic medium with alternating direction implicit FDTD (ADI-FDTD) method. Duan et al. [16] implemented a high-performance Parallel FDTD computation on multi-core of PC-Cluster using Winsock and multi-threaded method, and the results show that this method can significantly speed up the computation as well as improve the computation efficiency. Mao et al. [17] analyzed two different moving window FDTD (MW-FDTD) parallel approaches to simulate the EM propagation in tunnels, and both methods have high accuracy. Chakarothai et al. [18] developed a large-scale Parallel FDTD method using the GPU cluster of the TSUBAME system for numerical exposure of a human body to EM fields. Lei et al. [19] studied the scattering properties of electrically large coated objects, such as warships and planes, by employing the MPI-Based Parallel FDTD approach. Yang and colleagues proposed a 3-D parallel anisotropic medium FDTD method for the EM computations in anisotropic media [20–22]. Duan et al. [23] introduced the parallel Auxiliary Differential Equation FDTD (ADE-FDTD) method to solve the EM problems of plasma, which can reduce calculation time. Wang et al. [24] proposed a novel conformal surface current approach based on the Parallel FDTD method, providing a potential solution for handling large-scale EM calculation problems. Shi et al. [25] investigated a hybrid Parallel FDTD algorithm to solve EM scattering calculations of electrically large objects, and the results indicate that this approach can improve computing speed.

When applying the Lorentz-FDTD method to investigate time-varying and moving dispersive medium targets, the considerable computational effort is required for EM calculation. Therefore, the application of parallel Lorentz-FDTD methods for analyzing time-varying and moving plasmas is meaningful. Considering that the plasma sheath generated around high-speed moving targets is always time-varying, this paper combines the MPI-Based Parallel FDTD method with Lorentz transformation to calculate the EM scattering properties of a moving object coated with time-varying plasma. By integrating parallel processing techniques, the FDTD method can significantly accelerate the computation process and reduce computation time, thereby expanding the scope of applications for numerical simulation methods.

II. METHOD

In this section, the Lorentz transformation, Parallel FDTD method, and ADE-FDTD method will be discussed.

A. Lorentz transformation

In the analysis of EM scattering problems from moving targets, as shown in Fig. 1, two reference frames are considered: a moving reference frame K' and a laboratory reference frame K. Here, the target moves at the speed $\vec{v}$ in the system K, and the system K' moves at the same speed $\vec{v}$ relative to system K. Thus, the target is stationary in the system K'. Due to relativistic covariance, EM scattering problem of the moving target can be transformed into the moving reference frame for a solution.

(1) Time and space increment transformation

When performing the EM calculation for a moving dispersive medium target, the time and space increment need to be transformed between the reference frame K' and K. Assuming the target moving at the velocity $\vec{v}$, the time and space increment transformation formulas between these two reference frames are as shown in (1)–(4):

$$\Delta x = \left[1+\frac{v_x^2}{v^2}(\gamma-1)\right]\Delta x' + \frac{v_x v_y}{v^2}(\gamma-1)\Delta y' + \frac{v_x v_z}{v^2}(\gamma-1)\Delta z', \quad (1)$$

$$\Delta y = \frac{v_x v_y}{v^2}(\gamma-1)\Delta x' + \left[1+\frac{v_y^2}{v^2}(\gamma-1)\right]\Delta y' + \frac{v_y v_z}{v^2}(\gamma-1)\Delta z', \quad (2)$$

$$\Delta z = \frac{v_x v_z}{v^2}(\gamma-1)\Delta x' + \frac{v_y v_z}{v^2}(\gamma-1)\Delta y' + \left[1+\frac{v_z^2}{v^2}(\gamma-1)\right]\Delta z', \quad (3)$$

$$\Delta t = \frac{1}{\sqrt{1-\beta^2}}\left(1-\beta\left(\hat{a}_s\cdot\hat{a}_v\right)\right)\Delta t', \quad (4)$$

where $\gamma = 1/\sqrt{1-\beta^2}$, $\beta = v/c$, and c is the speed of light in free space, v is the speed of the target. $v_x = |\vec{v}|\sin\theta_v\cos\varphi_v v_y = |\vec{v}|\sin\theta_v\sin\varphi_v$, $v_z = |\vec{v}|\cos\theta_v$. The θ_v denotes the angel between $\vec{v}$ and $+z$ axis, and the φ_v denotes the angle between the projection of $\vec{v}$ on xOy and $+x$ axis.

(2) Introduction of incident waves

When converting the EM problems to the reference frame K', the incident wave defined in the reference frame K also needs to be introduced into the reference frame K'. According to the principle of the phase invariance of Lorentz transformation in (5), the amplitude and frequency of the incident wave in the reference frame K' are obtained by (6)–(7):

$$\omega_i t - xk_i\sin\theta_i\cos\varphi_i - yk_i\sin\theta_i\sin\varphi_i - zk_i\cos\theta_i \equiv$$

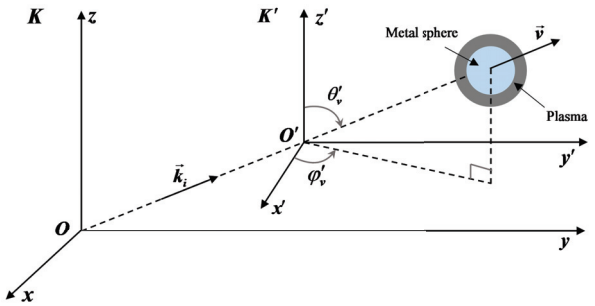

Fig. 1. The two reference frames of Lorentz-FDTD.

$$\omega_i' t' - x' k_i' \sin\theta_i' \cos\varphi_i' - y' k_i' \sin\theta_i' \sin\varphi_i' - z' k_i' \cos\theta_i', \tag{5}$$

$$|E_0'| = \sqrt{(E_0 \cos\psi)^2 + \gamma^2 \left(E_0 \sin\psi + |\vec{v} \times \vec{B}|\right)^2}, \tag{6}$$

$$\omega_i' = \omega\gamma[1 - \beta(\hat{a}_i \cdot \hat{a}_v)], \tag{7}$$

where ω_i, E_0 denotes the frequency and amplitude of the incident wave in the reference frame K. The θ_i is the angle between the incident wave vector $\vec{k}_i$ and the $+z$ axis, and φ_i is the angle between the projection of the incident wave vector $\vec{k}_i$ in the xoy plane and the $+x$ axis. And ψ is the angle between the incident electric field and the velocity of the target, $\cos\psi = \hat{a}_E \cdot \hat{a}_v$.

(3) EM fields transformation

After introducing the incident wave into the reference frame K', the EM scattered fields can be calculated using the FDTD method. Since the EM fields in the two reference frames follow the Lorentz transformation [26], the EM scattered field components can be derived by performing the inverse Lorentz transformation. The transformation formulas are shown in (8)–(9):

$$\boldsymbol{E} = \gamma\left(\boldsymbol{E}' - \boldsymbol{v} \times \boldsymbol{B}'\right) + (1+\gamma)\frac{\boldsymbol{E}' \cdot \boldsymbol{v}}{v^2}\boldsymbol{v}, \tag{8}$$

$$\boldsymbol{B} = \gamma\left(\boldsymbol{B}' - \frac{1}{c^2}\boldsymbol{v} \times \boldsymbol{E}'\right) + (1-\gamma)\frac{\boldsymbol{B}' \cdot \boldsymbol{v}}{v^2}\boldsymbol{v}. \tag{9}$$

B. Auxiliary Differential Equation (ADE)-FDTD method

Maxwell's equations in the collision non-magnetized plasma are given as follows [9]:

$$\nabla \times \boldsymbol{E} = -\frac{\partial \boldsymbol{B}}{\partial t}, \tag{10}$$

$$\nabla \times \boldsymbol{H} = \frac{\partial \boldsymbol{D}}{\partial t} + \boldsymbol{J}, \tag{11}$$

$$\boldsymbol{D}(\omega) = \varepsilon(\omega)\boldsymbol{E}(\omega), \tag{12}$$

where the frequency domain expression for the polarization current $\boldsymbol{J}_p$ is:

$$\boldsymbol{J}_p = \mathrm{j}\omega\varepsilon_0\chi(\omega)\boldsymbol{E}(\omega). \tag{13}$$

According to (12), the intrinsic relationship in the frequency domain for the dielectric coefficient is:

$$\boldsymbol{D}(\omega) = \varepsilon(\omega)\boldsymbol{E}(\omega) = \varepsilon_0[\varepsilon_\infty + \chi(\omega)]\boldsymbol{E}(\omega)$$

$$= \varepsilon_0\varepsilon_\infty\boldsymbol{E}(\omega) + \varepsilon_0\chi(\omega)\boldsymbol{E}(\omega), \tag{14}$$

where $\varepsilon(\omega)$ denotes the dielectric coefficient of the plasma, and $\chi(\omega)$ is the polarization rate of the plasma.

(1) ADE-FDTD for Drude model

The polarization rate of the Drude medium is described as follows:

$$\chi(\omega) = \frac{\omega_p^2}{\omega(\omega - j\nu_c)}. \tag{15}$$

Substituting equation (15) into (13):

$$\boldsymbol{J}_p(\omega) = \mathrm{j}\omega\varepsilon_0\frac{\omega_p^2}{\omega(\omega - j\nu_c)}\boldsymbol{E}(\omega). \tag{16}$$

By applying the operator conversion relation $j\omega \to \partial/\partial t$ from the frequency domain to the time domain [27], equation (16) transforms to:

$$\frac{\partial^2 \boldsymbol{J}_p}{\partial t^2} + \nu_c\frac{\partial \boldsymbol{J}_p}{\partial t} = -\varepsilon_0\omega_p^2(t)\frac{\partial \boldsymbol{E}}{\partial t}. \tag{17}$$

By integrating both sides of equation (17), the iterative formula of $\boldsymbol{J}_p$ shown in equation (18) is obtained after discretizing the differential equation. The coefficients are presented in equation (19):

$$\boldsymbol{J}_p{}^{n+1} = k_p\boldsymbol{J}_p{}^n + \beta_p\left(\boldsymbol{E}^{n+1} + \boldsymbol{E}^n\right). \tag{18}$$

The coefficient in (18) is shown in (19):

$$\begin{cases} k_p = \frac{2-\nu_c\Delta t}{2+\nu_c\Delta t} \\ \beta_p = \frac{\omega_p^2(t)\varepsilon_0\Delta t}{2+\nu_c\Delta t} \end{cases}. \tag{19}$$

Substituting equation (18) into (13), and then the iterative formula for electric field is obtained:

$$\boldsymbol{E}^{n+1} = \mathrm{CA} \bullet \boldsymbol{E}^n + \mathrm{CB} \bullet \left\{[\nabla \times \boldsymbol{H}]^{n+1/2} - \frac{1}{2}(1+k_p)\boldsymbol{J}_p{}^n\right\}, \tag{20}$$

$$\begin{cases} \mathrm{CA} = \frac{2\varepsilon_0\varepsilon_\infty - \sigma\Delta t + \beta_p\Delta t}{2\varepsilon_0\varepsilon_\infty + \sigma\Delta t - \beta_p\Delta t} \\ \mathrm{CB} = \frac{2\Delta t}{2\varepsilon_0\varepsilon_\infty + \sigma\Delta t - \beta_p\Delta t} \end{cases}. \tag{21}$$

(2) FDTD computational region

For EM scattering problems, a connecting boundary is typically introduced within the FDTD computational region. When FDTD is applied to scattered field calculations, the FDTD computation area is divided into a total field region and a scattered field region. To model EM problems in unbounded space within a limited computational region, absorbing boundary conditions are necessary on the truncated boundaries of the computational region. To obtain the scattered field outside of the computational domain, using the equivalence principle, the far-zone scattered field can be obtained from the near-zone scattered field by at the output boundary. The division of the FDTD computational region is shown in Fig. 2.

C. Parallel FDTD method

In this paper, a combined mode of master-slave and peer-to-peer modes are adopted for the calculation of

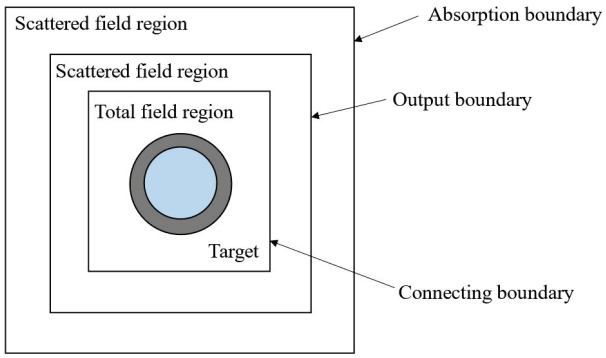

Fig. 2. The division of the FDTD computational region.

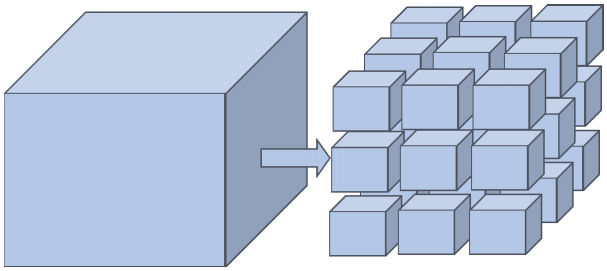

Fig. 3. Region divide using the 3-D mode.

EM scattering from a moving metal coated with time-varying plasma. The detailed flowcharts of the master process and slave processes are shown in Figs. 4 and 5, respectively. By using the Parallel FDTD method, we can significantly improve resource utilization and reduce the calculation time, especially when the hardware resources are limited.

In the master process, prior to employing the Parallel FDTD method for EM calculations, the FDTD calculation area is initially divided into sub-domains. A 3-D region dividing approach is adopted in this paper, as illustrated in Fig. 3. When the region is divided into sub-domains, each sub-domain can exchange information with one another.

As Fig. 4 illustrates, the master process is primarily responsible for assigning computation tasks to each slave process and collecting and processing data once all slave processes have completed their computation tasks.

As shown in Fig. 5, the slave processes are accountable for receiving the tasks assigned by the master process. Each process performs the iterative update of EM fields using the ADE-FDTD method, along with the computation of the connection boundary, absorption boundary, and output boundary. Once all processes have completed their calculation tasks, the calculation results are transmitted to the master process.

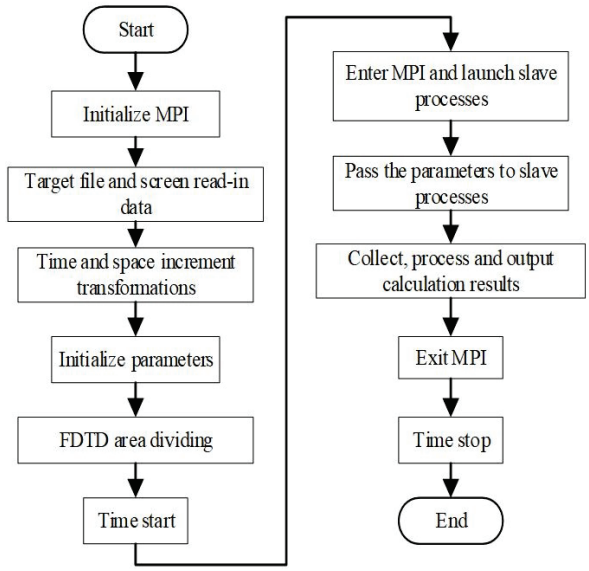

Fig. 4. The flowchart of the master process in Parallel FDTD method.

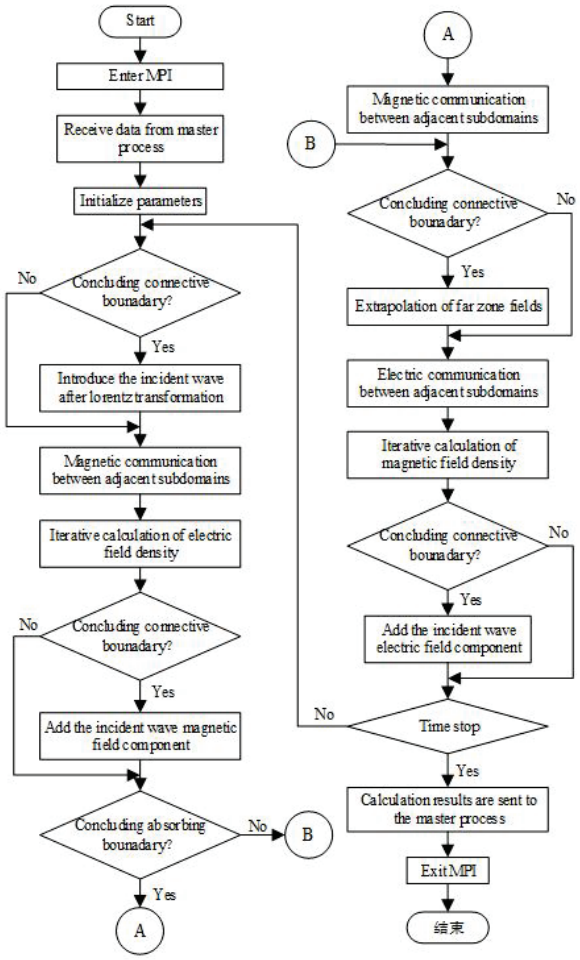

Fig. 5. The flowchart of the slave processes in Parallel FDTD method.

III. NUMERICAL RESULTS

A. Validation of parallel Lorentz-FDTD method

As an example, the scattered fields in the time domain and the monostatic RCS from a plasma sphere are calculated. The radius of the plasma sphere is 10 cm. In this section, the serial calculation results are compared with the parallel calculation results and the results of the plasma sphere with $v = 0$ m/s calculated by the parallel Lorentz-FDTD are compared with the results calculated using the ADE-FDTD method.

The space increment is set as $dx' = dy' = dz' = 0.005$ m, and the time increment satisfies the Courant stability criterion: $dt' \leq dx'/\sqrt{3}c$, c is the is the speed of light in free space. The incident direction is $\theta_i = 0°$, $\varphi_i = 0°$ and $\alpha = 0°$. The receive angle of the scattered wave is $\theta_s = 180°$, $\varphi_s = 180°$.

As shown in Figs. 6 (a) and (b), the corresponding time-domain scattered field and RCS results calculated with serial and parallel methods are presented when the target velocity is 0 m/s. In addition, the results calculated by the parallel Lorentz-FDTD method when $v = 0$ are also compared with the conventional ADE-FDTD results. From Figs. 6 (a) and (b), it can be seen that the serial and parallel results agree well, and the results of the Lorentz-FDTD method are also consistent with the conventional ADE-FDTD method, so the validity and accuracy of the parallel Lorentz-FDTD method is verified.

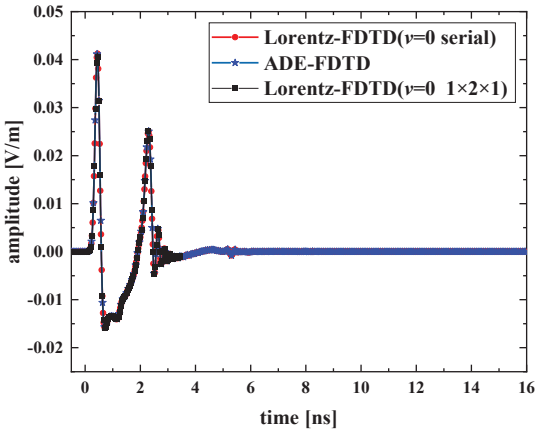

(a)

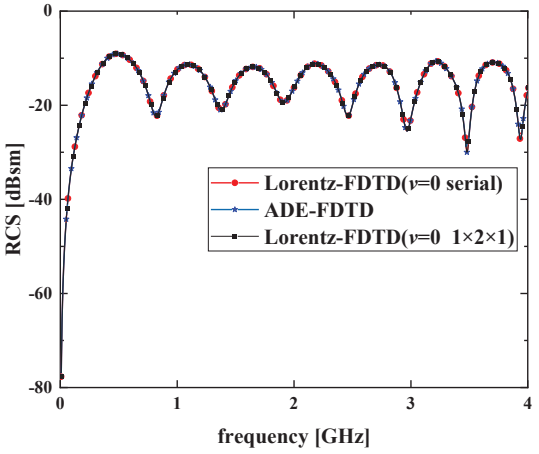

(b)

Fig. 6. The validation of parallel Lorentz-FDTD method: (a) scattering fields in the time domain and (b) monostatic RCS.

Figure 7 presents the monostatic RCS results calculated using the serial and parallel method when the plasma sphere is moving at $v = 0.01c$. The results in Fig. 7 demonstrate that the serial and parallel calculations are in good agreement. Thus, the Parallel FDTD method has almost the same precision as the serial computation when calculating the EM scattering from moving targets.

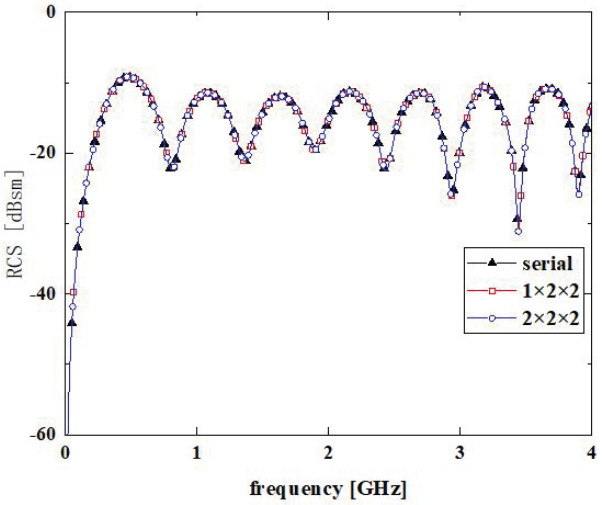

Fig. 7. Monostatic RCS of the plasma sphere moving at $v = 0.01c$.

B. EM scattering properties of moving metal sphere coated time-varying plasma sheath

In the simulation of this section, the EM scattering properties from a moving 3-D metal sphere coated with time-varying plasma are calculated and analyzed. A Gaussian pulse wave with an amplitude of 1 V/m, and $\tau = 1.7/B$, B =4GHz, and $t_0 = 0.8\tau$. The amplitude of the incident wave in the frame K' can be derived using the Lorentz transformation. The formula of the incident wave source in the frame K' is as show in (22). The space grid is set as $dx' = dy' = dz' = \delta = 0.0037m$, and the time increment satisfies the Courant stability criterion: $dt' \leq dx'/\sqrt{3}c$. The radius of the metal sphere is 40δ, and the thickness of the plasma is 5δ. The direction

of the incident wave is $\theta_i = 90^\circ$ and $\varphi_i = 90^\circ$:

$$E_i'(t') = E_0' \exp\left(-\frac{4\pi\gamma_t^2 (t'-t_0)^2}{\tau^2}\right), \quad (22)$$

$$\gamma_t = \gamma[1-\beta(\hat{a}_i \cdot \hat{a}_v)], \quad (23)$$

where E_0' is the amplitude of incident wave in the system K', and $\hat{a}_i \cdot \hat{a}_v$ denotes the dot product of the unit vector of the incident wave and the unit vector of the speed.

The time-varying electron density of the plasma is described as follows:

$$Ne(t) = Neavg(1+\Delta Ne(\sin(2\pi f_0 t))), \quad (24)$$

where $Neavg = 3\times10^{18}$ m^{-3} denotes the average electron density of the time-varying plasma, $\Delta Ne = 0.3$ denotes the variation range of electron density, and f_0 = 80 MHz is the time-varying frequency.

Figure 8 (a) displays the scattering fields in the time domain for targets moving at velocities of $v = 0$, 0.05c, and 0.1c. The results indicate that when the target's motion direction is aligned with the incident direction, the scattered wave experiences a delay in the time domain. Moreover, the greater the velocity, the greater the delay. Surprisingly, the amplitude of the scattered wave increases slightly with an increase in velocity. As shown in Fig. 8 (b), a monostatic RCS is observed with a shift towards the low-frequency band if the target moves along the incident direction (v>0). Moreover, the higher the speed, the more evident the RCS shift towards the lower frequency band.

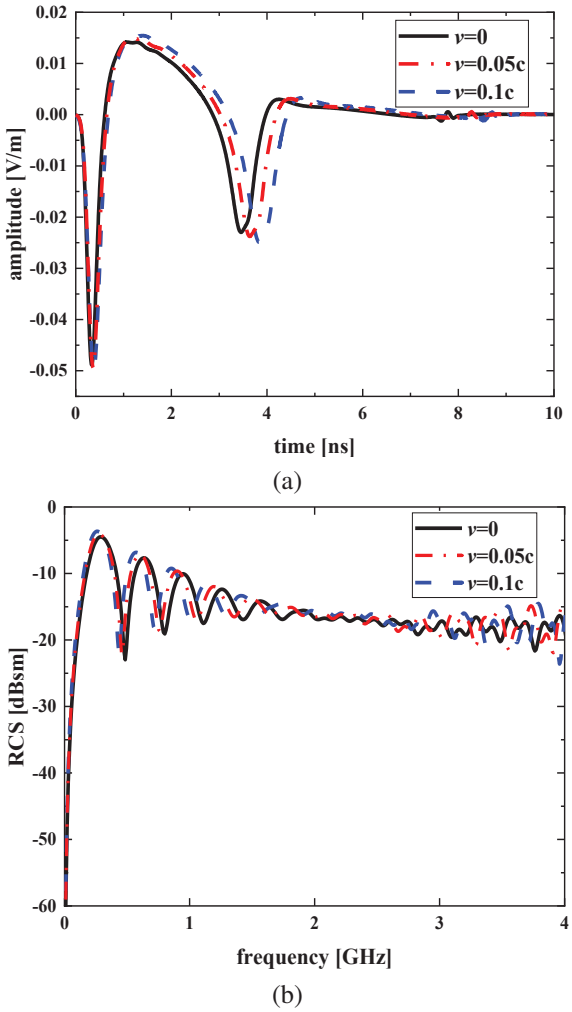

Fig. 8. Scattered field results of metal sphere coated with time-varying plasma at different velocities: (a) scattered fields in the time domain and (b) monostatic RCS.

Table 1 presents the serial and parallel computing times for three different speeds when the partitioning mode is the same (both 2×2×2) but the total running time steps are different. Besides, the parallel acceleration ratio (S_p) was calculated according to the serial and parallel computing times. The results in Table 1 indicate that, for three different motion speeds, the simulation time used by the parallel method is different when the total simulation time step is different but the target motion speed and the computational region are divided in the same way. Moreover, it can be seen from the data in Table 1 that the larger the total running time step, the higher the parallel acceleration ratio. A larger time step indicates a higher computational complexity. This implies that the Parallel FDTD algorithm for EM scattering calculations of moving targets coated with time-varying plasma sheath computes faster and more efficient when the computational complexity is higher.

Next, the effect of different plasma time-varying parameters on target EM scattering will be discussed, respectively.

Figure 9 displays the monostatic RCS for different average electron densities *Neavg* of the time-varying plasma when the target moves along the $+y$ axis at a velocity of $v = 30Mach$. The partitioning mode is set as 1×2×1. From Fig. 9, it can be seen that as the average electron density of time-varying plasma increases, the RCS also increases continuously. This is because a

Table 1: The calculation time comparison between the parallel Lorentz-FDTD method and the serial method

v (m/s)	Time Steps	Serial Time (s)	Parallel Time (s)	S_p
0	6500	4002.7243	812.7958	4.925
	8000	5479.5720	999.8317	5.480
	10000	8847.1129	1360.779	6.502
0.05	6500	3742.7816	1044.247	3.584
	8000	4240.9656	1064.220	3.985
	10000	5951.7948	1183.002	5.031
0.1	6500	4022.4639	1090.065	3.690
	8000	4196.1614	1104.651	3.799
	10000	5291.8946	1219.548	4.339

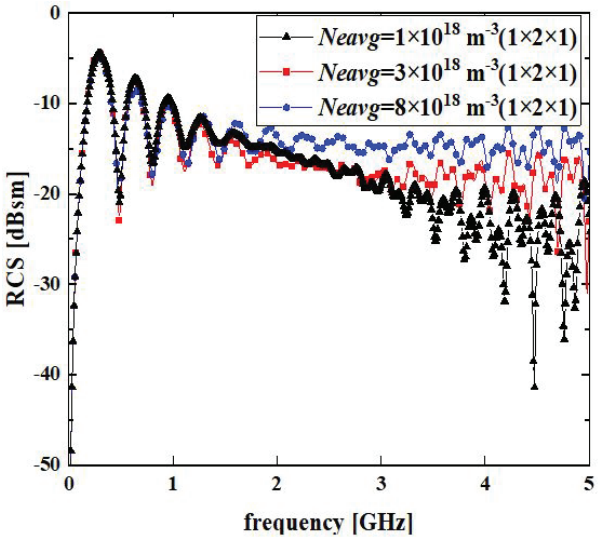

Fig. 9. Monostatic RCS of metal sphere coated with time-varying plasma under different average electron densities *Neavg*.

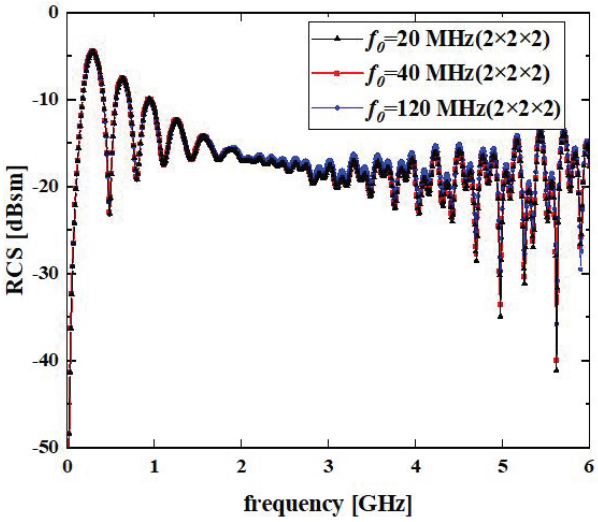

Fig. 11. Monostatic RCS of metal sphere coated with time-varying plasma under different time-varying frequencies f_0.

higher average electron density corresponds a higher the cutoff frequency of the plasma and stronger ability of the plasma sheath to backscatter the EM waves. This is because the time-varying characteristic of the electron density in the plasma sheath causes the cutoff frequency to vary with time, resulting in oscillations in the backward RCS.

Figure 10 presents the monostatic RCS for different variation ranges of electron density of the time-varying plasma ΔNe. The partitioning mode is set as $2\times2\times1$. As observed in Fig. 10, the monostatic RCS increases slightly with ΔNe. The main reason is that when ΔNe changes, the range of variation in plasma electron density is small. Therefore, the reflection ability of the plasma sheath on the EM wave has little effect, which leading to minimal changes in the backward RCS.

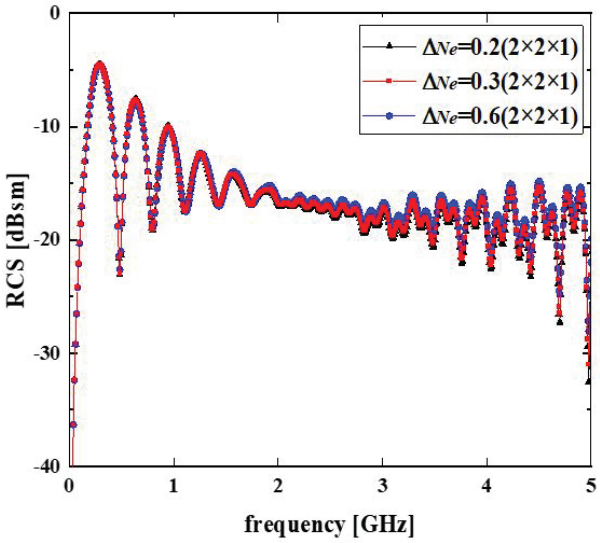

Fig. 10. Monostatic RCS of metal sphere coated with time-varying plasma under different ΔNe.

Figure 11 displays the monostatic RCS for different time-varying frequencies of the plasma. The total time step is set as 40000, and we choose the partitioning mode $2\times2\times2$ to speed up the simulation time. As shown in Fig. 11, it can be seen that monostatic RCS remains nearly invariant with the time-varying frequency f_0. This is because the average electron density remains unchanged in each case. Additionally, due to the time-varying frequency, the target has time-varying scattering characteristics for EM waves of different frequencies, which will impact the RCS of the target.

Table 2 presents the calculation time and speedup ratio (S_p) of the Parallel FDTD algorithm for different partitioning modes at different time-varying frequencies, when the time steps are all set to 40000 steps. As shown in Table 2, the calculation time of the parallel method varies for different partitioning methods, yet the program running speed is significantly improved.

Besides, as can be seen from the data in Table 2, the computation speed of a parallel approach is approximately seven times faster than that of a single process. However, as the number of parallel processes increases, the speed of parallel computing does not continue to increase; instead, it shows a relatively gradual decline as the number of processes increases. This is mainly because as the number of processes increases, the communication cost becomes higher. The number of grids

Table 2: The corresponding acceleration ratio of different parallel schemes under three time-varying frequencies

f_0 (MHz)	Process Number	Partitioning Mode	Parallel Time (s)	S_p
20	1	1×1×1	33763.2820	
	4	2×2×1	6078.145	5.555
	12	3×2×2	5679.412	5.945
	16	4×4×1	4968.570	6.795
	24	4×3×2	4680.543	7.214
	27	3×3×3	4814.949	7.012
	32	4×4×2	4931.247	6.847
	36	4×3×3	5327.295	6.338
40	1	1×1×1	34259.7538	∼
	4	2×2×1	7604.478	4.505
	12	3×2×2	6225.798	5.503
	16	4×4×1	5381.586	6.366
	24	4×3×2	5551.540	6.171
	27	3×3×3	5583.155	6.136
	32	4×4×2	5656.259	6.057
	36	4×3×3	6273.115	5.461
120	1	1×1×1	35509.1384	∼
	4	2×2×1	5975.918	5.942
	12	3×2×2	5213.722	6.811
	16	4×4×1	5359.718	6.625
	24	4×3×2	5384.410	6.595
	27	3×3×3	5585.403	6.357

needed to transfer data also increases, and the additional waiting time between the processes will continue to increase. This results in the parallel efficiency becoming lower and lower.

Figure 12 displays the monostatic RCS under various collision frequencies of plasma. As Fig. 12 indicates,

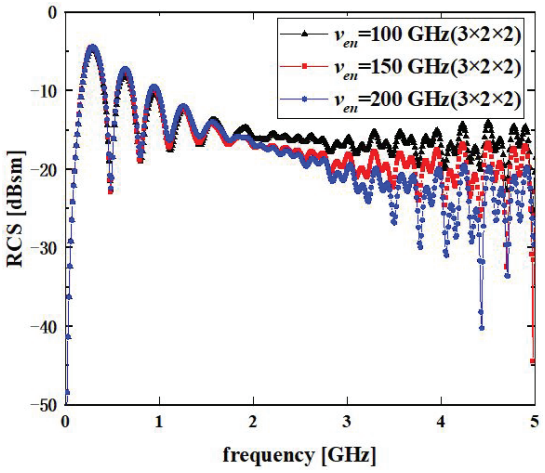

Fig. 12. Monostatic RCS of metal sphere coated with time-varying plasma with different collision frequencies v_{en}.

the monostatic RCS decreases with an increase in collision frequency. This is because, as the collision frequency increases, the absorption of EM waves by the plasma sheath is increased, which results in a decrease in the RCS.

Figure 13 shows the monostatic RCS under different thicknesses of plasma sheath. It can be seen that the monostatic RCS decreases with an increase in plasma thickness d. The explanation is that as the plasma thickness increases, the incident EM wave needs to traverse through a thicker layer of plasma. This results in more energy being absorbed or scattered away, and leads to a lower RCS of the target.

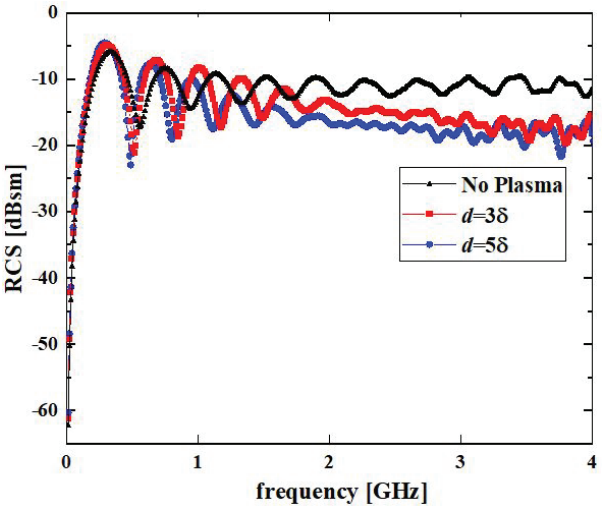

Fig. 13. Monostatic RCS of metal sphere coated with time-varying plasma with different thicknesses d.

IV. CONCLUSION

In this paper, the MPI-Based Parallel FDTD method and Lorentz transformation are integrated to calculate the EM scattering from a moving metal target coated with time-varying plasma. The accuracy and validity of the parallel Lorentz-FDTD algorithm is verified by comparing its results with those obtained using the serial approach. Moreover, the impacts of time-varying properties, plasma parameters, and motion velocity on the EM scattering properties of a moving and time-varying plasma coated target are investigated. The results reveal that the Parallel FDTD method can enhance the calculating speed and significantly reduce the calculation time when performing EM calculations regarding time-varying and moving dispersive medium targets. Furthermore, as the computational complexity increases, the computational efficiency of the Parallel FDTD algorithm will be further upgraded. Finally, by opting for the appropriate number of processes and an optimal partitioning mode, it is possible to further enhance the computational

efficiency and significantly abbreviate the computation time.

ACKNOWLEDGMENT

This work was supported by the National Natural Science Foundation of China (Nos. 62071003, 62201001, 61902252), the Natural Science Foundation of Education Department of Anhui Province, China (Grant No. KJ2020A0024), Anhui Provincial Natural Science Foundation (Nos.2208085QF184), the Open Research Fund of Advanced Laser Technology Laboratory of Anhui Province, China (No. AHL2020KF04), the Open Project of the State Key Laboratory of Millimeter Waves (Grant No. K202222).

REFERENCES

[1] W. Chen, "Research on some key problems of electromagnetic wave propagation and scattering in plasma sheath," Ph.D. dissertation, Dept. Radio Phys., Xidian Univ., Xian, China, 2018.

[2] L. Kuang, F. Xu, S. Z. Zhu, J. J. Gao, and Z. Q. Zheng, "Relativistic FDTD analysis of far-field scattering of a high-speed moving object," *IEEE Antennas Wireless Propag. Lett.*, vol. 14, pp. 879-882, Dec. 2014.

[3] G. Z. Niu, Y. M. Liu, B. W. Bai, and D. Yi, "A numerical simulation method of radar echo from a high-speed target," *IEEE Antennas Wireless Propag. Lett.*, vol. 20, no. 10, pp. 1958-1962, Oct. 2021.

[4] F. Harfoush, A. Taflove, and A. Kriegsmann, "A numerical technique for analyzing electromagnetic wave scattering from moving surfaces in one and two dimensions," *IEEE Trans. Antennas Propag*., vol. 37, no. 1, pp. 302-307, 1989.

[5] K. S. Zheng, Z. M. Mu, H. Luo, and G. Wei. "Electromagnetic properties from moving dielectric in high speed with Lorentz-FDTD," *IEEE Antennas Wireless Propag. Lett*., vol. 15, pp. 934-937, Sep. 2016.

[6] X. Q. Zhang and Z. P. Nie, "Simulation of electromagnetic scattering from moving perfectly conducting objects based on FDTD," *Chinese J. Radio Science*, vol. 24, no. 2, pp. 206-212, Apr. 2009.

[7] K.-S. Zheng, J.-Z. Li, G. Wei, and J.-D. Xu, "Analysis of Doppler effect of moving conducting surfaces with Lorentz-FDTD method," *J. Electron. Waves Appl.*, vol. 27, no. 2, pp. 149-159, Nov. 2012.

[8] K. S. Zheng, Y. Li, S. Qin, K. An, and G. Wei, "Analysis of micromotion characteristics from moving conical-shaped targets using the Lorentz-FDTD method," *IEEE Trans. Antennas Propag*., vol. 67, no. 11, pp. 7174-7179, Nov. 2019.

[9] D. B. Ge and Y. B. Yan, *The Finite-Difference Time-Domain Method for Electromagnetic Wave*, 3rd ed. Xi'an: Xidian Univ. Press, 2011.

[10] K. Yee, "Numerical solution of initial boundary value problems involving Maxwell's equations in isotropic media," *IEEE Trans. Antennas Propag*., vol. 14, no. 3, pp. 302-307, 1966.

[11] A. Taflove and S. Hagness, *Computational Electrodynamics: The Finite-Difference Time-Domain Method*, 2nd ed. Boston, MA: Artech House, 2000.

[12] R. C. Bollimuntha, M. F. Hadi, M. J. Piket-May, and A. Z. Elsherbeni, "Near-to-far field transformation in FDTD: A comparative study of different interpolation approaches," *Applied Computational Electromagnetics (ACES) Journal*, vol. 36, no. 05, pp. 496-504, 2021.

[13] V. Varadaraian and R. Mittra, "Finite-difference time-domain (FDTD) analysis using distributed computing," *IEEE Microw. Guided Wave Lett*., vol. 4, no. 5, pp. 144-145, 1994.

[14] C. Guiffaut and K. Mahdjoubi, "A Parallel FDTD algorithm using the MPI library," *IEEE Antennas Propag. Mag*., vol. 43, no. 3, pp. 94-103, 2001.

[15] T. Stefanski and T. D. Drysdale, "Parallel implementation of the ADI-FDTD method," *Micro. Optical Techno. Lett*., vol. 51, no. 5, pp. 1298-1304, 2009.

[16] X. Duan, X. Chen, K. Huang, and H. Zhou, "A high performance Parallel FDTD based on Winsock and multi-threading on a PC-Cluster," *Applied Computational Electromagnetics (ACES) Journal*, vol. 26, no. 3, pp. 241-249, 2022.

[17] Y.-F. Mao, J.-H. Chen, L. Pan, and X.-M. Wang, "Implementation of two different moving window FDTD methods to simulate the electromagnetic propagation in tunnel with parallel computing," *Applied Computational Electromagnetics (ACES) Journal*, vol. 30, no. 04, pp. 428-435, 2021.

[18] J. Chakarothai, K. Wake, and S. Watanabe, "Scalable GPU-parallelized FDTD method for analysis of large-scale electromagnetic dosimetry problems," *Applied Computational Electromagnetics (ACES) Journal*, vol. 31, no. 06, pp. 661-668, 2021.

[19] J. Z. Lei, C. H. Liang, W. Ding, and Y. Z, "Study on MPI-based parallel modified conformal FDTD for 3-D electrically large coated targets by using effective parameters," *IEEE Antennas Wireless Propag. Lett*., vol. 7, pp. 175-178, Sep. 2008.

[20] D.-B. Ge and L.-X Yang, "FDTD applied to anisotropic medium and its parallel computing," *J. System Engineering Electron*., vol. 28, no. 4, pp. 483-485, Apr. 2006.

[21] L.-X. Yang, D.-B. Ge, K. S. Zheng, and B. Wei, "Study of Parallel FDTD algorithm for anisotropic medium on a PC cluster system," *Chinese J. Radio Science*, vol. 21, no. 1, pp. 43-48, Feb. 2006.

[22] L.-X Yang, D.-B. Ge, B. Wei, K. S. Zheng, and N. Ge, "A study of FDTD parallel algorithm for anisotropic media with dyadic permittivity and permeability," *Acta Electron. Sinica*, vol. 34, no. 9, pp. 1703-1707, Sep. 2006.

[23] X. L. Duan, H. W. Yang, Y. Liu, and L. An, "Auxiliary Differential Equation FDTD method of plasma in parallel environment," *J. Infrared Milli., Terahz Waves*, vol. 30, pp. 860-867, 2009.

[24] J. Wang, W. Y. Yin, and Y. S. Xia, "A novel conformal surface current technique for large problems based on high-performance Parallel FDTD method," *IEEE Antennas Wireless Propag. Lett*., vol. 12, pp. 11-14, 2013.

[25] Q. W. Shi, B. Zhou, L. M. Zhang, and D. S. Liu, "Hybrid Parallel FDTD calculation method based on MPI for electrically large objects," *Wireless Commun. Mob. Comput*., 2019.

[26] L. Man, Y. Bo, H. C. Deng, Z. H. Xiao, and L. X. Yang, "Study on the interaction between relative moving plasma plate and electromagnetic wave," *Chinese J. Radio Science*., pp. 1-9, May 2022.

[27] B. Wei, D.-B. Ge, and F. Wang, "A general method for finite difference time domain modeling of wave propagation in frequency-dispersive media," *Acta Phys. Sinica*, vol. 57, no. 10, Oct. 2008.

Hai-Yan Li was born in Huaibei City, Anhui Province, China, in 1999. She received the B.S. degree in electronic information engineering from Huainan Normal University, Huainan, China, in 2021. She is currently working toward the master's degree in electromagnetic field and microwave technology of Electronic Information with the School of Electronic Information Engineering, Anhui University, Hefei, China.

Her current research interest is computational electromagnetism.

Xian-Min Guo was born in Xianyang City, Shanxi Province, China, in 1999. She received the B.S. degree in electronic information engineering from Shandong University of Technology, Zibo, China, in 2021. She is currently working toward the master's degree in electromagnetic field and microwave technology of Electronic Information with the School of Electronic Information Engineering, Anhui University, Hefei, China.

Her current research interest is computational electromagnetism and plasma physics.

Yong Bo was born in Shandong Province, China, on November 11, 1989. He received the B.S. degree in Shandong University of Science and Technology, Qingdao, China, in 2012, and the Ph.D. degree from the Center for Information Geoscience, University of Electronic Science and Technology of China, Chengdu, China.

He is currently a Lecturer with the University of Anhui, Hefei, China. The main subjects of his interest include computational electromagnetic, wave propagation in plasmas, and low temperature plasma technology and application.

Wei Chen was born in Jiangsu Province, China, in 1987. He received the B.S. and M.S. degrees from Jiangsu University, Jiangsu, China, in 2010 and 2013, respectively, and the Ph.D. degree from Xidian University, Xi'an, China, in 2018.

He is currently a Lecturer with the School of Electronics and Information Engineering, Anhui University, Hefei, China. His current research interests include numerical methods in electromagnetic scattering from plasma and wave propagation in complex systems.

Li-Xia Yang was born in Ezhou, Hubei, China, in 1975. He received the B.S. degree in physics from Hubei University, Wuhan, China, in 1997, and the Ph.D. degree in radio physics from Xidian University, Xi'an, China, in 2007.

Since 2010, he has been an Associate Professor with the Communication Engineering Department, Jiangsu University, Zhenjiang, China. From 2010 to 2011, he was a Postdoctoral Research Fellow with the Electro Science Laboratory (ESL), The Ohio State University, Columbus, OH, USA. From 2015 to 2016, he was a Visiting Scholar with the Institute of Space Science, The University of Texas at Dallas, Dallas, TX, USA. From 2016 to 2019, he has been a Professor, a Ph.D. Supervisor, and the Chairman of the Communication Engineering Department, Jiangsu University. Since 2020, he has been a Distinguished Professor, a Ph.D. Supervisor, and the Vice Dean with the School of Electronic and Information Engineering, Anhui University, Hefei, China. His research interests include wireless communication technique, radio sciences, the computational electromagnetic, and the antenna theory and design in wireless communication systems. He is a member of the Editor Board of Radio Science Journal in China.

Zhi-Xiang Huang was born in Anhui, China, in 1979. He received the B.S. and Ph.D. degrees from Anhui University, Hefei, China, in 2002 and 2007, respectively. He was a Visiting Scholar with Iowa State University, USA, from September 2010 to September 2011. From August 2013 to October 2013, he was a Visiting Professor with The University of Hong Kong. From February 2014 to February 2015, he was a Visiting Professor with the Beijing National Laboratory for Condensed Matter Physics, Institute of Physics, Chinese Academy of Sciences. He has published one monograph on the symplectic finite-difference time-domain method and two book chapters at CRC Press and In Tech Publishers. He has published 60 peer-reviewed journal articles included in the Web of Science Core Collection. His current research interests include time-domain numerical methods, metamaterials, and active metamaterials. He is a member of the OSA. In 2015, he was awarded the Second Prize of Science and Technology from the Anhui Province Government, China, and the National Science Foundation for Outstanding Young Scholar of China, in 2017.

Jia-Chen Wang was born in Hefei City, Anhui Province, China, in 2003. He is currently working toward the B.S. degree in communication engineering with the School of Electronic Information Engineering, Anhui University, Hefei, China.

His current research interest is microwave radar.

Xin-Jie Duan was born in Luan City, Anhui Province, China, on April 23rd, 2005. She is currently an undergraduate student majoring in Communication Engineering at the School of Electronic Information Engineering, Anhui University, Hefei, China. She was awarded the annual study scholarship.

Her current research interest is computational electromagnetism.

Mie Scattering Properties of Simple RCS Objects and Applications

Ilkyu Kim[1], Sun-Gyu Lee[2], and Jeong-Hae Lee[3]

[1]Department of Electrical and Electronics Engineering
Sejong Cyber University, Seoul 05006, South Korea
Ikkim0704@sjcu.ac.kr

[2]Radio Environment Monitoring Laboratory
Electronics and Telecommunications Research Institute, Daejeon 34129, Republic of Korea
gyul0206@etri.re.kr

[3]Department of Electronic and Electrical Engineering
Hongik University, Seoul 04066, Republic of Korea
jeonglee@hongik.ac.rk

Abstract – The requirement for advanced target recognition has facilitated the evolution of radar systems, enabling classification, recognition and identification of various types of objects. Numerous studies have focused on the accurate prediction of radar cross-section (RCS) for target identification. While the magnitude of the Mie scattering has been widely employed to enhance the likelihood for target detection, the proposed method based on the frequency spectrum of Mie scattering was presented for estimation of the size of the target. An accurate size of targets was quickly estimated using the frequency of the peak Mie scattering. The frequencies of Mie scattering are investigated using different radiuses of spheres and cylinders which directly indicate the size of objects. The peak magnitudes were acquired at 105∼485 MHz and 83∼398 MHz for spheres and cylinders, respectively, as the radiuses change from 0.1 m to 0.5 m. In addition, two aircraft-shaped models consisting of an ellipsoidal body, two wings and a stabilizer are used to obtain RCS scattering with various azimuth and elevation angles. Indoor RCS measurements with a metal sphere are presented in order to validate its effectiveness.

Index Terms – Aircraft-shaped objects, Mie scattering, radar cross-section (RCS), target identification.

I. INTRODUCTION

Radar systems have been widely used for the classification, recognition and identification of various types of objects [1–2]. A number of methods have been investigated for accurately predicting a radar cross-section (RCS) for the purpose of target identification [3–5]. The process of target identification commonly requires analyzing electromagnetic waves reflected back from targets. Several techniques have been applied to the analysis of RCS targets in which a simplified RCS object was used. Physical optics and geometrical optics methods have been applied to the analysis of simplified electromagnetic models for tanks [6], ships [7], aircraft [8] and missiles [9]. Statistical models based on the collected data set have been used in target identification and several algorithms have been investigated in order to implement effective target classifiers [10–12]. Radio frequency (RF) imaging has techniques for recognizing the details of unmanned aerial vehicles (UAV) with wings, payloads and body types [13]. However, this method typically demands intensive post-processing for the creation of target images. For time-limited operations, a simpler procedure requiring only RCS is more desirable. RCS scattering in the resonance (Mie) region has been used in target detection and classification algorithm in the time domain [14–16]. With a readily attainable frequency point of the highest RCS in the frequency domain, an accurate and more efficient target classification method may be achieved.

In this paper, a simple technique based on the unique signature of RCS scattering is proposed for the size estimation of targets. A workflow of this article is presented in Fig. 1. Compared to the conventional method, which has utilized the amplitude of the echo signal, more accurate estimation of target size can be realized using both magnitude and frequency of peak Mie scattering. The size of the target is instantly obtained by measuring the frequency where the peaks of RCS scattering are made. The frequencies of Mie scattering are investigated using different radiuses of spheres and cylinders, and aircraft-shaped model with various azimuth and elevation angles.

Submitted On: March 14, 2024
Accepted On: December 4, 2024

https://doi.org/10.13052/2025.ACES.J.400205

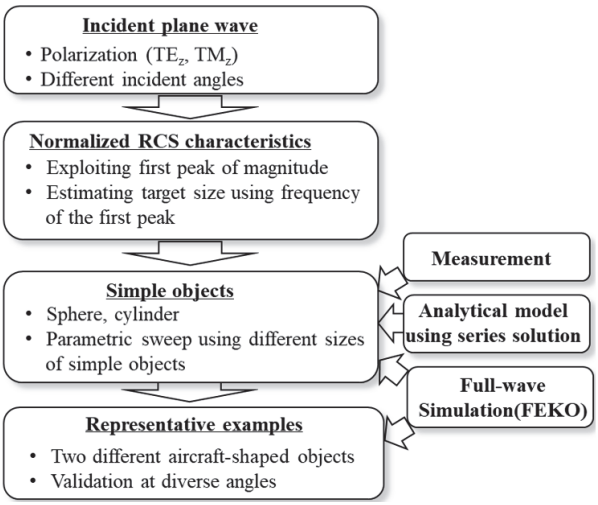

Fig. 1. Workflow of this article: proposed method based on the frequency point of normalized RCS scattering.

Indoor RCS measurements with the metal sphere validate the results obtained from the simulations.

II. TARGET RECOGNITION PRINCIPLE

The purpose of this section is to present the target estimation principles based on the distinct features of RCS scattering produced by the different sizes and shapes of objects. While estimation of the target size usually revolves around the magnitude of the echo signal, RCS scattering in the frequency domain [17] is introduced to enhance accuracy in this work. The frequency point where the first peak magnitude of RCS scattering appears is applied to the precise estimation of the target size. The proposed method was validated with RCS scattering of a metal sphere and cylinder, which were used as a simplified aircraft model, and the plane-wave incidence on the objects was assumed. Firstly, RCS scattering is investigated using the sphere and cylinder which were normalized with their cross-sections. Two spheres with radiuses of 25 mm and 15.9 mm were used for the evaluation in accordance with the setup of the indoor measurement presented in the subsequent sections. RCS scattering properties were obtained using the full-wave simulation FEKO and the analytical model based on series solution presented in [18]. The validity of the simulated results is evaluated with the calculated one. Figure 2 shows the magnitude of RCS normalized with the cross-section of the sphere and cylinder. Figure 2 (a) shows RCS characteristics in the Rayleigh and Mie regime. In the Mie regime, it tends to oscillate and converge to one for the optical regime [19].

For the sphere with radiuses R = 25 mm and 15.9 mm, the peaks of the normalized RCS occurred at 2 GHz and 3 GHz, respectively. For the cylinder, an incident

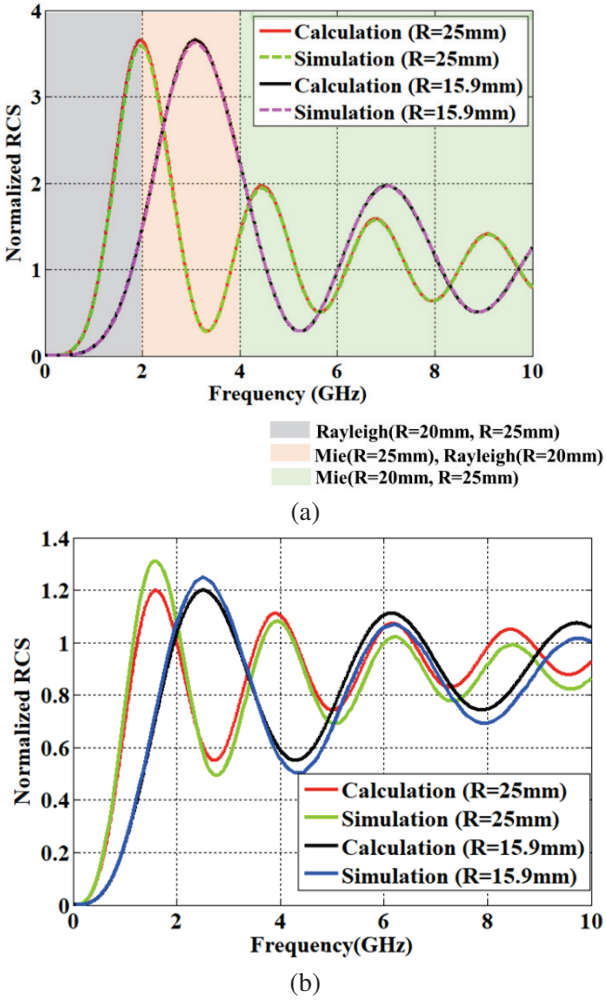

Fig. 2. Monostatic RCS normalized with its cross-section for (a) the case of the sphere and (b) the case of the cylinder.

wave with TE$_z$ polarization was used since it was more suitable for obtaining peak RCS value for target identification. Frequency points for the cylinder with radiuses of R = 25 mm and 15.9 mm were 1.6 GHz and 2.5 GHz, respectively, which were roughly 20% lower than both cases of the sphere, due to the larger RCS of the cylinder. For both cases, excellent agreement between the simulated and calculated results was observed. While the frequency points can be instantly obtained using the proposed method, the computational time of two spheres using FEKO was 3.9-5.3 hours per one case of simulations. Figure 3 shows frequencies of peak RCS calculated using the analytical model of the series solution with different radiuses of the sphere model and the cylinder model. It can be found that frequency of peak RCS decreases with increased radius of the sphere model and the cylinder model.

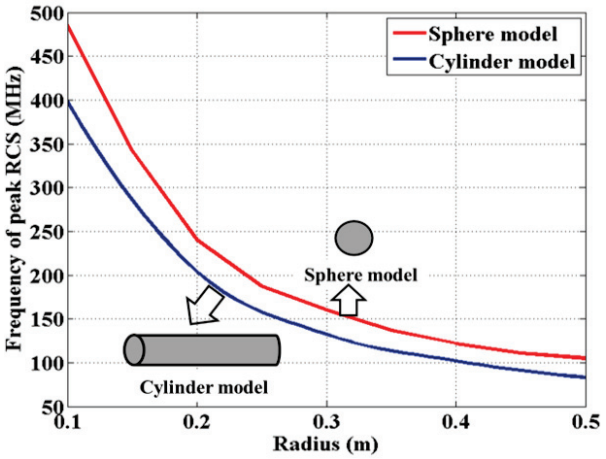

Fig. 3. Frequencies of peak RCS calculated using the analytical model for different radiuses of the sphere model and the cylinder model.

Peak magnitudes were acquired at 105∼485 MHz for sphere and 83∼398 MHz for cylinder. The frequencies of the sphere model are slightly higher than the cylinder model. Note, the frequencies of the cylinder model depend on the radius regardless of length of the cylinder.

III. APPLICATIONS OF THE PROPOSED METHOD

One of the main purposes of this paper was to evaluate the applicability of the proposed method using an aircraft-shaped model. The main body of the aircraft model was modeled as an ellipsoidal shape to represent a large airplane (Target A) and a small airplane (Target B). The length and radius of the ellipsoidal shape is 4 m and 0.5 m for target A, and 1 m and 0.1 m for target B, respectively. The aircraft model includes the wing, the tail and the stabilizer. The target inside the 3D spherical coordinate system is shown in Fig. 4. In order to evaluate the proposed method based on the aircraft model, a comparative analysis between sphere and cylinder model and the aircraft model is presented.

The dimensions of the sphere and cylinder are set to correspond to those of target A and target B, respectively. Note that a vertically polarized incident wave is used due to its effectiveness in target classification. Figure 5 shows a comparison of the normalized RCS between the simple geometries and the aircraft-shaped model. Despite the difference in graph shapes, the frequencies of the peak points exhibit a remarkable similarity, deviating by less than 5% in terms of center frequencies. Using the two aircraft models, diverse line of sight scenarios were evaluated. Typical line of sight scenarios with elevation angle θ of 95°∼110° and azimuth angle ϕ of 30°∼60° were

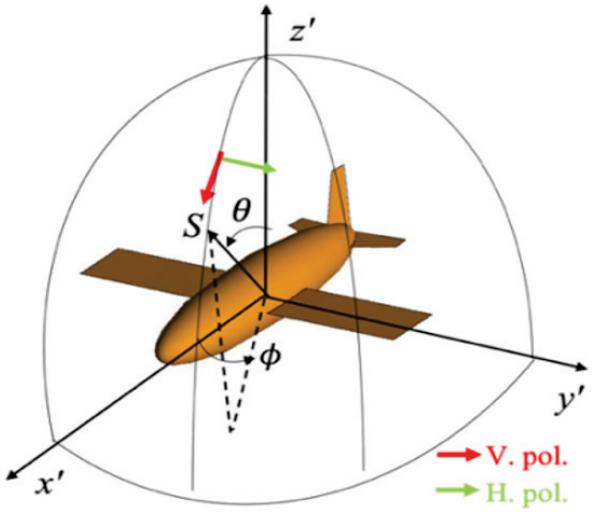

Fig. 4. RCS scattering of the aircraft-shaped FEKO model: target inside a 3D spherical coordinate system.

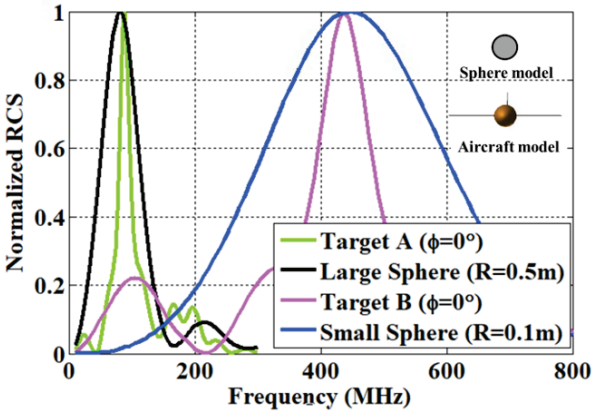

(a)

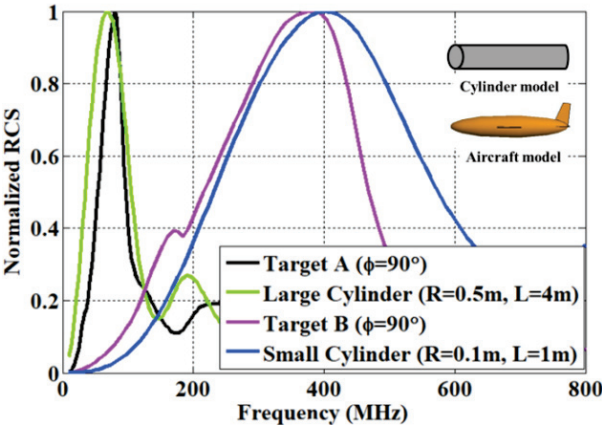

(b)

Fig. 5. RCS scattering of the aircraft-shaped FEKO model: (a) target inside 3D spherical coordinate system and (b) scenarios of target detection.

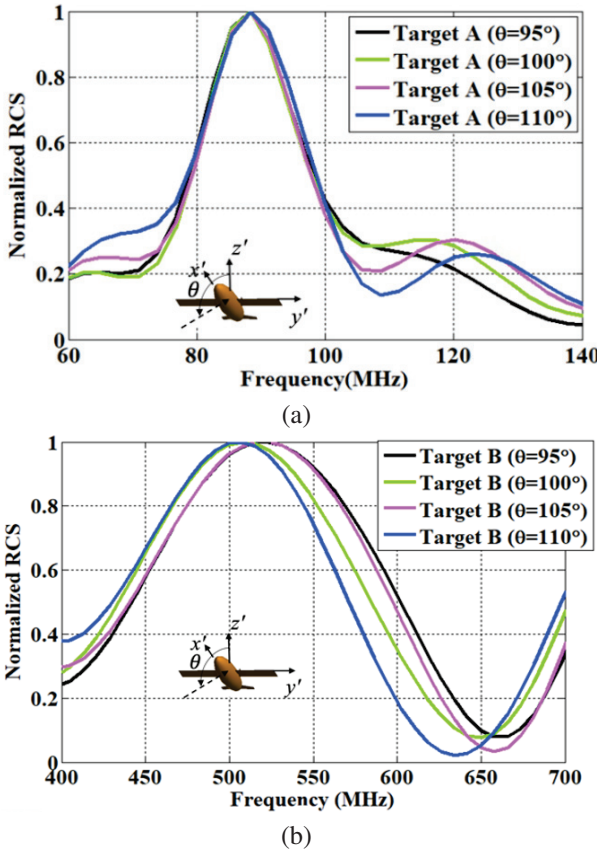

Fig. 6. Normalized RCS in the frequency domain for (a) target A (large aircraft) and (b) target B (small aircraft) with elevation angles of $\theta = 0°, 45°$ and $90°$.

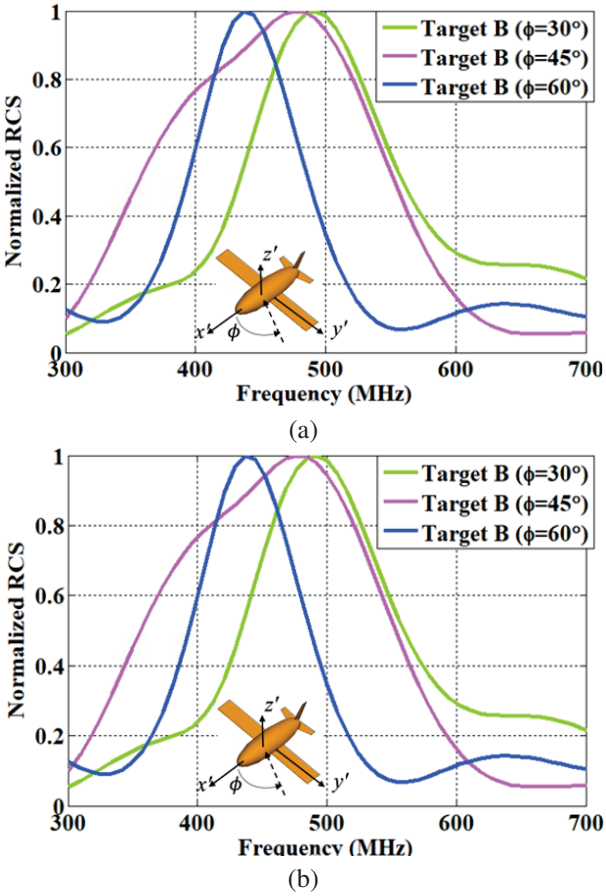

Fig. 7. Normalized RCS in the frequency domain for (a) target A (large aircraft) and (b) target B (small aircraft) with azimuth angles of $\phi = 0°, 45°$ and $90°$.

considered. Figure 6 shows the normalized RCS with respect to the elevation angle θ obtained from full-wave simulation FEKO. The frequencies of the highest value of the normalized RCS are approximately 90 MHz for target A and 510 MHz for target B. Deviation of the frequencies according to the elevation angles is less than 3 MHz for target A and 25 MHz for target B. There is a relatively small frequency variation in terms of the elevation angle θ. Figure 7 shows the normalized RCS of line-of-sight detection with the azimuth angle ϕ at the elevation angle θ=100°.

The circumference of the ellipsoidal model and the area of the two wings were changed for the different azimuth angle, which resulted in different frequencies. The peak RCS values were obtained at 85∼94 MHz for target A and 436∼492 MHz for target B. The observed frequency points, which are influenced by the incident angles, exhibit a variation of less than 15%, thereby providing significant utility in discriminating between various target types. It is shown that the method provides the successful classification of the two aircrafts. In Fig. 8, 3D plots of the frequencies of the highest RCS values are presented. It is observed that there is a slight increase of all frequencies at the azimuth angle $\phi = 30°$. Although in the 3D plot a variation increases slightly, it can be found that two groups of frequencies for both large and small aircrafts can be achieved. This work studies modified shapes of the aircraft model to validate its effectiveness. Figure 9 presents the frequencies of the peak RCS for ellipsoidal object with different radiuses based on the target A. The similar frequencies of the peak RCS can be obtained when r_b/r_a is smaller than 2.0. It is also shown that the frequencies of the peak RCS are not severely affected by the modified shapes of the aircraft model.

Next, the procedure to estimate the size of targets using the frequency of first peak RCS is presented. The first peak of the normalized RCS can be found to obtain its frequency point:

$$\sigma(f_i) > \sigma(f_j), \quad j = 1, 2, \ldots, N, \quad j \neq i, \qquad (1)$$

where $\sigma(f_i)$and $\sigma(f_j)$are the normalized RCS at frequency point f_i and f_j, respectively. The frequency

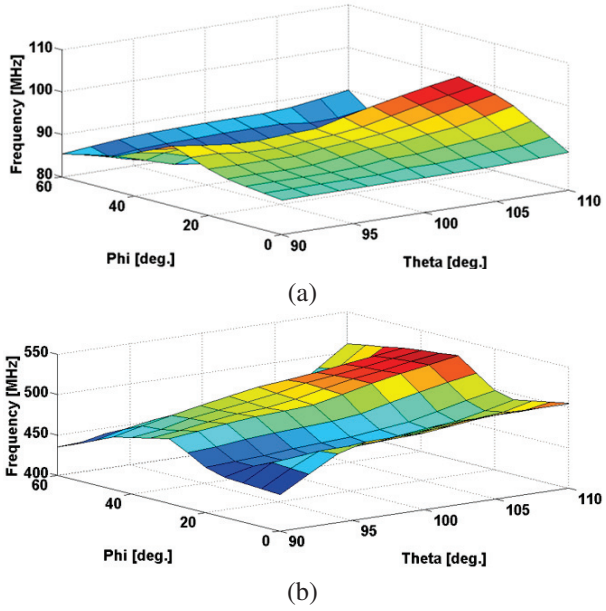

Fig. 8. 3D plots of the frequencies of the highest RCS values for (a) target A (large aircraft) and (b) target B (small aircraft) with different azimuth and elevation angles.

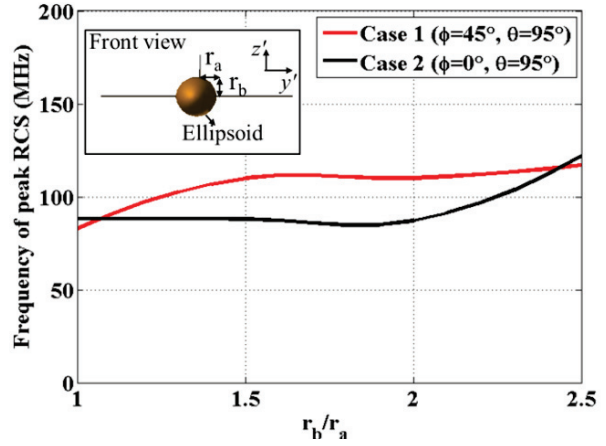

Fig. 9. Frequencies of peak RCS with different radius ratio of the ellipsoidal object.

point f_i where the peak of the normalized RCS occurs can be obtained. Next step is to compare the frequency point to the one in the database using the target classification technique presented in [15]. The distance between two frequency points can be defined as:

$$d_{a,\,b} = \sqrt{(f_a - f_b)^2}\,, \tag{2}$$

where f_a and f_b are the frequencies of target a and b, respectively. Thus, an unidentified target with a frequency f_t can be classified as a specific target u listed in

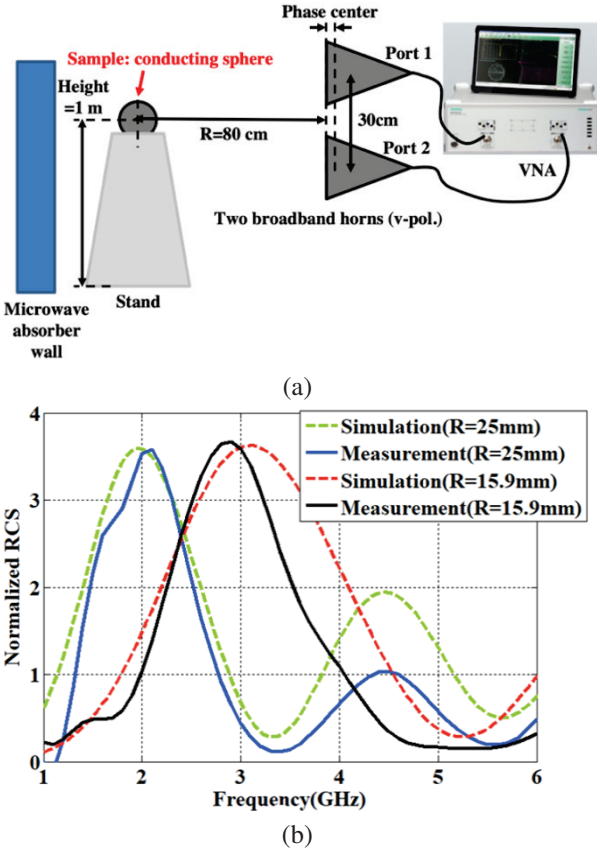

Fig. 10. Evaluation using indoor measurements: (a) depiction of the indoor measurement setup and (b) comparison between simulated and measured results for the two different radiuses of the metal spheres.

the database under the following condition:

$$d_{t,\,u} < d_{t,\,v},\quad v = 1,\,2,\,\ldots,\,M,\quad u \neq v, \tag{3}$$

where M is the number of data points.

IV. MEASUREMENT OF RCS OF A METAL SPHERE

In order to evaluate the numerical approach, indoor measurement of a metal sphere is performed. To experimentally verify the relationship between target size and RCS in the frequency domain, a scattered signal is generated by the sample. Therefore, a careful measurement setup was required to enhance the signal originating from the sample while minimizing external interference signals. The sample was located at 1 m elevation using a Styrofoam stand to prevent interference by scattered waves from the indoor floor.

Microwave absorber walls were placed around the sample to minimize interference by scattered waves from the indoor wall. Two broadband horn antennas operating in the frequency range of 1-6 GHz were used to generate an incident wave of vertical polarization (v-pol).

Separation distance between the sample and the two horns was the most important factor in determining the strength of the scattered signal from the sample. Since the previous study [20] suggested that the horn antenna had little gain reduction when the distance to the target normalized by the far-field distance was greater than 2, the separation distance was set to 80 cm. Finally, RCS can be calculated from the measured S21 in a vector network analyzer (VNA). A time-gating function [21] was used to separate the scattered signal by the sample from the noises, such as thermal noise and near-field coupling between two horns. Figure 10 (b) shows the measured RCS of the conducting spheres. The trend of measured results agrees well with the calculation and simulation results. The discrepancy in the second peak value was mainly due to a slight axis misalignment and a time-gating error. It was experimentally verified that target size could be distinguished from RCS shape in the frequency domain.

V. CONCLUSION

The proposed method based on the frequency spectrum of the scattering characteristics was presented for estimation of the size of the target. Target size was estimated using the distinctive features of RCS scattering in the Mie region. The principle of estimating the size of the target was presented for a simple aircraft model consisting of a metal sphere and cylinder which simply represents the front and side of an aircraft. The ellipsoidal aircraft model with the wing, the tail and the stabilizer was evaluated in terms of different aircraft sizes, and its azimuth and elevation angles. The peak magnitudes were acquired at 85∼94 MHz for target A and 436∼492 MHz for target B. Peak RCS values at different frequencies imply the sizes comparable to small and large aircraft. The frequency points according to the azimuth and elevation angles shows a relatively small deviation providing significant utility in discriminating various targets.

ACKNOWLEDGMENT

J.-H. Lee and I. K. Kim were funded by the National Research Foundation of Korea (NRF) grant funded by the Korea government (MSIT) (RS-2024-00343372).

REFERENCES

[1] I. Guvenc, F. Koohifar, S. Singh, M. L. Sichitiu, and D. Matolak, “Detection, tracking, and interdiction for amateur drones,” *IEEE Comm. Magazine*, vol. 56, no. 4, pp. 75-81, Apr. 2018.

[2] I. Kim, H. Kim, and J.-H. Lee, “Theoretical minimum detection range for a rapidly moving target and experimental evaluation,” *J. Electromagn. Eng. Sci.*, vol. 21, no. 2, pp. 161-164, Apr. 2021.

[3] A. Boag, “A fast iterative physical optics (FIPO) algorithm based on non-uniform polar grid interpolation,” *Microw. Opt. Technol. Lett.*, vol. 35, no. 3, pp. 240-244, Nov. 2002.

[4] M. A. Shah, B. A. Salau, and Ç. Tokgöz, “Bistatic radar cross section prediction using iterative physical optics with physical theory of diffraction for plate geometries,” in *2020 IEEE Int. Symp. on Antennas and Propag. and North American Radio Sci. Meeting*, Feb. 2020.

[5] M. A. Shah, B. A. Salau, and Ç. Tokgöz, “Radar cross section prediction using iterative physical optics with physical theory of diffraction,” *IEEE Trans. Antennas Propag.*, vol. 70, no. 6, pp. 4683-4690, June 2022.

[6] R. J. Burkholder, Ç. Tokgöz, C. J. Reddy, and W. O. Coburn, “Iterative physical optics for radar scattering predictions,” *Appl. Comput. Electromagn. Soc. J.*, vol. 24, no. 2, pp. 241-258, June 2009.

[7] E. Gillion, E. Rochefort, J. Claverie, and C. Brousseau, “Improvement of RCS estimation of large targets by using near-field approach,” in *IEEE Radar Conf*, Ottawa, Canada. p. 1, Apr. 2013.

[8] W. D. Burnside, R. C. Rudduck, and R. J. Marhefka, “Summary of GTD computer codes developed at the Ohio State University,” *IEEE Trans. Electromagn. Compat.*, vol. EMC-22, no. 4, pp. 238-243, Feb. 1980.

[9] G. S. B. Rao, S. Nambari, S. Kota, and K. S. R. Rao, “Monostatic radar cross section estimation of missile shaped object using physical optics method,” *2017 IOP Conf. Ser.: Mater. Sci. Eng.*, p. 225, 2017.

[10] F. Obelleiro-Basterio, J. L. Rodriguez, and R. J. Burkholder, “An iterative physical optics approach for analyzing the electromagnetic scattering by large open-ended cavities,” *IEEE Trans. Antennas Propag.*, vol. 43, no. 4, pp. 356-361, Apr. 1995.

[11] M. Ezuma, C. K. Anjinappa, M. Funderburk, and I. Guvenc, “Radar cross section based statistical recognition of UAVs at microwave frequencies,” *IEEE Trans. on Aerospace and Electronic Systems*, vol. 58, no. 1, pp. 27-46, Feb. 2022.

[12] S. Lee, S.-J. Jeong, B.-S. Kang, H. Kim, S.-M. Chon, and H.-G. Na, “Classification of shell-shaped targets using RCS and fuzzy classifier,” *IEEE Trans. Antennas Propag.*, vol. 64, no. 4, pp. 1434-1443, Apr. 2016.

[13] C. J. Li and H. Ling, “An investigation on the radar signatures of small consumer drones,” *IEEE Antennas and Wireless Propag. Letts.*, vol. 64, no. 4, pp. 649-652, Apr. 2016.

[14] Y.-R. Jeong, C.-S. Park, Y.-K. Ko, and J.-G. Yook, ”Analysis of RCS of low observable aircraft in VHF band,” *Int. J. of Antennas Propag.*, vol. 2018, p. 10, 2018.

[15] J. S. Chen and E. K. Walton, "Comparison of two target classification techniques," *IEEE Trans. Aerospace and Electronic Systems*, vol. AES-22, no. 1, pp. 15-22, Jan. 1986.
[16] D. Moffatt and R. Mains, "Detection and discrimination of radar targets," *IEEE Trans. Antennas Propag*., vol. 23, no. 3, pp. 358-367, May 1975.
[17] T. Mizushima, R. Nakamura, and H. Hadama, "Reflection characteristics of ultra-wideband radar echoes from various drones in flight," *2020 IEEE Topical Conf. Wireless Sensors Sens. Netw. (WiSNeT)*, pp. 30-33, 2020.
[18] C. A. Balanis, *Advanced Engineering Electromagnetics*, 2nd ed. New Jersey: Wiley, 2012.
[19] I. Kim, S. Xu, and Y. Rahmat-Samii, "Generalised correction to the Friis Formula: Quick determination of the coupling in the Fresnel region," *IET Microw. Antennas Propag.*, vol. 7, no. 13, pp. 1092-1101, Oct. 2013.
[20] C. Uluisik, G. Cakir, M. Cakir, and L. Sevgi, "Radar cross section (RCS) modeling and simulation, part 1: A tutorial review of definitions, strategies, and canonical examples," *IEEE Antennas and Propag. Magazine*, vol. 50, no. 1, pp. 115-126, Feb. 2008.
[21] A. Henderson, J. R. James, P. Newham, and G. Morris, "Analysis of gating errors in time domain antenna measurements," *IEE Proceedings H (Microw. and Antennas and Propag.)*, vol. 136, no. 4, pp. 311-320, Aug. 1989.

Ilkyu Kim received his B.S. degree in Electronics and Electrical Engineering from Hongik University, Seoul, South Korea, in 2003, the M.S. degree in Electrical Engineering from University of Southern California, Los Angeles, CA, in 2006, and Ph.D. degree in Electrical Engineering from University of California at Los Angeles in 2012. He was with Samsung Advanced Institute of Technology from 2006 to 2008. After gaining his Ph.D. degree, he joined the Defense Agency for Technology Quality, Daejeon, South Korea, where his research area was studying radar and space applications. Since 2022, he has been an assistant professor with the Department of Electrical and Electronics Engineering, Sejong Cyber University, Seoul, South Korea. His research interests include but are not limited to computation of electromagnetic mutual coupling and antenna design for space and radar applications.

Sun-Gyu Lee received the B.S., M.S. and Ph.D. degrees in electronic and electrical engineering from Hongik University, Seoul, South Korea, in 2016, 2018 and 2023, respectively. He was a Research Professor of the Metamaterial Electronic Device Research Center, Hongik University, Seoul, South Korea, in 2023. Since 2024, he has been working as a Senior Researcher with the Electronics and Telecommunications Research Institute, Daejeon, South Korea. His current research interests include reconfigurable metasurfaces, reconfigurable intelligent surfaces and phased array antennas.

Jeong-Hae Lee received the B.S. and M.S. degrees in electrical engineering from Seoul National University, South Korea, in 1985 and 1988, respectively, and the Ph.D. degree in electrical engineering from the University of California at Los Angeles, Los Angeles, CA, USA, in 1996. From 1993 to 1996, he was a Visiting Scientist of general atomics in San Diego, CA, USA, where his major research initiatives were developing a millimeter-wave diagnostic system and studying plasma wave propagation. Since 1996, he has been a Professor with the Department of Electronic and Electrical Engineering, Hongik University, Seoul, South Korea. He was President of the Korea Institute of Electromagnetic Engineering and Science in 2019. He is currently Director of the Metamaterial Electronic Device Center. He has more than 130 articles published in journals and 80 patents. His current research interests include metamaterial radio frequency devices and wireless power transfer.

Design of 4×4 Multi-layer Butler-like Matrix with Flexible Phase Differences and Filtering Integration for 5G Applications

Li Ma, Lei Wang, and Xiaodong Chen

Department of Mobile Communications and Terminal Research
China Telecom Research Institute, Guangzhou, 510000, China
mal1@chinatelecom.cn, wanglei1@chinatelecom.cn, chenxiaodong@chinatelecom.cn

***Abstract* –** A universal topology for the filtering integrated Butler-like matrix (BLM) with flexible beam steering has been proposed based on the $N/2 \times N$ Butler matrix (BM). This structure is constructed on three-layer circuits, with compact size and no crossover owing to the path distribution. Besides, the filtering function has been integrated into the BLM by utilizing the multi-stage coupled lines. For validation, a 4×4 BLM operating at 4.9 GHz was designed and fabricated. Measured results reveal that the 4×4 BLM exhibits a working bandwidth of 18.4% and filtering integrated functions, with a compact size of $1.2\times2.3\ \lambda_g^2$. The measured scatting parameters and phase characteristics show great agreement with the simulated ones.

***Index Terms* –** Antenna array, Butler matrix, filtering, multi-layer circuit, flexible phase differences.

I. INTRODUCTION

The development of wireless communication and growing demands for high-speed data services has raised higher requirements for the coverage and capability for the 5G signals and terminals [1]. Flexible BPNs are an ideal solution to extend the radiation range of antenna arrays (AA) in practical engineering. The implementation of smart antennas in the existing wireless communication depends a lot on the flexible BPNs. Among them, Butler matrix (BM) is the most widely used. For a conventional 4×4 BM with the distance between adjacent radiation elements being half a wavelength, the beam direction is fixed at ±48.6° and ±14.5° respectively [2–5]. However, in realistic employment, BMs with arbitrary phase differences (A-PD) are desired for flexible beam coverage of the smart antenna arrays. High-order BM is one of the approaches of exploring the beam's controllability so as to broaden the radiation angle. In other ways, standard BM could be integrated with switching networks [6], or A-PD elements [7] to realize flexible phase differences.

BMs with various circuit structure and multiple function integration have been studied in various ways, such as multilayered printed circuit board (PCB) construction [8], CMOS technologies [9] and so on. In [10], a low-loss PET-based 4×4 BM has been designed with fixed phase differences of ±45° and ±135°. Additionally, BM now has a filtering option, which simplifies the system, improves the performance, and reduces the complexity. Nevertheless, research on integrated filter antennas that are excited by nearby input ports and have variable beam spacing and arbitrary beam direction is still required.

In this paper, a multilayer configuration of the BM has been presented with theorical analysis, design procedure, and experimental verification. The generalized coupling network (GCN) consisting of power dividers, phase shifting units, and shunt single-pole-double-throw (SPDT) switches, has been introduced to construct the Butler-like matrix (BLM). This paper is an expansion of the authors' previous work in [11]. Advantages of this BM lies in three aspects: 1) an original circuit configuration with compact size and no crossover, 2) flexible phase differences for the beam steering and beam controllability, and 3) wideband and filtering functions integrated for practical applications. Compared with the author's former work [11] and the related A-PD antenna arrays in [10] and [2–13], our improvements and contributions are as follows. The universal topology of the BLM with flexible phase differences has been designed and explained, with the design theory under two different working states illustrated in detail. The relationship between the beam-steering properties of the proposed topology with the phase differences of the BLM and the parameters of components are delivered and analyzed, which are also compared with the conventional ones to highlight the advantages of this BLM structure. Furthermore, the design procedure of the beam has been explored from 4×4 to $N\times N$ beamforming networks. Moreover, for validation, the 4×4 BLM has been designed, fabricated, and measured. Both simulated and measured results coincide well with each other. Measured results reveal that the 4×4 BLM exhibits a wide working bandwidth and compact size

Submitted On: January 8, 2024
Accepted On: March 11, 2024

https://doi.org/10.13052/2025.ACES.J.400206

with filtering integrated functions and flexible phase properties.

II. DESIGN THEORY OF BLM

The topology and configuration of the BLM is illustrated in this section, following by the design theory of the phase differences and the relation with beam steering for the BLM and BFN. A 4×4 BLM has been taken as an example, then the design procedure has been expanded to $N\times N$ BLM.

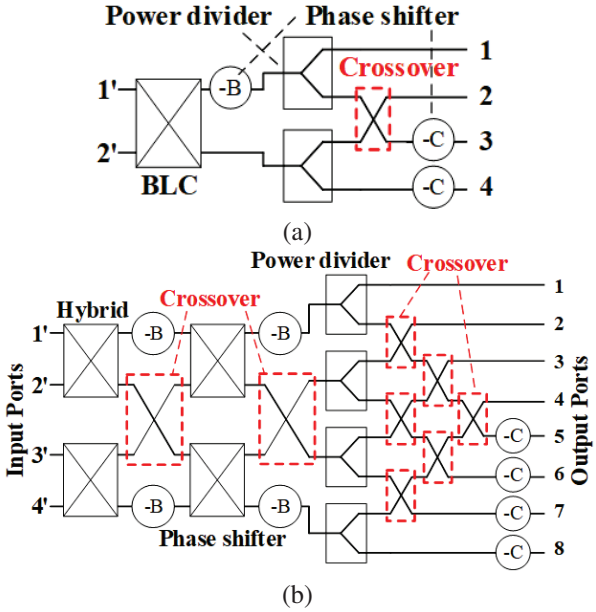

Fig. 1. Conventional (a) 2×4 and (b) 4×8 BMs.

A. configuration of the 4×4 BLM

In view of the symmetry of the BM structure, the proposed $N\times N$ BLM can be divided into two $N/2\times N$ BM structures. Traditional $N/2\times N$ BM has complex structures and large number of components, as shown in Fig. 1. Considering that those two BMs have many overlapping parts, the 4×4 BLM can be constructed in two ways: a single 2×4 BM structure with two reconfigurable working states, or two independent 2×4 BM structures grouped through SPDT switches.

As shown in Fig. 2 (a), a couple of 2×4 BM structures can generate different beam distributions by the alternation of working State 1 and State 2. For example, SPDT switches are used to access different phase shifters related to different states. In Fig. 2 (b), two states of independent 2×4 BM structures are adopted, defined as State 3. The schematics of the 4×4 BLM shown in Fig. 2 possess four input ports 1', 2', 3 ', 4' and four output ports 1, 2, 3, 4. The output ports are connected and switched through a group of parallel SPDT switches. The 2×4 BM structure is constructed on a three-layer circuit, so that

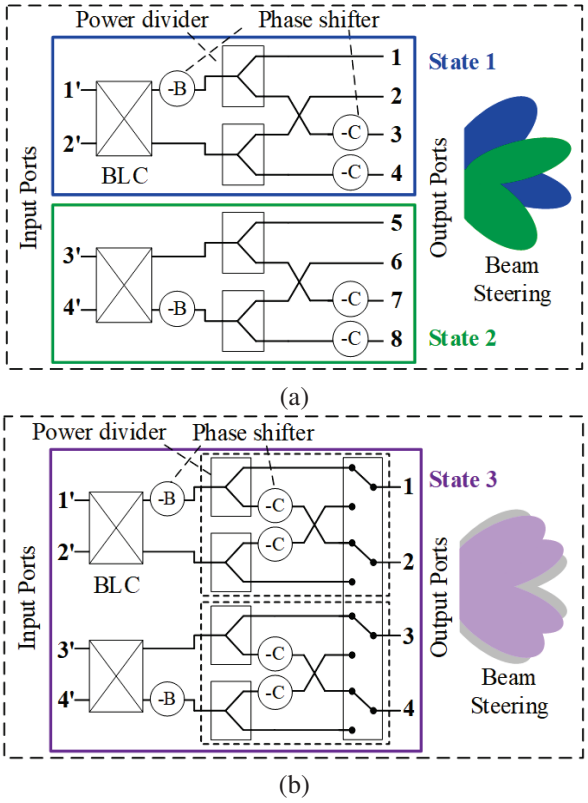

Fig. 2. Schematics of the proposed 4×4 BLM based on 2×4 BM, working at (a) State 1 and 2, (b) State 3.

the crossover could be eliminated by multilayer configuration. Then we can get a 4×4 BLM structure similar to a conventional 4×4 BM, which is easy to analyze and is illustrated later.

A four-port generalized coupled network (GCN) is designed to construct the BLM, which is composed of two power dividers, two phase-shift units, and two shunt SPDT switches, as shown in Fig. 3. The forward phase difference A_1 excited by port 1 and the reverse phase difference A_1' excited by port 2 are no longer limited to $A_1+A_1'=180°$. The first-stage coupling structures connected with the outputs are two GCNs, with forward

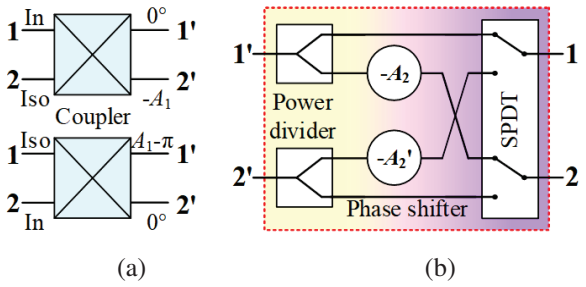

Fig. 3. Schematics of (a) A-PD coupler, (b) GCN.

Table 1: Phase responses of the 4×4 BLM

	Port1	**Port2**	**Port3**	**Port4**
Port1'	-B1	-A3	-B1-A1	-A2-A3
Port2'	-B1-A3'	0°	-B1-A1-A3'	-A2
Port3'	-A1'	-B2-A2'-A4	0°	-B2-A4
Port4'	$-A_1$'-A_4'	$-B_2$-A_2'	$-A_4$'	$-B_2$

phase differences of $\{A_1, A_2\}$ and reverse phase differences of $\{A_1', A_2'\}$. The coupling structures in the second stage close to the input consist of two traditional couplers with forward and reverse phase differences of $\{A_3, A_4\}$ and $\{A_3', A_4'\}$. Two phase shifters with phase shifts of $\{B_1, B_2\}$ are arranged. When fed by port i', the phase of output ports m and n are $\delta_{mi'}$ and $\delta_{ni'}$, with the phase differences being $\delta_{i'-mn}=\delta_{mi'}-\delta_{ni'}$ ($i, m, n\in\{1,2,3,4\}$).

B. Phase differences of the 4×4 BLM

When the input ports 1'∼4' are excited respectively, the phase responses of the BLM are shown in Table 1. The phase differences between port m and m+1 for different input ports can be summarized as follows:

$$\begin{aligned}
\Delta\delta_{1'-21} &= -A_3 + B_1, \Delta\delta_{1'-32} = -\Delta\delta_{1'-21} - A_1, \Delta\delta_{1'-43} \\
&= \Delta\delta_{1'-21} + \Delta A, \\
\Delta\delta_{2'-21} &= A_3' + B_1, \Delta\delta_{2'-32} = -\Delta\delta_{2'-21} - A_1, \Delta\delta_{2'-43} \\
&= \Delta\delta_{2'-21} + \Delta A, \\
\Delta\delta_{3'-21} &= \Delta\delta_{3'-43} + \Delta A', \Delta\delta_{3'-32} = -\Delta\delta_{3'-43} + A_2', \\
&\Delta\delta_{3'-43} = -A_4 - B_2, \\
\Delta\delta_{4'-21} &= \Delta\delta_{4'-43} + \Delta A', \Delta\delta_{4'-32} = -\Delta\delta_{4'-43} \\
&+ A_2', \Delta\delta_{4'-43} = A_4' - B_2,
\end{aligned} \tag{1}$$

where $\Delta A = A_1$ - A_2, $\Delta A' = A_1'$ - A_2'. According to different sets of the GCN's phase differences, the performances of the BLMs are discussed respectively.

There is $A_i + A_i' = 180°$ for an arbitrary coupler in a universal BLM with equal phase interval (EPI), which brings about the restriction between $\delta_{1'}$ and $\delta_{4'}$. Besides, there is $B_1 + B_2 = 90°$. The phase differences of the neighboring output ports can be re-written as

$$\delta_{1'} = -A_1/2 \tag{2a}$$

$$\delta_{2'} = 180° + \delta_{1'} \tag{2b}$$

$$\delta_{3'} = \delta_{1'} - 90° \tag{2c}$$

$$\delta_{4'} = \delta_{1'} + 90°. \tag{2d}$$

It is apparent that all the output phase differences $\delta_{1'}\sim\delta_{4'}$ are bound up with a single variable of A_1. By introducing the arbitrary-phase-difference (A-PD) couplers, the phase differences would vary with A_1, referring to an A-PD BLM with flexible beam controllability.

The phase differences of BLM with equal phase differences satisfies $\delta_{i'-21} = \delta_{i'-32} = \delta_{i'-43}$, simplified as $\delta_{i'}$ ($i\in\{1,2,3,4\}$). The design parameters of the BLM EPD can be calculated by

$$\begin{cases}
A_1 = A_2 = 2A_3 - 2B_1 + 2k\pi, k \in Z \\
A_1' = A_2' = 2A_4' - 2B_2 + 2k\pi, k \in Z \\
A_3 + A_3' = k\pi, k \in Z \\
A_4 + A_4' = k\pi, k \in Z
\end{cases}. \tag{3}$$

The sum of forward and reverse phase differences for couplers A_3 (or A_4) is 180°, which is consistent with the design schemes above. The inherent properties contribute to the limitation of the phase differences: $\delta_{2'} - \delta_{1'} = 180°$, $\delta_{4'} - \delta_{3'} = 180°$.

Traditional BMs are composed of 90° hybrids and 45° phase shifters, defined as Case A with $A_1 = A_2 = A_3 = A_4 = 90°$, $B_1 = B_2 = 45°$. It means that the output phase differences $\delta_{1'}\sim\delta_{4'}$ have fixed values of -45°, 135°, -135°, and 45°. By introducing the arbitrary-phase-difference (A-PD) couplers, the phase differences would vary with A_1, referring to an A-PD BLM with flexible beam controllability. For example, given that Case B with $A_1 = A_2 = 130°$, $A_1' = A_2' = 50°$, $A_3 = A_4 = 90°$, and $B_1 = 25°$, $B_2 = 65°$, the BLM EPI possesses the flexible phase differences of $\delta_{1'} = -65°$, $\delta_{2'} = 115°$, $\delta_{3'} = -155°$, and $\delta_{4'} = 25°$. The array patterns of this A-PD 4×4 BM in Case B is depicted in Fig. 4 (a) with comparison to Case A. The ideal simulated results are calculated by MATLAB. It can be seen that the phase intervals of any two-output ports with adjacent beams are 90°.

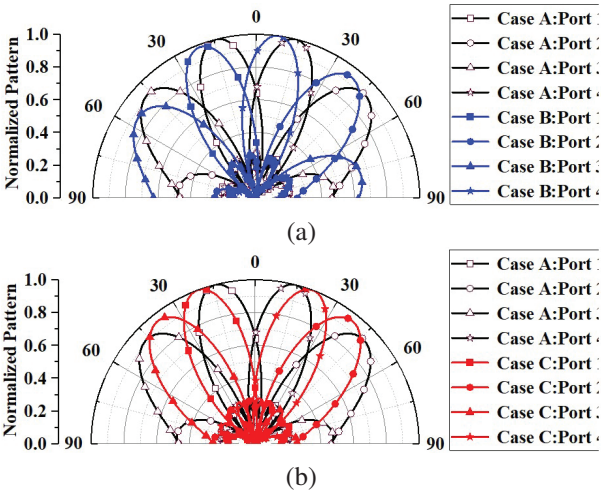

Fig. 4. Array patterns of traditional BM in Case A with (a) BLM EPI in Case B and (b) BLM UEPI in Case C.

Although the universal BLM EPD based on traditional couplers can extend the range of the radiation beam angles, it suffers from two main defects: a) phase intervals between adjacent output ports are fixed inherently; b) the beams of the antenna fed by BLM EPI are not symmetrical about the vertical axis of $\theta = 0°$.

In order to solve the defects of BLM EPI, the restrictions of the forward and reverse phase differences for

couplers A_1 (or A_2) should be broken. According to formula (2), it can be obtained that the situation of $A_i + A_i$' $\neq 180°$ needs to be considered, which means A_1 (or A_2) and A_1' (or A_2') could be designed flexibly and arbitrarily. The relationships between $\delta_{1'}$ and $\delta_{4'}$ in (2d) are re-defined as

$$\delta_{4'}=A_2^{'}/2. \tag{4}$$

The phase intervals between two output ports with adjacent beams can be calculated by [11]:

$$\begin{matrix}\Delta\delta_{3'}-\Delta\delta_{1'}=\Delta\delta_{4'}-\Delta\delta_{2'}=A_1/2+A_1/2-180°\\ \Delta\delta_{2'}-\Delta\delta_{3'}=-\left(A_1/2+A_1/2\right)\end{matrix}. \tag{5}$$

From (5) we can see that the phase intervals are no longer constant at 90°. That is, the phase differences of the BLM with unequal phase interval (UEPI) $\delta_{1'}$ relevant to A_1 (or A_2) and $\delta_{4'}$ relevant to A_1' (or A_2') could be designed independently and respectively. For simplification, assume that A_3 and A_4 is 90°. Then combining (2), (4), and (5), the design equations could be derived as

$$\begin{cases}\delta_{1'}=-A_1/2\\ \delta_{2'}=A_2/2+2B_1\\ \delta_{3'}=-A_2/2-2B_2\\ \delta_{4'}=A_2^{'}/2\end{cases}. \tag{6}$$

Take a BLM UEPI as Case C, with $A_1 = A_1' = A_2 = A_2' = 130°$, $A_3 = A_4 = 90°$, and $B_1 = B_2 = 25°$ for example; this would produce phase differences of -65°, 115°, -115°, and 65° under the excitation of P1'∼P4'. A symmetrical distribution relationship appears for the array patterns of this BLM UEPI, as illustrated in Fig. 4 (b).

C. Design procedures of the N×N BLM

In general, we extend the design schemes to the $N\times N$ BLM with $N = 2^n$ input or output ports. There are n-stage coupling structures, each stage of which includes $N/2$ coupling networks. The phase differences of the output ports are recorded as $\delta_{1'}\sim\delta_{N'}$. On the basis of with the constructions and analysis cases, the properties of the proposed BLM based on four-port GCNs have been summarized in the following:

a) All the coupling structures on the first stage have the same positive and negative output phase differences to achieve equal phase differences.

b) The relationship between $\delta_{1'}$ and $\delta_{N'}$ is determined by the sum of the positive and negative output phase differences coupling structure on the first stage. The relationships of $\delta_{1'}\sim\delta_{(N/2-1)'}$ and $\delta_{(N/2)'}\sim\delta_{N'}$ are relevant to the sum of the positive and negative output phase differences coupling structure on stage 2∼n.

c) The coupling structures on the first stage have been designed as four-port GCNs, and those on the second to the n^{th} stages are 90-degree hybrids. The phase differences of the BLMs would be carried out according to the analysis and iterations.

III. SIMULATION AND EXPERIMENT

A. Circuit constitution

The parameters of the proposed 4×4 BLM are set up according to equations (2) to (6), distributed on Ro4730 with the relative permittivity 3.0 and loss tangent 0.002. The overall circuits are distributed on three layers, as shown in Fig. 5, the middle of which acts as the reference ground, and the thickness between each layer is represented as h = 30 mil. The BLM consists of two multi-layer couplers, two phase shifters, and two filtering GCNs, skipping the crossover. All the units of the BLM will be introduced respectively.

The couplers in the first stage are branch line couplers (BLC) with two sections. The circuits on the top layer and those on the bottom layer are symmetrical about the ground. Each layer of the BLC has two transmission lines, possessing impedance Z_1 and electrical length $\theta = \lambda/4$, and three stubs, with impedance and electrical length of (Z_2, θ) on either side and (Z_3, θ) in the middle. The end of the three stubs on Layer 1 is connected with those on Layer 3 by metal vias passing through the ground. Owing to the symmetric structure of the proposed coupler, the scatting parameters can be analyzed and calculated by the even- and odd- mode theory.

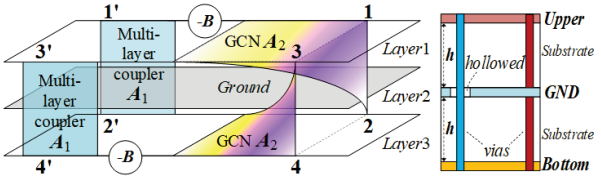

(a) (b)

Fig. 5. (a) Schematic and (b) cross section of the BLM.

The couplers in the second stage are GCNs, which are composed of power dividers, phase-shifting structures, and filtering switches. The circuit parameters of the multistage coupled-line structure and lumped elements in the filtering SPDT switch can be obtained based on the analysis of the equivalent circuit model by transforming transmission line sections into J-inverters. The capacitors $C_2\sim C_4$ are shorted with metal vias into the ground plane on Layer 2 for the DC terminal. Then the GCN shows a forward phase difference of A and reverse phase difference of A' when different signal paths of the SPDT are switched on. The phase control units provide phase shifts of A and A' for the forward and reverse phase differences of GCN, respectively.

The three-layer topology of the proposed 4×4 BLM has inherent isolation for different paths so that the numbers of crossovers are decreased.

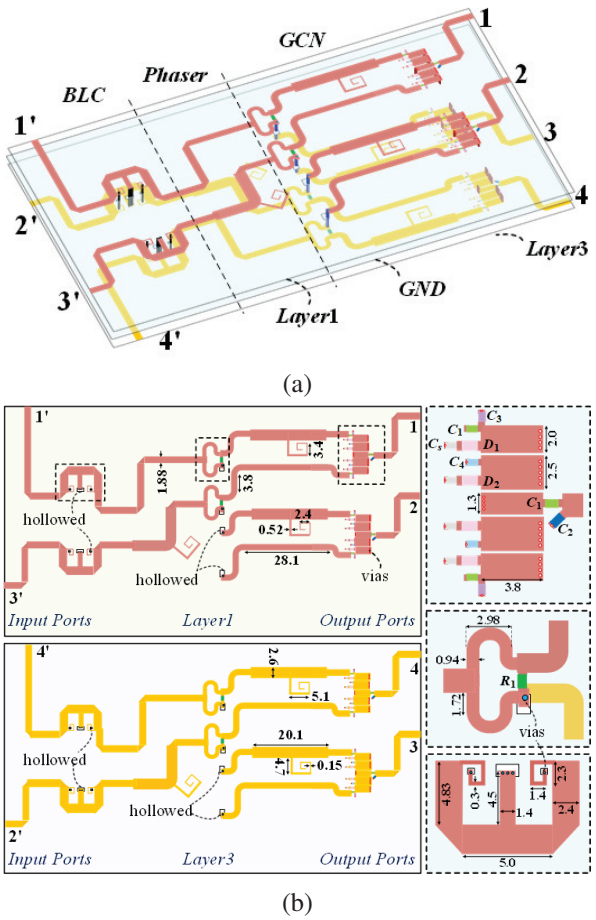

Fig. 6. Schematics of the 4×4 BLM: (a) 3D layout and (b) top view with physical parameters.

B. Simulated and measured results

A 4×4 BLM working at 4.9 GHz with unequal phase intervals and equal phase differences has been designed and simulated by employing design parameters of $A_1 = A_2 = 60°$, $A_3 = A_4 = 90°$, and $B_1 = B_2 = 60°$. The 3D layout and top view of the multi-layer circuit have been shown in Fig. 6, of which each unit is designed as mentioned before. Considering the BLM is arranged symmetrically to the horizontal central line, performances of the BLM when P1' (or P2') is excited are the same as those under the excitation of P4' (or P3'). A coupler working at 4.9 GHz and relative bandwidth of 40% is designed and optimized by employing the full-wave EM simulator.

The simulated *S*-parameters and the phase properties of both the first coupling network as BLC and the second coupling structure of GCN are displayed in Fig. 7 [11]. The physical parameters of the BLC are shown in Fig. 6 when $Z_1 = 42.6\ \Omega$, $Z_2 = 113\ \Omega$, and $Z_3 = 62.6\ \Omega$. Besides, the metal ground of Layer 2 is hollowed out

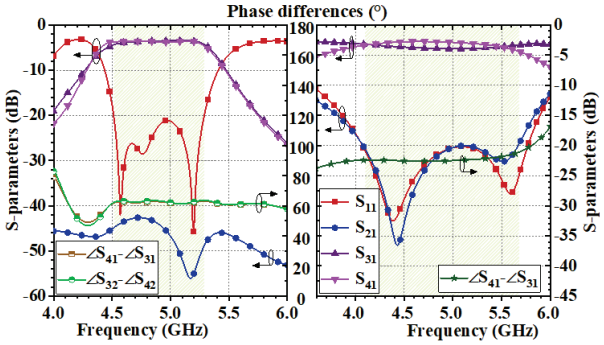

Fig. 7. Simulated *S*-parameters and phase differences of the coupling networks in (a) first stage and (b) second stage.

around the vias to avoid earth short. The proposed GCN is composed of two power dividers, two phase shifting structures, and two filtering SPDT switches with C_1 and C_2 being 0.3 pF, C_3 being 0.2 pF, and C_4 being 1 pF. The diodes $D_1 \sim D_4$ employ SMP1345-079LF (with L_s = 0.7 nH, R_{ON} = 2 Ω, and C_{OFF} = 0.15 pF). The capacitors and resistors are implemented in 0402 and 0603 size respectively. Besides, both the forward and reverse phase differences are around 60°, breaking the limitation $A + A' = 180°$ of normal BLC.

The fabricated BLM, as illustrated in Fig. 8 working at 4.9 GHz employs the design parameters of $A_1 = A_2 = A_1' = A_2' = 60°$, $A_3 = A_4 = A_3' = A_4' = 90°$, and $B_1 = B_2 = 60°$. In Fig. 9, the simulated and measured phase shifters of the BLM have been illustrated. In the simulated phase shifters of the 4×4 BLM with P1'∼P4' excited respectively, there is flexible phase differences

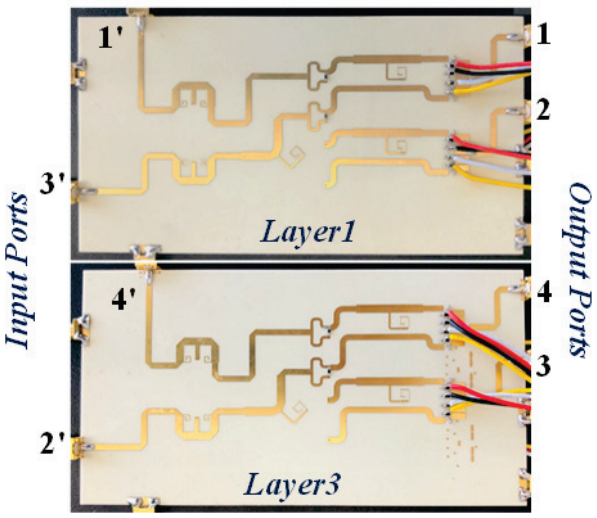

Fig. 8. Photograph of the fabricated BLMs.

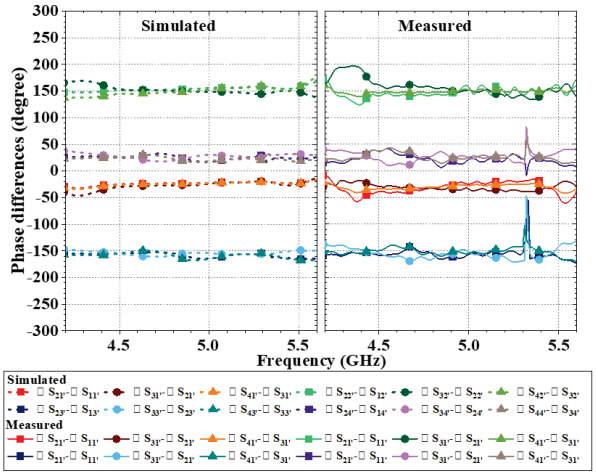

Fig. 9. Simulated and measured phase differences between adjacent output ports of the 4×4 BLM with P1'-P4' excited.

of $\delta_{1'}$ = -30°, $\delta_{2'}$ = 150°, $\delta_{3'}$ = -150°, and $\delta_{4'}$ = 30°. While forming the measured results of the BLM, the phase differences at 4.9 GHz are about -32.7°∼ -27.6°, 145.5°∼ 151.4°, -161.2.4°∼ -151.8°, and 17.9°∼ 25.0° with P1'∼P4' excited, respectively.

Figure 10 shows the simulated and measured *S*-parameters of the BLM. As we know, the input ports P1' and P4' of the proposed BLM are symmetric; so are P2' and P3'. Thus, only the experimental results under the excitation of P1' and P2' are presented in this case. According to the simulated scatting parameters, the bandwidth of the 4×4 BLM (with S_{11}, S_{22}, S_{33}, and S_{44} below 15 dB) is about 0.9 GHz (18.4%) ranging from 4.4 GHz to 5.3 GHz. As for the experimental results measured by the Vector Network Analyzer, the return losses and isolations are better than 11 dB for the working band from 4.4 to 5.3 GHz. When P1' is excited, the measured transmission coefficients from P1' to P1∼P4 are -9.6∼-7.5, -8.6∼-7.8, -10.0∼-9.5, and -9.9∼-9.1 dB. When P2' is excited, the measured transmission coefficients of S_{12}', S_{22}', S_{32}', and S_{42}' are -9.6∼-7.5, -8.6∼-7.8, -10.0∼-9.5, and -9.9∼-9.1 dB.

C. Beam steering of AA with proposed BLM

The radiation pattern has been calculated with the simulated and measured results in the previous sections. Figure 11 reveals that the normalized measured radiation beams point to -8.5° for the input port P1', 42.7° for input port P2', -45.3° under the excitation of P3', and 7.9° when P4' excited. The beams show symmetry distribution with respect to the vertical axis, consistent with the desired effect.

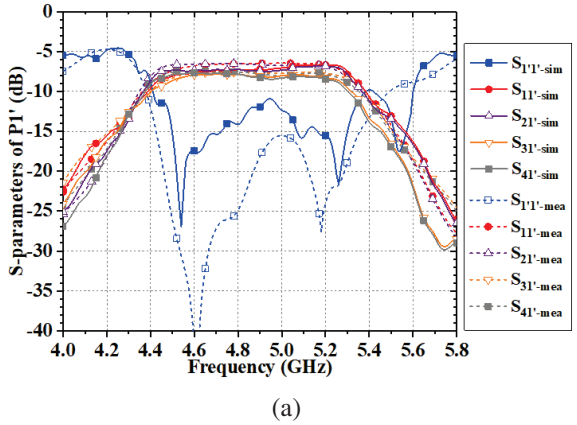

(a)

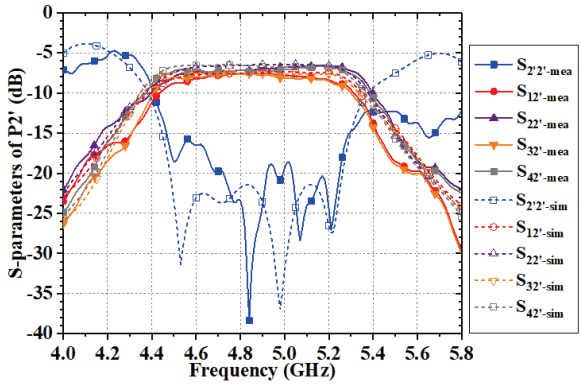

(b)

Fig. 10. Simulated and measured *S*-parameters of the 4×4 BLM with (a) P1' and (b) P2' excited.

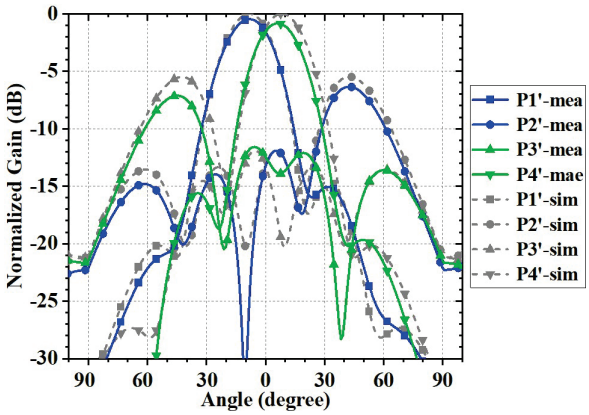

Fig. 11. Radiation patterns of linear antenna array fed by the proposed 4×4 BLM with measured results.

IV. CONCLUSION

In this paper, a universal topology of the filtering-integrated BLM with arbitrary phase phases has been proposed in three-layer construction. The 4×4 BLM operating at 4.9 GHz were designed, fabricated, and measured, exhibiting a bandwidth about 18.4% and a

compact size of 1.2×2.3 $\lambda_g{}^2$. The proposed BLM possesses such characteristics as compact size, filtering integration, wide working band, and flexible phase differences. It is worthy for further application to smart antennas and wireless communications.

ACKNOWLEDGMENT

This work was supported in part by National Key Research and Development Program of China (No. 2021YFB2900303). This paper is an expanded version from the International Applied Computational Electromagnetics Society (ACES) Symposium, Hangzhou, China, Aug. 2022 [11].

REFERENCES

[1] E. Dahlman, G. Mildh, S. Parkvall, J. Peisa, J. Sachs, Y. Selén, and J. Sköld, "5G wireless access: Requirements and realization," *IEEE Commun. Mag.*, vol. 52, no. 12, pp. 42-47, Dec. 2014.

[2] N. Tiwari and T. R. Rao, "A switched beam antenna array with Butler matrix network using substrate integrated waveguide technology for 60 GHz radio," *Applied Computational Electromagnetics (ACES) Journal*, vol. 31, no. 5, pp. 599-602, Aug. 2021.

[3] K. Tekkouk, J. Hirokawa, R. Sauleau, M. Ettorre, M. Sano, and M. Ando, "Dual-layer ridged waveguide slot array fed by a butler matrix with sidelobe control in the 60-GHz band," *IEEE Trans. Antennas Propag.*, vol. 63, no. 9, pp. 3857-3867, Sep. 2015.

[4] W. Yang, Y. Yang, W. Che, C. Fan, and Q. Xue, "94-GHz compact 2-D multibeam LTCC antenna based on multifolded SIW beam-forming network," *IEEE Trans. Antennas Propag.*, vol. 65, no. 8, pp. 4328-4333, Aug. 2017.

[5] H. N. Chu and T.-G. Ma, "An extended 4×4 Butler matrix with enhanced beam controllability and widened spatial coverage," *IEEE Trans. Microw. Theory Techn.*, vol. 66, no. 3, pp. 1301-1311, Mar. 2018.

[6] F. E. Fakoukakis and G. A. Kyriacou, "On the design of a Butler matrix-based beamformer introducing low sidelobe level and enhanced beam-pointing accuracy" in *Proc. IEEE-APS Top. Conf. Antennas Propag. Wireless Commun. (APWC)*, pp. 12-16, Sep. 2011.

[7] Y. Wu, J.-Y. Shen, Y. Liu, S.-W. Leung, and Q. Xue, "Miniaturized arbitrary phase-difference couplers for arbitrary coupling coefficients," *IEEE Trans. Microw. Theory Techn.*, vol. 61, no. 6, pp. 2317-2324, June 2013.

[8] A. A. M. Ali, N. J. G. Fonseca, F. Coccetti, and H. Aubert, "Design and implementation of two-layer compact wideband Butler matrices in SIW technology for Ku-band applications," *IEEE Trans. Antennas Propag.*, vol. 59, no. 2, pp. 503-512, Feb. 2011.

[9] B. Cetinoneri, Y. A. Atesal, and G. M. Rebeiz, "An 8×8 Butler matrix in 0.13-μm CMOS for 5-6-GHz multibeam applications," *IEEE Trans. Microw. Theory Techn.*, vol. 59, no. 2, pp. 295-301, Feb. 2011.

[10] S. A. Babale, "PET-based instant inkjet-printed 4×4 Butler matrix beamforming network," *Applied Computaional Electromagnetics (ACES) Journal*, vol. 37, no. 02, pp. 199-208, July 2022.

[11] L. Ma, "Design of multi-layer filtering Butler-like matrix with flexible phase differences," *Applied Computational Electromagnetics (ACES) Journal Symp.*, July 2022.

[12] Y. M. Hussein, M. K. A. Rahim, N. A. Murad, and H. O. Hanoosh, "Low loss wideband 4×4 Butler matrix networks based on substrate integrated waveguide for 5G applications," *IEEE Access*, 2023. doi:10.1109/ACCESS.2023.3342713

[13] S. Tang, Y. Zhang, J. Rao, Z. Han, C.-Y. Chiu, and R. Murch, "Beamforming network design utilizing node microstrip architectures for dual-polarized endfire millimeter-wave antenna arrays," *IEEE Trans. Antennas Propag.*, vol. 71, no. 6, pp. 4862-4873, June 2023.

Li Ma received the B.S. degree and the Ph.D. degree in electronic science and technology from Beijing University of Posts and Telecommunications (BUPT), Beijing, China, in 2017 and 2022, respectively. She is currently working as a researcher at the Department of Mobile Communications and Terminal Research of China Telecom Research Institute. Her research interests include wireless communication, microwave components, and antenna technology.

Lei Wang is a senior engineer of China Telecom. He received the B.S. and M.S. degrees in information and communication engineering from the Xidian University, Xi'an, China, in 2001 and 2004, respectively. He is now working as a senior engineer at the Department of Mobile Communications and Terminal Research of China Telecom Research Institute. His research interests include 5G communications and key technology of terminals.

Xiaodong Chen is a deputy senior engineer of China Telecom. He received the B.S. and M.S. degrees in communication and information system from the South China University of Technology, Guangzhou, China, in 1999 and 2002, respectively. From 2002 to 2011, he was a researcher with the Wireless Communication Department of Guangdong Scientific Telecommunication Academy. From 2012 to 2023, he was a project manager and a senior expert of the Mobile Communication Department of China Telecom Research Institute. His research interests include backscatter communications and 6G vision.

Discussion of the Transmission Efficiency of Quasi-optical Reflector Antenna Across Various Levels of Feeder Performance

Haoran Zhang and Ming Jin

College of Information Science and Technology
Beijing University of Chemical Technology, 100191 Beijing, China
2023210600@mail.buct.edu.cn, jinming@mail.buct.edu.cn

Abstract – For microwave radiometer calibration, higher main beam efficiency reduces interference from environmental brightness temperature (BT). A key challenge for high-frequency microwave sounders is achieving high main beam efficiency with limited mirror size. Although efficiency has improved to around 95-98%, there is still room for improvement. This study investigates the main beam efficiency of ground-based radiometer antenna systems, considering feeders with different radiating qualities and mirror conditions. A quasi-ellipsoidal mirror with feeders operating at multiple discrete frequencies is designed to optimize the optical path for microwave calibration. The key focus is transmission efficiency, which affects BT leakage. Numerical results for various feeders are compared - straight wall corrugated horns with 98.2% Gaussian content, dual-mode horns with 98.5%, curved wall corrugated horns with 99.8%, and ideal Gaussian beams - highlighting achievable transmission levels in different polarizations with different feeders. Design curves for the high main beam efficiency quasi-optical reflector antenna system are provided. Such information is beneficial and of direct referencing value for practical radiometer reflector antenna designs.

Index Terms – Brightness temperature leakage, microwave radiometer calibration, quasi-optical reflector antenna.

I. INTRODUCTION

The microwave radiometer payload performs an important part in remote sensing techniques for monitoring the earth environment from surface to atmosphere [1, 2]. As the radiometer payloads passively detect weak and non-coherent thermal radiation from the earth environment, its antenna needs high gain, low side-lobe characteristics [3]. Thus, reflector antennas are often used in microwave radiometer systems.

The quasi-optical (QO) reflector antenna [4, 5] is a kind of compact reflector antenna which is suitable for applications of microwave sounders. It is based on optical system design ideas, where electromagnetic waves propagate in the form of a Gaussian beam in free space, and the width and curvature of the Gaussian beam can be controlled by the mirror, lens and other devices. A well-designed QO reflector antenna leads to less leakage, which is significant in radiometer applications.

Specifically in the calibration process, which is vital for radiometer quantitative observation, the leakage from the reflector antennas is an important factor, which should be suppressed as much as possible [6–11]. As can be found in the reported microwave radiometer payloads [6, 7, 9, 11], achieved main beam efficiency is at a level of 0.95∼0.98. Comparatively, the emissivity level of a modern calibration target is 0.999∼0.9999, which is another source of leakage disturbing calibration accuracy [12–14]. It can be concluded, leakage from the reflector antenna is a significant factor contributing to calibration error, as it leads to the notable intrusion of background brightness temperature (BT) which is generally hard to control or accurately model.

To minimize the leakage caused by reflectors, main beam efficiency needs to be further improved. However, there are no design guidelines specifically for achieving high main beam efficiency in QO reflector antennas. During designing a low-leakage QO antenna for a ground-based radiometer calibration test system with accuracy demands, the authors developed a set of prototypes with various levels of feeder performance, which leads to a comprehensive database for the quantitative conclusion for low-leakage design. In this work, the authors will demonstrate the quantitative analysis with further considerations of factors such as reflector size and polarization, forming a direct reference for designers of radiometer reflector antennas.

II. FORMULA DEFINITION

In this work, the authors utilized the factor of Gaussian content, which is the similarity level between horn antenna fields and the pure Gaussian fields of fundamental mode [15, 16], to govern the performance of the feeder. To further improve calibration accuracy, it is significant that the QO reflector antenna [17] can be with a main beam efficiency notably higher than the current level of 0.95∼0.98. High main beam efficiency is linked

Submitted On: November 6, 2024
Accepted On: January 24, 2025
https://doi.org/10.13052/2025.ACES.J.400207

to the Gaussian content of the feeder horn, which is a qualitative acknowledgement. However, it is of practical referencing value if the quantitative reference can be given, including both the factors of feeder Gaussian content and reflector size.

In this section, the authors will give specific definitions of Gaussian content and main beam efficiency in this analysis.

A. Gaussian content

Gaussian fundamental mode scalar field distribution can be expressed as:

$$u(\vec{r},\omega_0,z)=\frac{\omega_0}{\omega(z)}\exp(j\varphi_0)\exp(\frac{-jk_0r^2}{2q(z)}). \quad (1)$$

$\vec{r}$is the transverse position vector diameter perpendicular to the propagation direction, $\vec{r}=x\hat{x}+y\hat{y}$, $r=\sqrt{x^2+y^2}$, z is the propagation distance along the propagation direction (z-axis). z is 0 at the waist of the Gaussian beam (radius of the waist ω_0):

$$\omega(z)=\omega_0\sqrt{1+(\frac{\lambda_0 z}{\pi\omega_0^2})^2}, \quad (2)$$

$$q(z)=\frac{j\pi\omega_0^2}{\lambda_0}+z=(\frac{1}{R(z)}-\frac{j\lambda_0}{\pi\omega^2(z)})^{-1}, \quad (3)$$

$$R(z)=z(1+(\frac{\pi\omega_0^2}{\lambda_0 z})^2). \quad (4)$$

For the main polarization field$E^{col}(r)$ of the horn antenna, which is based on CST, the Gaussian content can be obtained at the radiation interface:

$$C(\omega_0,z)=\frac{\left|\int u(\vec{r},\omega_0,z)E^{col*}(r)ds\right|^2}{\int u(\vec{r},\omega_0,z)u^*(\vec{r},\omega_0,z)ds\int E^{col}(r)E^{col*}(r)ds}. \quad (5)$$

Figure 1 (a) shows the field $E^{col}(r)$(dB) in CST and Fig. 1 (b) shows the field $E^{col}(r)$ (linear) in our field analyses.

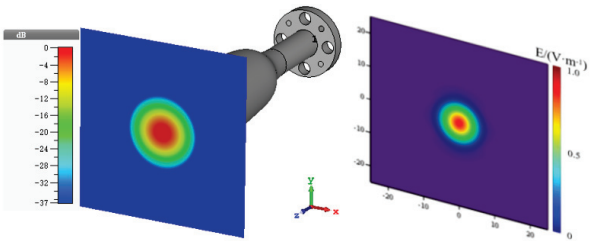

(a) (b)

Fig. 1. Main polarization field$E^{col}(r)$ of the horn antenna.

B. Main beam efficiency η and leakage

If a sufficiently large cross-section A_{inc} is taken near the front of the feed opening, the edge field is attenuated significantly. The field distribution on the interface is E_{inc}, H_{inc}, and the incident power is obtained by integrating the surface flux of the Poynting vector:

$$P_{inc}=\frac{1}{2}\int_{A_{inc}}(\vec{E}_{inc}\times\vec{H}_{inc})\cdot\hat{n}ds. \quad (6)$$

After passing behind the mirror far enough (across the observation area), take a cross-section $\boldsymbol{A}_{out}$ equal to the size of the reflector, define the exit field distribution of the cross-section as E_{out}, H_{out}, and obtain the exit power by integrating the surface flux of the Poynting vector:

$$P_{out}=\frac{1}{2}\int_{A_{out}}\left(\vec{E}_{out}\times\vec{H}_{out}\right)\cdot\hat{n}ds. \quad (7)$$

Main beam efficiency η (power transfer efficiency) is defined as:

$$\eta=P_{out}/P_{inc}. \quad (8)$$

Power transmission leakage is defined as:

$$leakage=1-\eta. \quad (9)$$

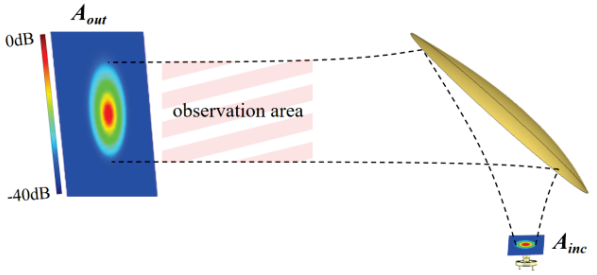

Fig. 2. Main beam efficiency η analysis scenario.

III. RESULTS AND COMPARISONS

In this part, the authors introduce the different kinds of feed horns used in QO antenna, and main beam efficiency is compared in different conditions.

The horn antennas here include the common horns which are often used in radiometer antenna system, such as the curved wall corrugated horn, the linear wall corrugated horn and the dual-mode horn [18, 19]. The far-field and near-field information of the reflector antenna are given, which can visually show the leakage of the reflector. Simulation value of main beam efficiency is discussed with different frequencies, polarization, kinds of feed horns and size of reflectors, which is significant to the design of radiometer reflector antenna system.

A. Horn antennas

This part introduces the structure and performance of feed horns which are often used in radiometers with three frequencies of 54, 89 and 118 GHz. The types of the feeders are the curved wall corrugated horns, linear profile corrugated horns and dual-mode conical horns (dual-mode horn is only designed in 89 and 118 GHz). Taking the design of 89 GHz frequency as an example, the typical structure of the feeds is shown in Fig. 3.

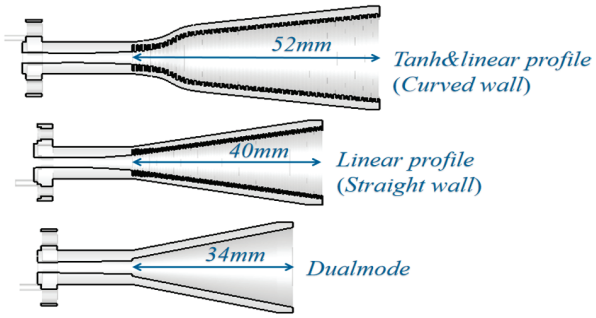

Fig. 3. 89 GHz feed horns.

The far-field pattern of the feed horn of each frequency is shown in Figs. 4–6. These feed horns can get a pretty good performance in far-field pattern that the side-lobe level is below -35 dB. It is worth noting that that far-field pattern of the curved wall corrugated horn rapidly rolls down with θ, which is important for a high-performance radiometer reflector antenna.

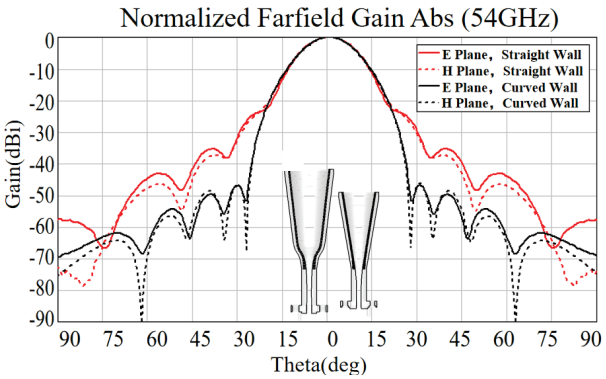

Fig. 4. 54 GHz far-field pattern. Red lines mark the angular coverage of the QO reflector with cross-section radius $L = 0.1$ m, and the distance Zc from the feed Gaussian waist position to the center of the reflector is 0.155 m.

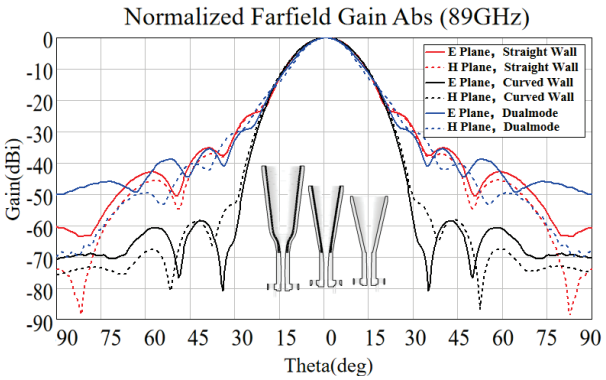

Fig. 5. 89 GHz far-field pattern.

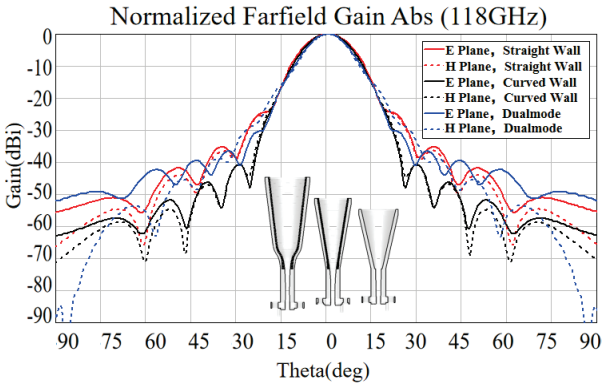

Fig. 6. 118 GHz far-field pattern.

As shown in Table 1, the Gaussian parameters of all feed horns at the three frequencies are summarized. The curved wall corrugated horn has the highest Gaussian content level of more than 99.5%, the straight wall corrugated horn and the dual-mode horn have a Gaussian content around 98.5%.

Table 1: Gaussian parameters of the feed horn

Feed Horn	ω_0/λ	**Gaussian Content**
Tanh&linear profile corrugated horn (54 GHz)	1.43±0.02	99.85%
Linear profile corrugated horn (54 GHz)	1.43±0.02	98.35%
Tanh&linear profile corrugated horn (89 GHz)	1.43±0.02	99.8%
Linear profile corrugated horn (89 GHz)	1.43±0.02	98.2%
Dual-mode horn (89 GHz)	1.43±0.02	98.8%
Tanh&linear profile corrugated horn (118 GHz)	1.64±0.02	99.7%
Linear profile corrugated horn (118 GHz)	1.64±0.02	98.2%
Dual-mode horn (118 GHz)	1.64±0.02	98.5%

B. Reflectors of different sizes

Information on the sufficient size of reflector for achieving a specific main beam efficiency is generally interesting for radiometer antenna designers. To conclude that information, the reflector instance is set to be with different truncated sizes for expanding the data range. Specifically, as shown in Fig. 7, L refers to the cross-section size of reflector and $\omega(z_c)$ refers to the ideal Gaussian beam waist radius when the beam propagates to the center of the mirror, so that the relative size of

the reflectors can be understood as $L/\omega(z_c)$. Our analysis of main beam efficiency includes five sizes of reflectors, which can help examine the relationship between main beam efficiency and the relative size of reflectors.

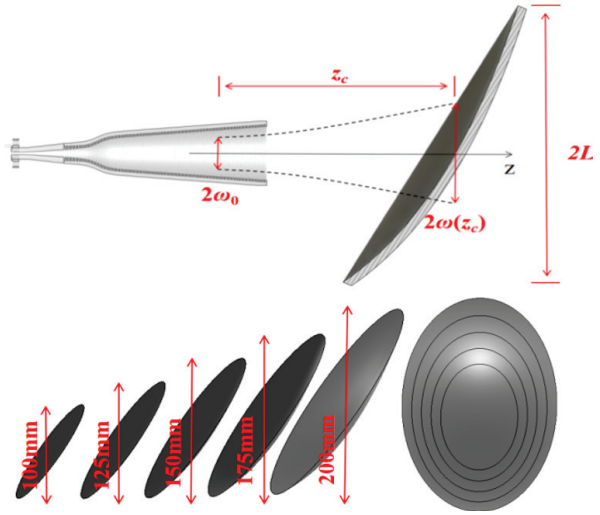

Fig. 7. Relationship between $\omega(z_c)$ and L.

C. Comparison of reflected fields in far-field and near-field

In this section, the authors showcase the reflected fields of 89 GHz, to help understand the phenomenon of reflector leakage. To the author's knowledge, the most important reason for reflector leakage is insufficient size of reflector for covering the diffusing fields from the small-aperture feeder. Meanwhile from the view of feeders, the ability to suppress wasted radiation in far off-axes angles is important for achieving high main beam efficiency. In the analysis, there are three different feeders - straight wall corrugated horn, dual-mode horn and curved wall corrugated horn - which have different levels of Gaussian content related to far off-axes side-lobe performance. Considering a relatively small reflector size ($L = 0.1$ m), one can easily see the power leakage in the 3D far-field pattern in Fig. 8, referenced with a pure Gaussian beam illumination. The Gaussian beam and curved wall corrugated horn cause less power leakage, while the straight wall corrugated horn can cause obvious power leakage.

Figure 9 shows how power transmission leakage occurs at 89 GHz. Specifically, the reason is the relative size between the beam width and the reflector. With the increase of Gaussian content level, leakage obviously decreases, which shows the significance of Gaussian content level of feed horns in radiometer reflector antennas. The normalized reflected electric fields of 89 GHz are shown in Fig. 10. We can see that the reflected

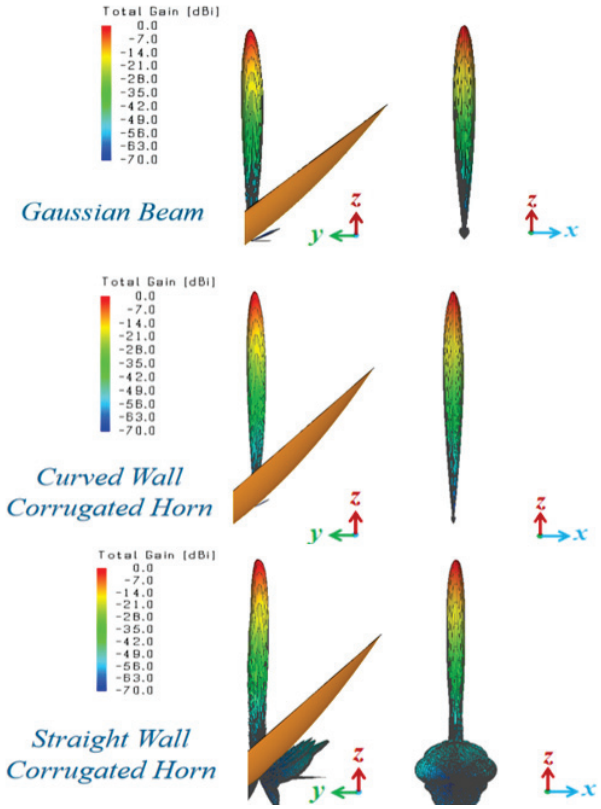

Fig. 8. 89 GHz normalized far-field pattern (from 0 to -70 dB [20]).

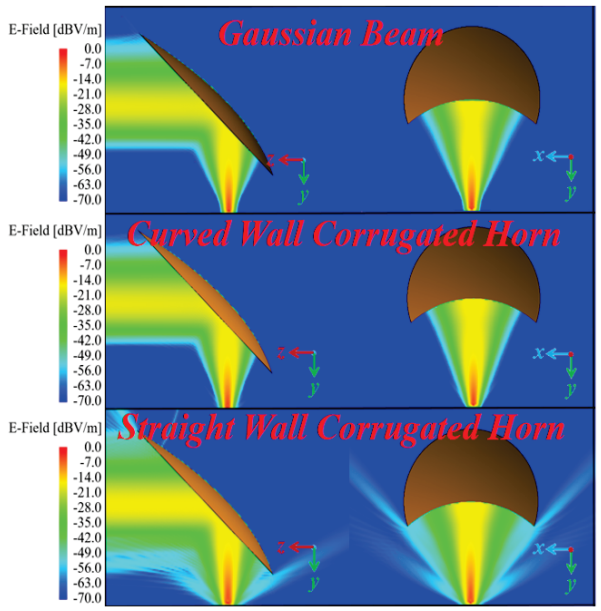

Fig. 9. 89 GHz near-field plane (from 0 to -70 dB [20]).

fields of Gaussian beam have the characteristics of power focusing and edge attenuation. The reflected fields of the

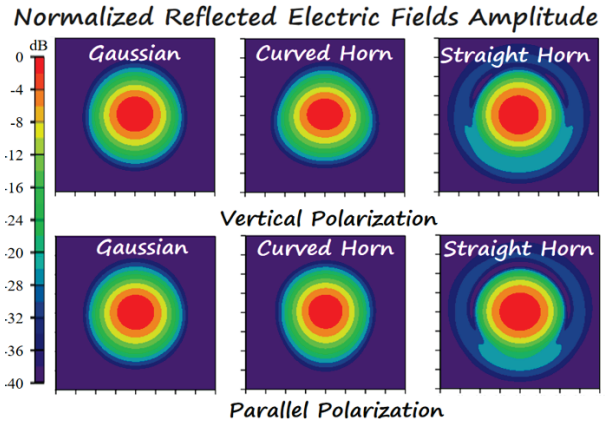

Fig. 10. 89 GHz normalized reflected electric fields amplitude (dB), considering the reflector with a cross-section radius $L = 100$ mm, which leads to η notably higher than 0.99.

curved wall corrugated horn are similar to the reflected fields of the Gaussian beam, while the reflected fields of the straight wall corrugated horn have poor beam quality, which means the straight wall corrugated horn (with a Gaussian content about 98.2%) will have a relatively bad performance in radiometer reflector antenna applications.

When further calculating main beam efficiency η using equations (7) and (8), the direct integrated physical optics (PO) algorithm is used, as it will not introduce numerical influences caused by the iterative solving process of the full-wave MLFMA (multi-layer fast multi-pole algorithm) of FEKO. However, as the diffraction algorithm is not included, the PO calculated fields do not contain the edge diffraction effects. Therefore, a method investigation has to be made on whether the edge diffraction effect is notable in the main area of considered parameter region.

Specifically, the authors compared the reflected fields by their PO and FEKO solvers (Fig. 11), in the case of the 89 GHz straight wall corrugated horn, and $L/w(z) = 2.167$ ($L = 0.075$ m). In this case, η is around 99%, which is the main parameter region where investigations are focused.

For the first comparison, the authors took a cross-section aperture of 0.2 m. The reflected fields are shown in the 40 dB dynamic range (Fig. 12), and the correlation between FEKO results and results from our program is above 0.999, as shown in Fig. 12. Thus, the PO calculation gives accurate results in the main-beam area. Further, in order to find field leakage caused by edge diffraction off the main-beam path, the authors took a larger cross-section area of 0.6 m. The reflected fields are shown in the 40 dB dynamic range and 60 dB dynamic range in Fig. 13. It can be observed that, for the weak

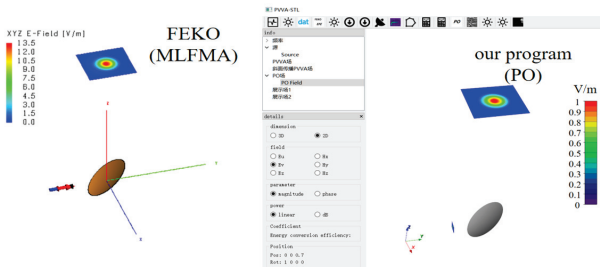

Fig. 11. Configuration of reflected fields calculation by FEKO (full wave MLFMA) left, and by our program based on physical optics (PO) right.

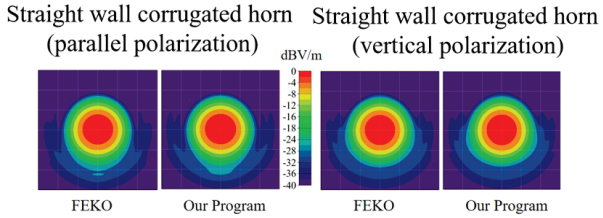

Fig. 12. Comparison between reflected field results of straight wall corrugated horn at 89 GHz in cases of parallel-pol and vertical-pol reflection (correlation efficiency between results by the two methods achieves a level of 0.999).

diffracted pattern away from the main-beam path, there are indeed differences in the two sets of results. However, the fields in the pattern-differed area are very weak compared to those in the main-beam area. Therefore, PO calculation is sufficient for field and further main beam efficiency analysis for cases of η>99%, without considering edge diffraction. However, it should be noted that, when reflected fields investigation is performed when η is notably lower, (0.95∼0.98), edge diffraction should be included in the analysis.

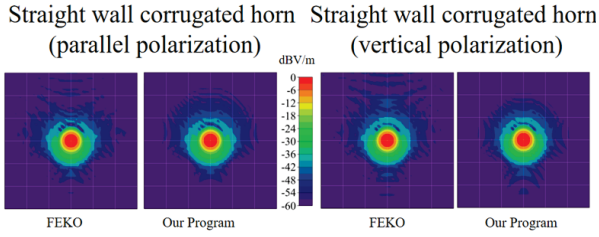

Fig. 13. Comparison of reflected field results by FEKO and PO: 89 GHz reflected fields of straight wall corrugated horn, parallel-pol and vertical-pol reflection (40 dB dynamic range, upper row, and 60 dB dynamic range, lower row).

D. Main beam efficiency

Next, the achieved main beam efficiency is calculated and analyzed in considered feeders at different frequencies of different beam waist radius and reflectors of different sizes. Figure 14 quantitatively shows the feeders with Gaussian content of about 98.5% and 99.5%, whose main beam efficiency changes with the relative size of the reflector. The vertical ordinates of Fig. 14 are main beam efficiency, and the horizontal ordinates are relative size of reflector (normalized by the equivalent beam waist radius of the propagated fields at the reflector). Main beam efficiency rises with Gaussian content. For example, Gaussian content of the pure Gaussian beam and curved corrugated horn are similar, and their main beam efficiency curves are similar too. Equally, the dual-mode horn antenna and linear profile corrugated horn show the same regularity.

A common horn antenna with 98.5% Gaussian content needs $L \approx 3\omega(z_c)$ to attain a high main beam efficiency of 99.5%. This is important in the design of radiometer reflectors.

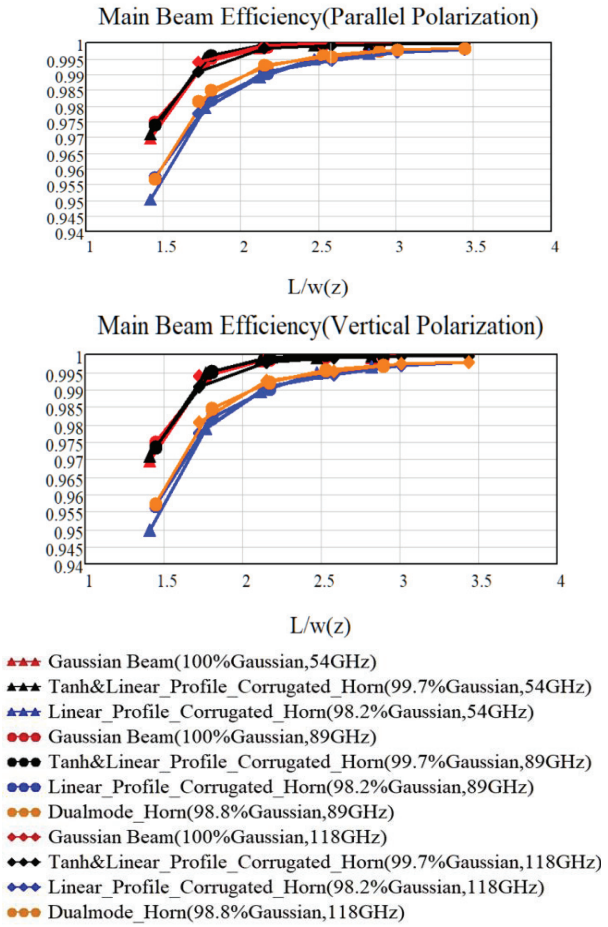

Fig. 14. Counted main beam efficiency η (parallel-pol and vertical-pol).

E. Leakage

Power transmission leakage can be obtained by main beam efficiency η from Fig. 14. Figure 15 shows the leakage when different horns irradiate different sizes of reflector antenna systems. In order to facilitate observation and analysis, a logarithmic scale is used in Fig. 15. After averaging the leakage of Gaussian beam and curved wall corrugated horns, we have a clearer insight on the leakage information shown in Fig. 16.

Regarding practical applications in radiometer systems, leakage of the QO reflector antenna is becoming notable for achieving a high-accuracy BT transfer, as progress in other factors have been made in recent years [6, 7, 9, 11]. For example, leakage from the calibration target can be reduced to a level of 0.0001 (emissivity>40 dB), while leakage from the reflector can be at a level over 0.01 (η<0.99, from the reported radiometer payloads design). The results of this work clearly indicate that achieving Gaussian content in the feeder (or QO feeder network) fields to the state-of-the-art level is of practical significance. This is particularly important for enhancing main beam efficiency when reflector sizes are limited.

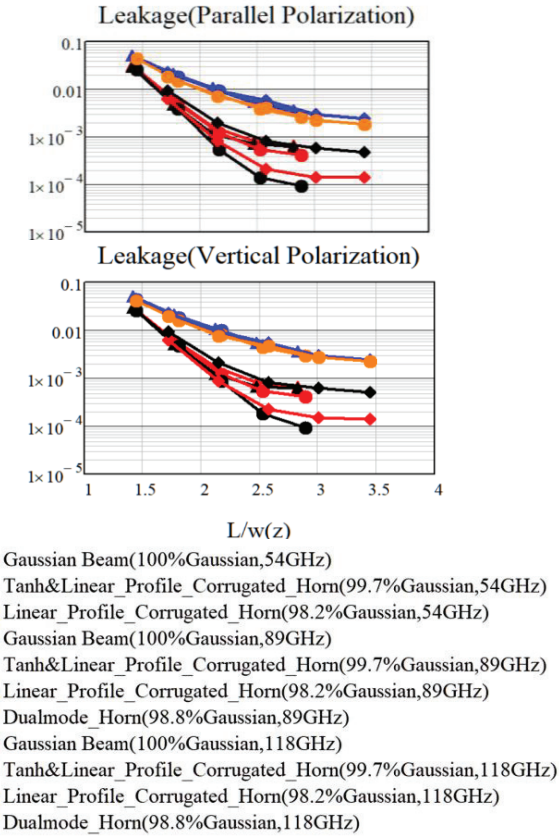

Fig. 15. Counted main beam efficiency η (parallel-pol and vertical-pol).

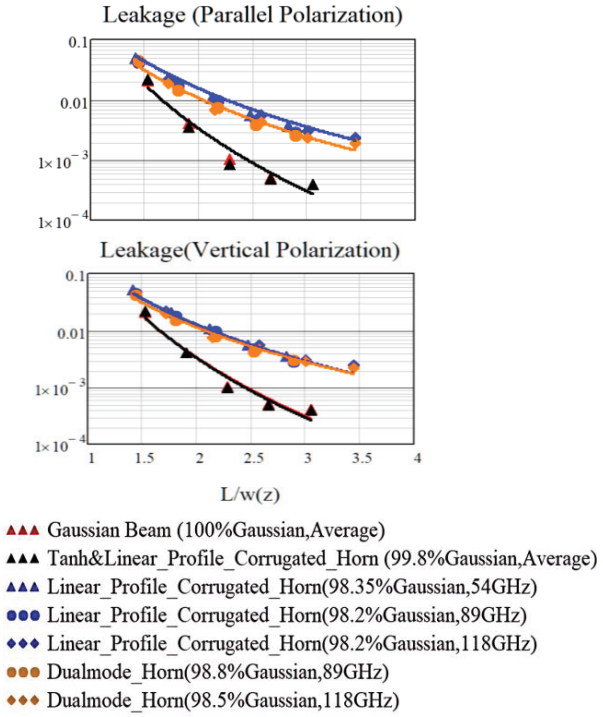

Fig. 16. Leakage of the reflector antenna (curve fitting, parallel-pol and vertical-pol).

F. Additional fabricated Ka-band instance

It is interesting and important that the curves in sections III D and E are of reference value to general QO designs. Therefore, in this section, a fabricated Ka-band feeder and its paired QO reflector are considered as in Fig. 17 (a). The feeder is a typical straight wall corrugated horn antenna, and it shall be noted that the Ka-band is out of the range of data instances in section III. The aperture fields of the Ka-band feeder are tested in Figs. 17 (b) and 18 (a). The reflected fields (parameters listed in Table 2) are calculated to show the achieved main beam efficiency, for comparison with concluded curves in section III.

Table 2: QO design parameters

Parameter	Length/m
cross-section of reflector (L)	0.1
radius of curvature 1 (R_1)	0.137
radius of curvature 2 (R_2)	0.512
incident distance (d_{in})	0.13
exit distance (d_{out})	0.287

In the specific calculation of main beam efficiency, the equivalent waist radius of the tested field was determined to be 1.08λ. From this, the beam waist radius at the reflector was calculated to be 4.25λ. Subsequently,

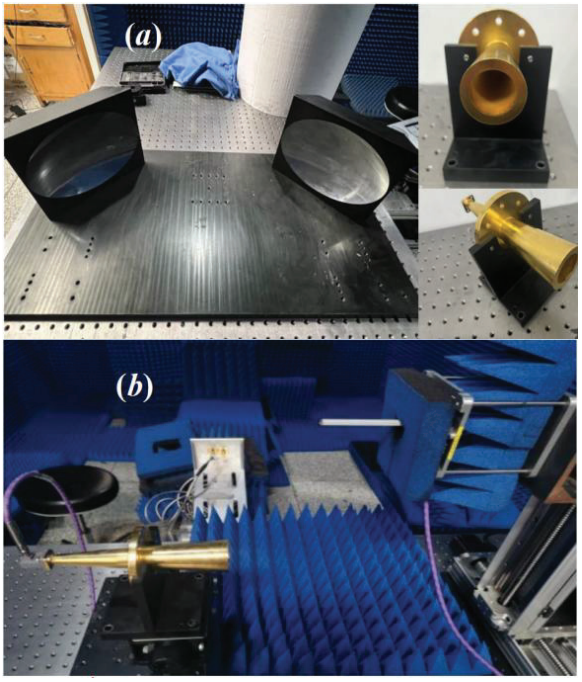

Fig. 17. The considered fabricated Ka-band straight wall feeder antenna and its aperture field testing configuration. (a) Feeder antenna and its paired QO reflector and (b) aperture field testing configuration (planar field scanning). (Feeder antenna and testing facility provided by the microwave engineering laboratory in Beihang University.)

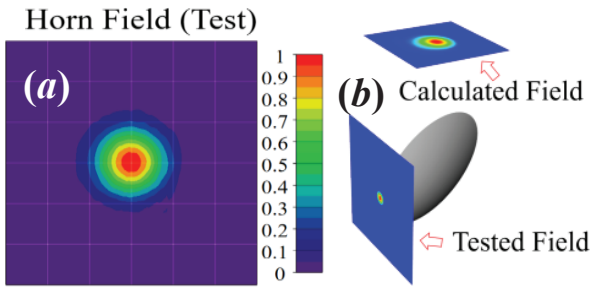

Fig. 18. (a) Tested fields of the Ka-band feeder and (b) computation configuration for the reflector reflected fields.

the reflected fields were computed (see Figs. 18 (b) and 19) to evaluate the main beam efficiency. The results are presented in Fig. 20, where a comparison with the curves derived in section III is made. As shown in Fig. 20, the results exhibit good agreement with the previously concluded curves. This example demonstrates that the curves presented in section III have practical reference value for typical QO designs.

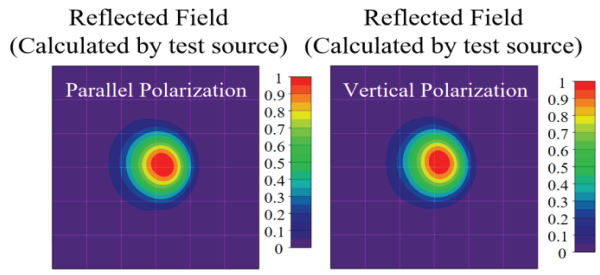

Fig. 19. Reflected fields in two polarization cases.

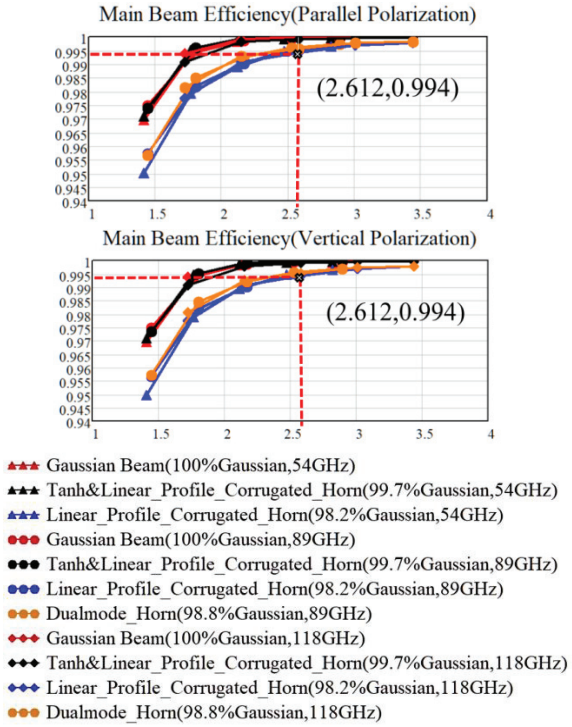

Fig. 20. Counted main beam efficiency results based on the tested Ka-band feeder aperture fields, and comparison with concluded curves based on 54 GHz/89 GHz/118 GHz feeders.

IV. DISCUSSION

This study is driven by the need to improve QO reflector main beam efficiency, which is becoming a notable obstructive factor in improving radiometer calibration accuracy. Compared with reported main beam efficiency level at 95∼98% in applied radiometer payloads, this study investigates the strategy to achieve main beam efficiency higher than 99%, and that ($\eta\sim99\%$) may be still not be enough for future requests from radiometer designers.

This study explores the relationship between power transmission leakage and reflector antenna design, considering different frequencies, Gaussian content of feeds and reflector sizes. Notably, the power transmission leakage for various frequencies follows a similar trend. It is clear that, besides the reflector size, the Gaussian content achieved by the feeder is also significant.

It is worth emphasizing that the rapid roll-off of the far-field pattern (feeder) is crucial for pursuing high efficiency at the cutting edge, which is shown for the curved-wall corrugated horn in Figs. 4–6. As can be found in Fig. 16, a very large reflector can be used with a 98.5% Gaussian content feed (straight wall horn or dual-mode horn), for pursing a 99.9% level of main beam efficiency. Further, it should also be noted, in the QO systems, beam propagation from the feeder to the reflector should not be directly considered as far-field but is a near-field process. Reflector leakage is found to be larger than it seems in the far-field pattern. For example, as shown in Fig. 4, angular coverage of the reflector with a $L = 0.1$ m can be $\pm33^{o}$ for the 54 GHz feeder (distance Z_c between the feeder Gaussian waist to the center of reflector is 0.155 m). Out of that angular region, the side-lobes are smaller than -30 dB for the straight wall corrugated feed (shown in Fig. 4), but the counted main beam efficiency is 0.996, which means a leakage notably larger than -30 dB happens.

The authors present these results to provide a universal reference for the design of QO reflector antennas aimed at achieving extremely high efficiency. Figure 14 shows the main beam efficiency values that a common radiometer reflector antenna can achieve according to different reflector sizes with different types of feeder antennas. The instance of Ka-band straight wall corrugated horn conforms the validity of the concluded curves as a common reference. It is clear that, for achieving an extremely high main beam efficiency, such as >0.999, the Gaussian quality of the QO feeder is significant. For example, if an extremely high performance QO reflector antenna is required with leakage less than 0.001, a reflector with $L\geq2.5\omega(z_c)$ and a well-designed horn with $\eta_g\sim99.5\%$ (Gaussian content) is necessary.

Although the calculated result of the main beam efficiency in Ka-band is in agreement with the analysis results of straight wall corrugated feeders, it is regrettable that η is not a measured value. When $\eta>0.99$, measuring the main beam efficiency becomes a technical challenge and requires further methodology development. The authors plan to further investigate the high efficiency QO reflector system (or the QO feed network), as it becomes significant for improving radiometer calibration accuracy. However, the investigations should focus on both the design implementation and the measurement validation.

V. CONCLUSION

In this paper, the authors analyzed the power transmission leakage of a reflector antenna under different feed types. The high Gaussian feed horn, characterized by its rapid roll-off in the far-field pattern, demonstrated superior performance in this study. Additionally, the power transmission leakage of the reflector antenna was quantitatively analyzed across various levels of feeder performance. These findings are universally applicable and hold practical significance for the design of high-performance reflector antennas used in radiometers.

ACKNOWLEDGMENT

The authors appreciate the help from Professor Ming Bai and Dr. Ning Leng at the Microwave Engineering Laboratory, Beihang University, for providing the measurement facility & equipment and technique support.

REFERENCES

[1] D. Draper, Q. Remund, D. Newell, and S. Krimchansky, "A comparison of GPM Microwave Imager (GMI) high frequency channel brightness temperatures to the Advanced Technology Microwave Sounder (ATMS)," in *IEEE International Geoscience and Remote Sensing Symposium (IGARSS)*, Milan, Italy, pp. 5146-5149, 2015.

[2] N. Sun and F. Weng, "Evaluation of Special Sensor Microwave Imager/Sounder (SSMIS) environmental data records," *IEEE Transactions on Geoscience and Remote Sensing*, vol. 46, no. 4, pp. 1006-1016, Apr. 2008.

[3] M. Jin, R. Yuan, X. Li, Y. Tao, Q. Gao, and M. Bai, "Wideband microwave calibration target design for improved directional brightness temperature radiation," *IEEE Geoscience and Remote Sensing Letters*, vol. 19, pp. 1-5, 2022.

[4] Z. Li, Y. Zhang, K. Liu, D. Liu, and J. Miao, "A millimeter and sub-millimeter wave multi-channel quasi-optical system for microwave radio-meter," in *IEEE Geoscience and Remote Sensing Symposium*, Quebec City, QC, Canada, pp. 3033-3036, 2014.

[5] A. L. Woodcraft, S. T. Froud, R. J. Wylde, P. A. R. Ade, R. V. Sudiwala, C. E. Tucker, S. M. Tun, M. Bray, P. Campbell, G. Maxwell-Cox, and V. Kangas, "Design and testing of the quasi-optical network for the MetOp-SG microwave sounder," in *17th European Conference on Antennas and Propagation (Eu-CAP)*, Florence, Italy, pp. 1-5, 2023.

[6] W. Hongjian, "Design and analysis of FengYun3 Microwave Humidity Sounder (FY3MHS) Antenna," in *IEEE International Symposium on Antennas and Propagation and USNC-URSI Radio Science Meeting*, Atlanta, GA, USA, pp. 471-472, 2019.

[7] I. A. Osaretin, M. W. Shields, J. A. M. Lorenzo, and W. J. Blackwell, "A compact 118-GHz radiometer antenna for the micro-sized microwave atmospheric satellite," *IEEE Antennas and Wireless Propagation Letters*, vol. 13, pp. 1533-1536, 2014.

[8] V. Kangas, S. D'Addio, G. Mason, M. Buckley, G. Tennant, and P. Campbell, "Microwave sounder instrument for MetOp second generation," in *13th Specialist Meeting on Microwave Radiometry and Remote Sensing of the Environment (MicroRad)*, Pasadena, CA, USA, pp. 232-235, 2014.

[9] R. Dey, R. Ram, S. Kulshrestha, V. K. Singh, and M. B. Mahajan, "Design and development of antenna system for millimeter-wave humidity sounder payload," in *IEEE Microwaves, Antennas, and Propagation Conference (MAP-CON)*, Ahmedabad, India, pp. 1-4, 2023.

[10] W. J. Blackwell, "Antenna development for microwave sounding CubeSats," in *IEEE International Symposium on Antennas and Propagation (APSURSI)*, Fajardo, PR, USA, pp. 1537-1538, 2016.

[11] R. Albers, A. Emrich, and A. Murk, "Antenna design for the arctic weather satellite micro-wave sounder," *IEEE Open Journal of Antennas and Propagation*, vol. 4, pp. 686-694, 2023.

[12] E. Kim, V. Leslie, J. Lyu, C. Smith, I. Osaretin, S. Abraham, M. Sammons, K. Anderson, J. Amato, J. Fuentes, M. Hernquist, M. Landrum, F. Rodriguez-Gutierrez, J. Kam, P. Cho, H. Yang, Q. Liu, and N. Sun, "Pre-launch performance of the Advanced Technology Microwave Sounder (ATMS) on the Joint Polar Satellite System-2 Satellite (JPSS-2)," in *IEEE International Geoscience and Remote Sensing Symposium*, Waikoloa, HI, USA, pp. 6353-6356, 2020.

[13] D. A. Houtz, W. Emery, D. Gu, K. Jacob, A. Murk, D. K. Walker, and R. J. Wylde, "Electromagnetic design and performance of a conical microwave blackbody target for radiometer calibration," *IEEE Transactions on Geoscience and Remote Sensing*, vol. 55, no. 8, pp. 4586-4596, Aug. 2017.

[14] K. Jacob, A. Schröder, L. von Werra, F. Reinhard, P. Raisin, and A. Murk, "Radiometric characterization of a water-based conical blackbody calibration target for millimeter-wave remote sensing," *IEEE Journal of Selected Topics in Applied Earth Observations and Remote Sensing*, vol. 12, no. 6, pp. 1688-1696, June 2019.

[15] L. Cheng, Y. Li, X. Zhang, L. Xia, Y. Yang, and P. Li, "A fast and accurate design method for the smooth-walled horn antenna with a high

Gaussian coupling efficiency," in *16th UK-Europe-China Workshop on Millimetre Waves and Terahertz Technologies (UCMMT)*, Guang-zhou, China, pp. 1-3, 2023.

[16] L. Cheng, F. Wu, Y. Zhou, D. Li, Y. Yang, and L. Jin, "Study on horn antenna with a high Gaussian coupling efficiency," in *CIE International Conference on Radar (Radar)*, Haikou, Hainan, China, pp. 1976-1979, 2021.

[17] B. Li, M. Jin, M. Bai, and Z. Li, "Quasi-optical antennas design in the standard measurement facility on the emissivity from microwave calibration targets," *Journal of Astronautic Metrology and Measurement*, vol. 38, no. 6, pp. 9-15, 2018.

[18] J. E. McKay, D. A. Robertson, P. J. Speirs, R. I. Hunter, R. J. Wylde, and G. M. Smith, "Compact corrugated feedhorns with high Gaussian coupling efficiency and -60 dB sidelobes," *IEEE Transactions on Antennas and Propagation*, vol. 64, no. 6, pp. 2518-2522, June 2016.

[19] F. Teng, J. Wan, and J. Liu, "Design of a 118 GHz corrugated horn based on the modal analysis," in *IEEE International Workshop on Electromagnetics: Applications and Student Innovation Competition (iWEM)*, Guangzhou, China, pp. 1-3, 2021.

[20] FEKO. Altair Engineering, Inc., Troy, MI, 2020.

Haoran Zhang received the B.Sc. degree from Beijing University of Chemical Technology (BUCT) in 2023, where he is now pursuing his master's degree. His research interest is the design of quasi-optical antennas.

Ming Jin received the B.Sc. and Ph.D. degrees from Beihang University (BUAA), Beijing, China, in 2007 and 2013, respectively. From 2007 to 2012, he was a research assistant in the Microwave Engineering Laboratory, Beihang University. From December 2010 to March 2011, he was a Visiting Scholar at Arizona State University. In 2019, he joined the College of Information Science and Technology, Beijing University of Chemical Technology (BUCT) as an associate professor. His research interests include microwave radiometer calibration techniques, quasi-optical beam propagation and computational electromagnetics.

Study on Partial Coating Approach for Reducing Cavity Backscattering

Cong-Bo Zhang, Xiao-Wei Huang, and Xin-Qing Sheng

Institute of Radio Frequency Technology and Software
School of Integrated Circuits and Electronics, Beijing Institute of Technology, Beijing 100081, China
3120185390@bit.edu.cn, xwhuang@bit.edu.cn, xsheng@bit.edu.cn

***Abstract* –** Cavities are strong scattering parts for aircrafts, while coating the interior surface of cavities is a general approach for reducing cavity backscattering. In this paper, the discontinuous Galerkin (DG) method based on the self-dual integral equation (SDIE) is employed to efficiently simulate scattering from partially coated cavities. The distance sparse preconditioner (DSP) is applied to DG-SDIE for speeding up convergence instead of the conventional block-diagonal preconditioner (BDP). An efficient partial coating scheme is presented. The numerical results of straight cavity, S-shaped cavity and complex aircraft cavity demonstrate our coating scheme can achieve similar effect of reducing backscattering by using smaller coated interior surface regions. Useful conclusions about partially coating the cavity are summarized.

***Index Terms* –** Coated cavity, discontinuous Galerkin (DG) method, distance sparse preconditioner (DSP), self-dual integral equation (SDIE).

I. INTRODUCTION

Scattering from cavity structures often contributes significantly to the overall electromagnetic (EM) scattering from aircraft. A major way to reduce EM scattering from these cavities is to coat their interior surface with EM absorbing materials. How to efficiently coat the cavity becomes an attractive problem.

Method of moments (MoM) is a powerful tool for the EM scattering problem [1–3]. The thin coating surface is usually approximated by the impedance boundary condition (IBC) [4]. Formulations of MoM based on the surface integral equation and IBC were developed in [5–8]. However, these early formulations suffered from drawbacks of an ill-conditioned matrix. A robust and efficient self-dual integral equation (SDIE) was developed for scattering from coated objects [9]. A more efficient formulation was recently developed by employing the combined field integral equation (CFIE) and IBC, shortened to C-SDIE [10]. The discontinuous Galerkin (DG) method was recently applied to C-SDIE (DG-C-SDIE) to further improve efficiency and flexibility for simulating scattering from non-uniform or partially coated cavities [11–14].

In this paper, DG-C-SDIE is employed to study scattering from partially coated cavities. A more efficient distance sparse preconditioner (DSP) is applied to DG-C-SDIE to replace the conventional block-diagonal preconditioner (BDP) used in [10]. Furthermore, a partial coating scheme is presented for more efficient coating. The numerical results of scattering from coated rectangular cavity, S-shaped curved cavity and realistic aircraft cavity demonstrate that our coating scheme can achieve the similar effects of reducing backscattering with a smaller coated surface region. Some useful results for partially coating a cavity to reduce backscattering are obtained and shown in section IV.

II. FORMULATION

Consider a coated cavity immersed in free space with permittivity ε_0 and permeability μ_0. The cavity is illuminated by an incident plane wave $(\boldsymbol{E}^{inc}, \boldsymbol{H}^{inc})$. Electric current $\boldsymbol{J}$ and magnetic current $\boldsymbol{M}$ on the cavity surface S can be formulated by the CFIE as:

$$C(z_0\boldsymbol{J}) - \frac{1}{2}z_0\boldsymbol{J} + \widehat{\boldsymbol{n}} \times C(\boldsymbol{M}) - \frac{1}{2}\widehat{\boldsymbol{n}} \times \boldsymbol{M} = -\boldsymbol{e}^{inc} - \boldsymbol{j}^{inc}, \quad (1)$$

where $\widehat{\boldsymbol{n}}$ denotes the outward normal vector of the cavity surface S, $z_0 = \sqrt{\varepsilon_0/\mu_0}$, $\boldsymbol{e}^{inc} = \widehat{\boldsymbol{n}} \times \boldsymbol{E}^{inc} \times \widehat{\boldsymbol{n}}$, and $\boldsymbol{j}^{inc} = z_0\widehat{\boldsymbol{n}} \times \boldsymbol{H}^{inc}$. Operator $C = L + K$ and operator L and K are defined as:

$$L(\boldsymbol{X}) = -jk_0 \int_S \left(I + \frac{\nabla\nabla}{k_0^2}\right) G(\boldsymbol{r}, \boldsymbol{r}') \cdot \boldsymbol{X}(\boldsymbol{r}')dS', \quad (2)$$

$$K(\boldsymbol{X}) = P.V. \int_S \nabla G(\boldsymbol{r}, \boldsymbol{r}') \times \boldsymbol{X}(\boldsymbol{r}')dS', \quad (3)$$

where $G(\boldsymbol{r}, \boldsymbol{r}') = e^{-jk_0|r-r'|}/4\pi|\boldsymbol{r}\text{-}\boldsymbol{r}'|$ denotes the free-space Green's function with wavenumber k_0 and P.V. stands for the Cauchy principal value integration.

On the other hand, IBC can give the following relation between $\boldsymbol{J}$ and $\boldsymbol{M}$ as:

$$z_s z_0 \boldsymbol{J} = \widehat{\boldsymbol{n}} \times \boldsymbol{M}. \quad (4)$$

Submitted On: October 1, 2023
Accepted On: September 16, 2024

https://doi.org/10.13052/2025.ACES.J.400208

$$\begin{bmatrix} C-\frac{1}{2}-\sqrt{z_s} & \hat{\boldsymbol{n}}\times C\left(\sqrt{z_s}\right)-\frac{\sqrt{z_s}}{2}\hat{\boldsymbol{n}}\times I+\hat{\boldsymbol{n}}\times I \\ -\hat{\boldsymbol{n}}\times C+\frac{1}{2}\hat{\boldsymbol{n}}\times I-\sqrt{z_s}\hat{\boldsymbol{n}}\times I & C\left(\sqrt{z_s}\right)-\frac{\sqrt{z_s}}{2}-1 \end{bmatrix}\begin{bmatrix} \widetilde{\boldsymbol{J}} \\ \widetilde{\boldsymbol{M}} \end{bmatrix}=\begin{bmatrix} -\boldsymbol{e}^{inc}-\boldsymbol{j}^{inc} \\ \left(-\boldsymbol{e}^{inc}-\boldsymbol{j}^{inc}\right)\times\hat{\boldsymbol{n}} \end{bmatrix}. \tag{5}$$

It should be noticed that z_s is the normalized surface impedance of the cavity. Combining equations (1) and (4) and replacing $\boldsymbol{J}$ and $\boldsymbol{M}$ with $\widetilde{\boldsymbol{J}}=z_0\boldsymbol{J}$ and $\widetilde{\boldsymbol{M}}=\boldsymbol{M}/\sqrt{z_s}$ yields the C-SDIE equation (5).

According to the DG method, $\boldsymbol{J}$ and $\boldsymbol{M}$ are expanded with the RWG basis or half RWG basis $\boldsymbol{g}$. The electric or magnetic current continuity between nonconformal meshes is inherently guaranteed by translating the term in the integral equation involving operator L into the following four terms [14]:

$$\begin{aligned}\int_S \boldsymbol{g}_m\cdot L(\boldsymbol{g}_n)\,dS &= -jk_0\int_S\int_{S'}\boldsymbol{g}_m\cdot\boldsymbol{g}_n G dS' dS \\ &+\frac{j}{k_0}\int_S\nabla\cdot\boldsymbol{g}_m\int_{S'}\nabla'\cdot\boldsymbol{g}_n G dS' dS-\frac{j}{k_0}\int_S\nabla\cdot\boldsymbol{g}_m\int_{C'}\hat{\boldsymbol{t}}_n \\ &\cdot\boldsymbol{g}_n G dC' dS-\frac{j}{k_0}\int_C\hat{\boldsymbol{t}}_m\cdot\boldsymbol{g}_m\int_{S'}\nabla'\cdot\boldsymbol{g}_n G dS' dC,\end{aligned} \tag{6}$$

where m, n are the number of the edges, $\boldsymbol{g}$ denotes either RWG basis or half RWG basis, and $\hat{\boldsymbol{t}}$ denotes the unit normal vector of the boundary edges.

It is found that the BDP used in [10] does not work well for a partially coated cavity. We here apply a simple and efficient preconditioner DSP to DG-C-SDIE. The entries of DSP matrix are:

$$P_{ij}=\begin{cases} M_{ij} & \left|\boldsymbol{r}_i-\boldsymbol{r}_j\right|\le 0.3\lambda_0 \\ 0 & elsewhere \end{cases}, \tag{7}$$

where r_i and r_j represent the location of the testing and bases elements and λ_0 is the free space wavelength.

III. NUMERICAL RESULTS

In the following numerical experiments, the multilevel fast multipole algorithm (MLFMA) [15] is applied to reduce CPU time and memory requirement.

A. Coating scheme

To efficiently coat the cavities, we first should select a suitable normalized surface impedance z_s of the coating. According to [4], when the EM wave is vertically incident on the coating, the surface impedance z_s of the coating can be equivalent as:

$$z_s=\sqrt{\frac{\varepsilon_r}{\mu_r}}\tanh(jk_0 d\sqrt{\varepsilon_r\mu_r}), \tag{8}$$

where d is the thickness of the coating, ε_r and μ_r are relative permittivity and relative permeability respectively, and k_0 is the wave number in free space. The impedance boundary condition typically assumes a small tangential electric field and, therefore, the equivalent impedance at vertical incidence is generally regarded as a boundary approximation. The effectiveness of the impedance boundary condition has been extensively studied [14, 16]. To make a preliminary assessment of the wave-absorbing performance of coatings with different thicknesses, the following reflection coefficient formula for a normally incident semi-infinite space is commonly used for estimation:

$$R=\left|\frac{1-z_s}{1+z_s}\right|. \tag{9}$$

In this paper, a real EM absorbing material with relative permittivity of (18.4, -1.09j) and relative permeability of (1.6, -1.67j) is used. The relation between reflectivity R and thickness of the coat d is shown in Fig. 1, where λ is the wavelength of absorbing material. The thickness of 0.117λ, 0.17λ and 0.21λ are chosen respectively as three coating cases (I, II, III) of the absorbing capacity from weak to strong. The normalized surface impedances are equivalent as (0.2819, 0.175j), (0.4936, 0.1302j) and (0.5927, -0.0396j), respectively.

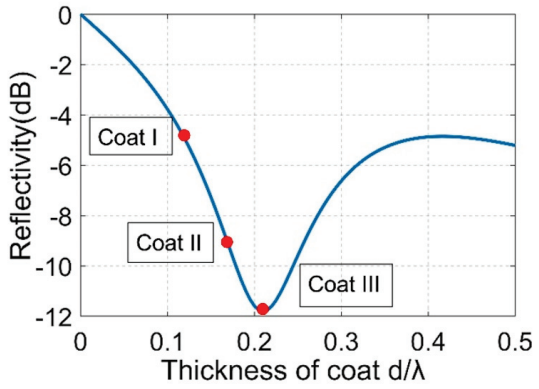

Fig. 1. Relationship between reflectivity and the thickness of a coating with relative permittivity of (18.4, -1.09j) and relative permeability of (1.6, -1.67j), where λ is the wavelength in absorbing material.

Our coating scheme is as follows. When the frequency of the EM wave is higher than the cutoff frequency of the cavity dominant mode, the EM wave can enter the cavity. We coat the cavity interior surface area directly illuminated by the EM wave incident in all concerned angles. To further reduce the coated region, we can neglect the part which is illuminated by the EM wave incident in a small angle range and coat the part which is illuminated by the EM wave incident from a large incident angle range.

When the frequency of the EM wave is lower than the cutoff frequency of the cavity, the EM wave cannot enter the cavity. Therefore, we coat the external surface of the cavity.

B. Performance of DSP preconditioner

The numerical example is a partially coated rectangular cavity whose dimension is $1m\times 1m\times 2m$ and

Table 1: Comparison of numerical performance of NoP, BDP, DSP for the cavity in Fig. 2, where the degree of freedom is 5709

	Memory for PreC (MB)	CPU Time for PreC (s)	Iteration Number	Iteration Time (s)	Total Time (s)
NoP	—	—	76	23.14	23.14
BDP	3927	1468.89	21	10.85	1479.74
DSP	277	6.62	16	5.79	12.41

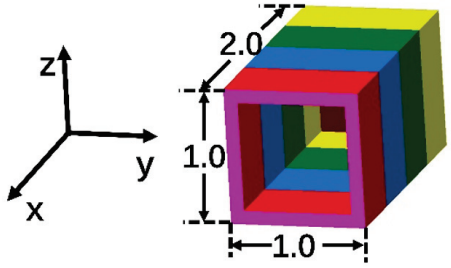

Fig. 2. Rectangle cavity with coated interior surface (impedance $z_s = 0.2819 + 0.175j$) and perfect electric conducting (PEC) external surface.

thickness is 0.1 m, shown in Fig. 2. The interior surface is an IBC boundary with impedance $z_s = 0.2819 + 0.175j$ and the external surface is a perfect electric conducting (PEC) material. The cavity is illuminated by a plane wave of 300 MHz, propagating in the x-direction with the electric field polarized in the z-direction. The cavity is divided into 11 subdomains to speed up the inverse of BDP preconditioner. Each subdomain is discretized independently with mesh size $\lambda/10$. The degree of freedom (DoF) of the cavity is 5709, with 3366 DoFs for the external cavity surface and 2343 DoFs for the interior cavity surface. The numerical performance of no preconditioner (NoP), BDP and DSP are shown in Table 1. The bistatic RCS and iteration convergence history are shown

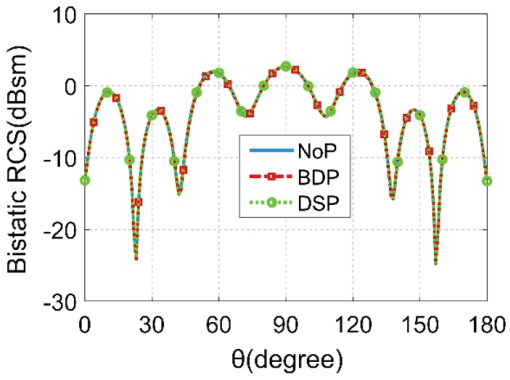

(a)

Fig. 3. *Continued.*

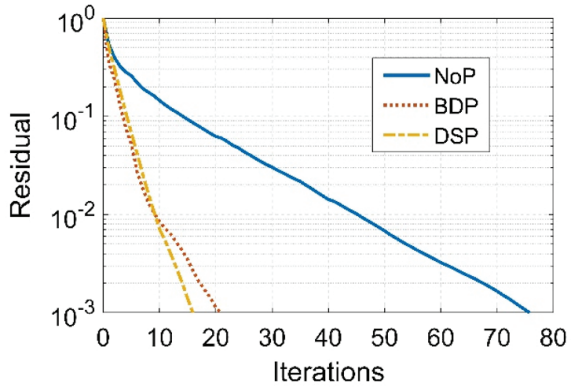

(b)

Fig. 3. (a) Bistatic VV-polarized RCS and (b) iteration convergence history for the cavity in Fig. 2, applying different preconditioners.

in Fig. 3. From Table 1 and Fig. 3, we can observe that, compared with BDP, DSP has a little faster convergence speed but saves considerable time and memory for constructing the preconditioner matrix. Obviously, DSP is more efficient when dealing with the coated cavity problem with larger DoFs.

C. Coated straight cavity

The EM scattering properties of a partially coated straight cavity are first investigated. Let us consider a rectangular cavity with an interior surface of $1m \times 4m \times 8m$ and a thickness of 0.1 m, as shown in Fig. 4. The surface impedance of coating is chosen as (0.2819, 0.175j). The RCS calculation angle is 60∼90 degrees in the θ-direction and $\varphi = 0$.

For a straight cavity, the entire cavity interior surface can be illuminated directly by the EM wave from our incident angle range. According to the surface area illuminated by EM waves in different incident angular

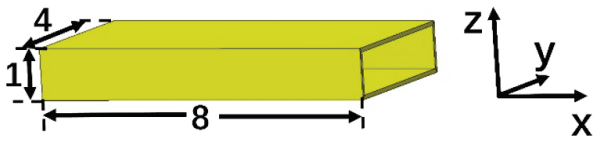

Fig. 4. Parameters of the rectangular cavity (unit: meter).

ranges, the interior surface of the cavity can be divided into four surface regions, as shown in Fig. 5 (a). The blue region is illuminated by an incident angle range of 60∼90 degrees, the azure region by an incident angle range of 70∼90 degrees, the green area by an incident angle range of 80∼90 degrees and the yellow area by a much smaller incident angle range. For the straight cavity, coating the directly illuminated area is equivalent to coating the entire interior surface. According to our coating approach, three schemes are presented to further reduce the coated area, as shown in Fig. 5 (b). Scheme I coats the three regions of the blue, azure and green area; Scheme II coats the two regions of the blue and azure area; Scheme III only coats the blue region. We calculate the monostatic VV-polarization RCS of the PEC cavity, the cavity in which the total interior surface is coated (total coating), and the cavity coated by Scheme I, II and III at frequency $f = 600$ MHz.

Let us take the total coating as an example. The DoF of the cavity is 245709 with 128406 DoFs for the external cavity surface and 117303 DoFs for the interior cavity surface. The results are shown in Fig. 6. From Fig. 6, we see Scheme I has similar RCS reduction with the total coating. Scheme II also has comparable RCS reduction with the total coating, except for a little higher RCS at 80∼90 degrees. Scheme III has similar RCS reduction with total coating at the angle range of 60∼75 degrees,

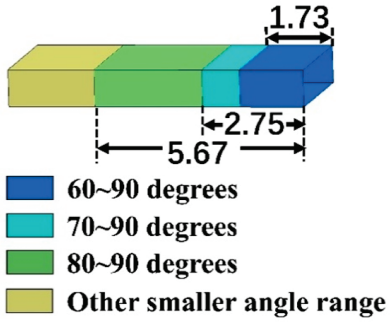

(a)

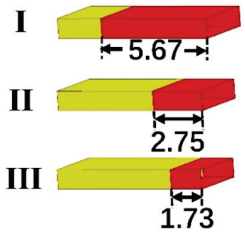

(b)

Fig. 5. The four regions illuminated by the EM wave from different angular ranges in the θ direction and (b) the three partial coating schemes (red area is coated and the unit is meter).

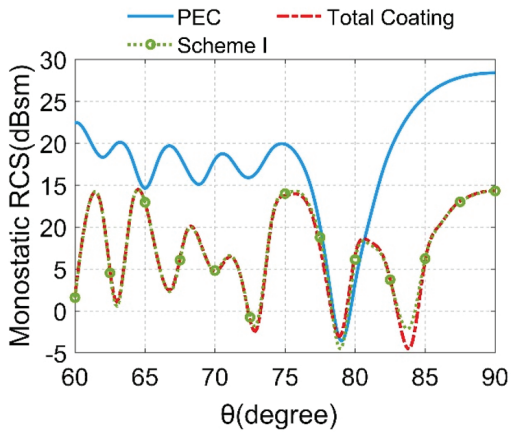

(a)

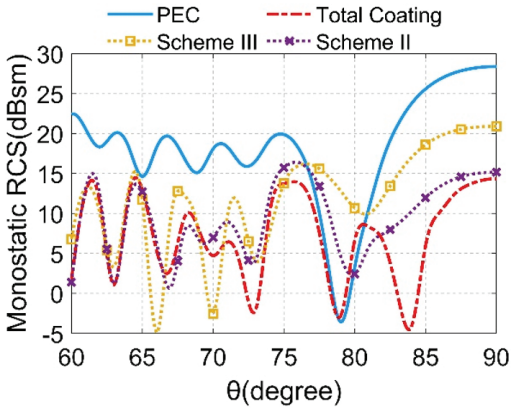

(b)

Fig. 6. (a) Monostatic VV-polarization RCS of PEC cavity in which the total interior surface is coated and (b) cavity coated by three schemes in Fig. 5 (b), at a frequency of 600 MHz.

but less RCS reduction at the angle range of 75∼90 degrees, as we expected.

Next, we calculate the scattering from the above coated rectangular cavity at frequency of 15 MHz lower than the cavity dominant mode cutoff frequency of 37.5 MHz. The monostatic RCS of this coated cavity are shown in Fig. 7. As we expect, coating the interior surface of cavity cannot reduce RCS at all. For this case, coating the external surface of the cavity is the only way to reduce RCS.

D. Coated S-shaped cavity

We further investigate the EM scattering properties of the coated S-shaped cavity, which is widely used in the air inlet of stealth aircraft. As shown in Fig. 8, the model is a double S-shaped cavity with thickness 0.1 m and the specific parameters of the interior surface are as follows. The two S-shaped regions are 4.5 and 3.5 m long and offset distances in bending direction are 1.4 and 0.6

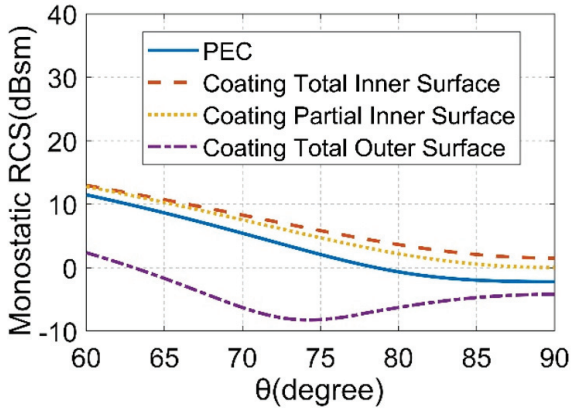

Fig. 7. Monostatic VV-polarization RCS of a PEC cavity in which the total inner and partial inner surface is coated, and a cavity in which the total outer surface is coated, at frequency of 15 MHz.

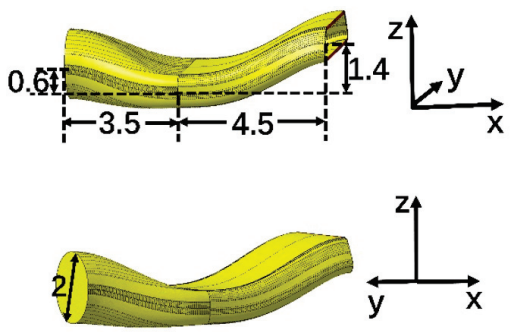

Fig. 8. Parameters of double-S shaped cavity (unit: meter).

m long; The bottom is a round surface with radius of 2 m while the opening is trapezoid with a median of 3.75 m and height of 0.94 m. The surface impedance of the coat is (0.2819, 0.175j). The RCS calculation angle is 60∼120 degrees in the θ direction and $\varphi = 0$.

Based on the analysis of a coated rectangular cavity, the interior surface of the S-shaped cavity can be divided into different regions as shown in Fig. 9 (a). The yellow region is not illuminated directly by the EM wave; the dark green and light green regions are illuminated by incident angles of 60∼82 degrees; the red, blue, pink and purple regions are illuminated by an incident angle of 82∼90, 82∼100, 82∼110 and 82∼120 degrees; the orange region by a much smaller incident angle range. According to our coating approach, we have the following coating schemes. Scheme I only coats the region illuminated directly by the EM wave. Since the asymmetric structure of the S-shaped cavity makes the EM wave incident from large angles (82∼120 degrees) illuminate a small region on the upper interior surface and the EM

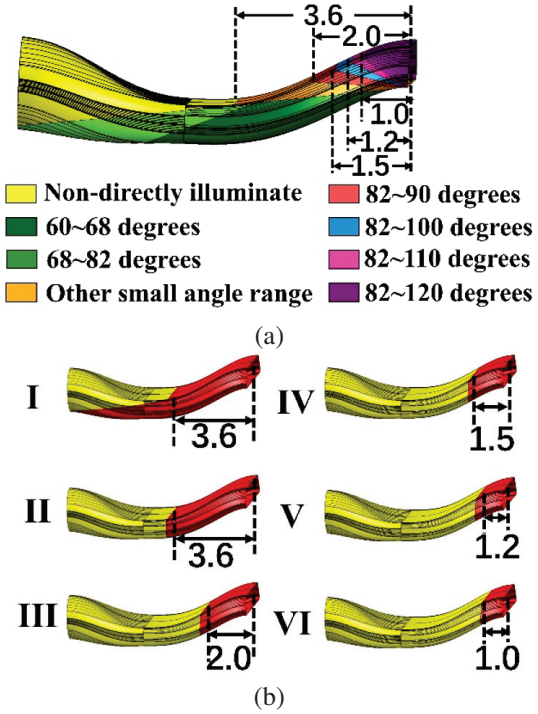

Fig. 9. (a) Eight regions illuminated by an EM wave from different angular ranges in the θ direction and (b) six partial coating schemes (red area is coated and the unit is meter).

wave incident from small angles (60∼82 degrees) illuminates a large region on the lower interior surface, Scheme II neglects the region on the lower surface and only coats the region corresponding to 82∼120 degrees. Based on Scheme II, we further neglect the orange, red, blue and pink area in turn, corresponding to Schemes III, IV, V and VI, respectively. These schemes are shown in Fig. 9 (b). The monostatic VV-polarization RCS from the PEC cavity, the total coating and the cavity coated by the above-mentioned schemes at 600 MHz are calculated. Taking the total coating as an example, the DoF of the cavity is 200893, with 104653 DoFs for the external cavity surface, and 96240 DoFs for the interior cavity surface. We here only show the monostatic VV-polarization.

RCS of Scheme I and III in Fig. 10 and use the RCS from the PEC cavity and the total coating cavity as a comparison. It can be seen that Scheme I has nearly the same RCS reduction as total coating. Scheme III also has comparable RCS reduction as total coating, except for a little higher RCS at 65∼82 degrees, as we expected. To better demonstrate the effect of the coated area saving for reducing RCS, we defined the average reduction of RCS as:

$$\overline{RCS_{reduce}} = \left(\sum_{i=1}^{N_{obs}} \left(RCS^{i}_{PEC} - RCS^{i}_{IBC} \right) \right) \Big/ N_{obs}, \quad (10)$$

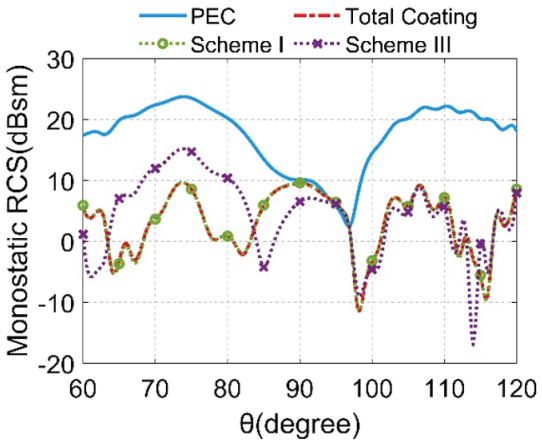

Fig. 10. Monostatic VV-polarization RCS of PEC cavity in which the total interior surface is coated, and cavity coated by Scheme I and III in Fig. 9 (b), at a frequency of 600 MHz.

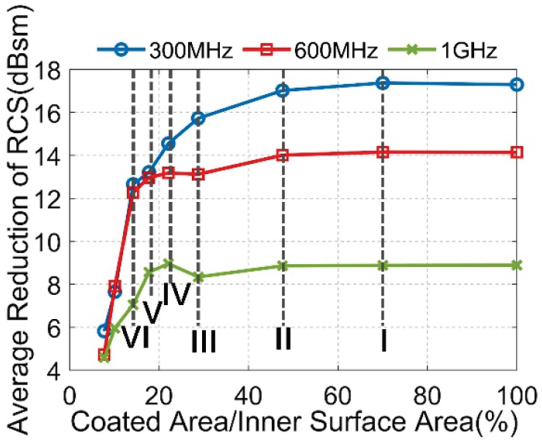

Fig. 11. Relationship between average reduction of the monostatic VV-polarization RCS and coated area ratio. Frequency is altered from 300 MHz to 1 GHz.

where N_{obs} denotes the number of observation angles and 121 is used in this example, RCS^i_{PEC} is the RCS of PEC cavity and RCS^i_{IBC} is the RCS of the coated cavity. The relationship between the coated area ratio and the average reduction of RCS is shown as a red line in Fig. 11 and the points corresponding to Scheme I∼VI is marked. Clearly, coating the directly illuminated area (Scheme I) guarantees maximum (reliability for) RCS decrease and saves about 30% coating area while neglecting the area illuminated by a few angles (Scheme II∼VI) saves about 50∼85% area respectively and maintains enough RCS reduction.

E. Feasibility for different frequency

In this part, the feasibility of our partial coating scheme for different frequencies is investigated. We employ the same impedance (0.2819, 0.175j), and set the different frequencies as 300 MHz, 600 MHz and 1 GHz; other parameters are the same as those in section IIID. The relationship between average reduction of the monostatic VV-polarization RCS and the coated area ratio for different coatings are shown in Fig. 11. As we see, the coated region directly illuminated (Scheme I) in the whole incident angle range has almost the same RCS reduction as the fully coated cavity for all frequencies. Moreover, we see Scheme II and III, which do not coat the interior surface illuminated by a small incident angle range, can also reduce enough RCS. All these demonstrate the applicability of our coating scheme.

F. Complex and large cavity with partial coating

Finally, a complex and large cavity with partial coating is presented to show the performance of our partial coating scheme. We consider a real inlet of a stealth aircraft, a three S-shaped cavity, whose opening is a parallelogram of 1157*966 mm and bottom is a circle with radius of 0.5 m, as shown in Fig. 12. This cavity is 97λ in length. The surface impedance of the coating is (0.4936, 0.1302j). We calculate the monostatic RCS in the incident angle range of 60∼120 degrees in the θ-direction and 0 degrees in the φ-direction at a frequency of 4 GHz.

According to our partial coating scheme, a specific coating scheme is as follows. Coating the area of cavity directly illuminated in an incident angle range from 60 to 120 degrees, designated by the red area shown in Fig. 13. This coating scheme can save 11.1% coated area compared to total coating. The monostatic VV-polarization RCS of the PEC cavity, the total coating cavity and the

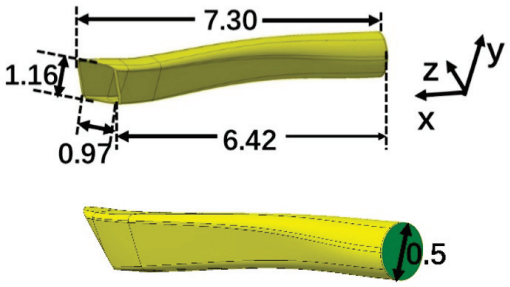

Fig. 12. Parameters of a realistic air inlet (unit: meter).

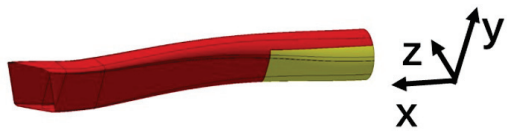

Fig. 13. Partial coating scheme for cavity in Fig. 12 (red area is coated).

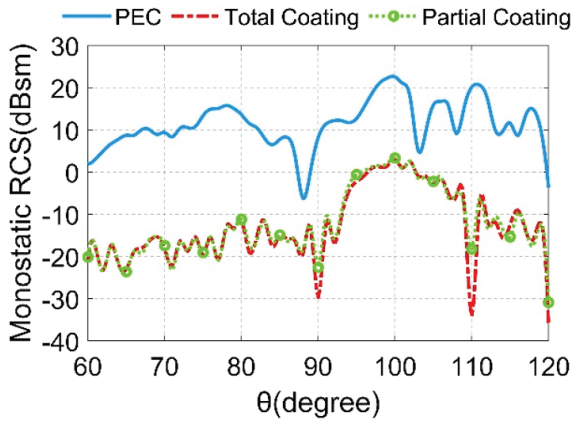

Fig. 14. Monostatic VV-polarization RCS of PEC cavity in which the total interior surface is coated, and cavity partially coated by the scheme in Fig. 13, at a frequency of 4 GHz.

cavity coated by our scheme are calculated. Take the total coating as an example. DoF of the cavity is 2828576 with 1464133 DoFs for the external cavity surface, and 1364443 DoFs for the interior cavity surface. RCS are shown in Fig. 14, and we can clearly see that our coating scheme can significantly reduce RCS and achieve almost the same results as the total coating.

IV. CONCLUSION

Scattering from partially coated cavities is studied efficiently and accurately by the improved DG-C-SDIE. The following useful conclusions can be obtained from the numerical experiments:

1. Coating the cavity interior surface region directly illuminated by the EM wave incident in whole angles can efficiently reduce backscattering and obtain almost the same RCS reduction as the total coating cavity.
2. The cavity interior surface illuminated by the EM wave incident in a small angle range can be further neglected and is not coated to further reduce the coated area with a little loss of RCS reduction.
3. For a working frequency lower than the cut-off frequency of the cavity, coating the interior cavity surface cannot reduce RCS. Instead, coating the external cavity surface is the only way to reduce the backscattering of the cavity.

ACKNOWLEDGMENT

This work was supported in part by the China National Postdoctoral Program for Innovative Talents under Grant BX20220376 and in part by the China Postdoctoral Science Foundation under Grant 2022M72041.

REFERENCES

[1] J. Hu, R. Zhao, M. Tian, H. Zhao, M. Jiang, X. Wei, and Z. P. Nie, "Domain decomposition method based on integral equation for solution of scattering from very thin, conducting cavity," *IEEE Trans. Antennas Propagat.*, vol. 62, no. 10, pp. 5344-5348, Oct. 2014.

[2] Z. Peng, K.-H. Lim, and J.-F. Lee, "A boundary integral equation domain decomposition method for electromagnetic scattering from large and deep cavities," *J. Comput. Phys.*, vol. 280, pp. 626-642, Jan. 2015.

[3] C.-B. Zhang and X.-Q. Sheng, "An efficient discontinuous Galerkin method for cavity design," *IEEE Antennas Wireless Propagat. Lett.*, vol. 20, no. 2, pp. 199-203, Feb. 2021.

[4] T. B. A. Senior, "Approximate boundary conditions," *IEEE Trans. Antennas Propagat.*, vol. 29, no. 5, pp. 826-829, Sep. 1981.

[5] K. M. Mitzner, "An integral equation approach to scattering from a body of finite conductivity," *Radio Sci.*, vol. 2, no. 12, pp. 1459-1470, Dec. 1967.

[6] J. Rogers, "Moment-method scattering solutions to impedance boundary condition integral equations," *Proc. Antennas Propagat. Soc. Int. Symp.*, vol. 22, pp. 347-350, June 1984.

[7] A. W. Glisson, "Electromagnetic scattering by arbitrarily shaped surfaces with impedance boundary conditions," *Radio Sci.*, vol. 27, no. 6, pp. 935-943, Jan. 1992.

[8] A. Bendali, M. B. Fares, and J. Gay, "A boundary-element solution of the Leontovitch problem," *IEEE Trans. Antennas Propagat.*, vol. 47, no. 10, pp. 1597-1605, Oct. 1999.

[9] S. Yan and J.-M. Jin, "Self-dual integral equations for electromagnetic scattering from IBC objects," *IEEE Trans. Antennas Propagat.*, vol. 61, no. 11, pp. 5533-5546, Nov. 2013.

[10] H.-W. Gao, M.-L. Yang, and X.-Q. Sheng, "A new SDIE based on CFIE for electromagnetic scattering from IBC objects," *IEEE Trans. Antennas Propagat.*, vol. 68, no. 1, pp. 388-399, Jan. 2020.

[11] Z. Peng, K.-H. Lim, and J.-F. Lee, "A discontinuous Galerkin surface integral equation method for electromagnetic wave scattering from nonpenetrable targets," *IEEE Trans. Antennas Propagat.*, vol. 61, no. 7, pp. 3617-3628, July 2013.

[12] B.-B. Kong and X.-Q. Sheng, "A discontinuous Galerkin surface integral equation method for scattering from multiscale homogeneous objects," *IEEE Trans. Antennas Propagat.*, vol. 66, no. 4, pp. 1937-1946, Apr. 2018.

[13] X.-W. Huang and X.-Q. Sheng, "A discontinuous Galerkin self-dual integral equation method for scattering from IBC objects," *IEEE Trans. Antennas Propagat.*, vol. 67, no. 7, pp. 4708-4717, July 2019.

[14] X.-W. Huang, M.-L. Yang, and X.-Q. Sheng, "A simplified discontinuous Galerkin self-dual integral equation formulation for electromagnetic scattering from extremely large IBC objects," *IEEE Trans. Antennas Propagat.*, vol. 70, no. 5, pp. 3575-3586, May 2022.

[15] J. M. Song, C.-C. Lu, and W. C. Chew, "Multilevel fast multipole algorithm for electromagnetic scattering by large complex objects," *IEEE Trans. Antennas Propag.*, vol. 45, no. 10, pp. 1488-1493, Oct. 1997.

[16] D.-S. Wang, "Limits and validity of the impedance boundary condition on penetrable surfaces," *IEEE Trans. Antennas Propagat.*, vol. 35, no. 4, pp. 453-457, Apr. 1987.

Cong-Bo Zhang received the B.S. degrees in physics from the Beijing Institute of Technology (BIT), Beijing, China, in 2017. He is currently pursuing the Ph.D. degree in the Institute of Radio Frequency Technology and Software, School of Integrated Circuits and Electronics, BIT. His current research interests include the computational electromagnetics, domain decomposition methods, and EM scattering from complex cavity. Zhang was a recipient of the Student Modeling Contest 2nd Prize at the 2021 International Applied Computational Electromagnetics Society (ACES-China) Symposium.

Xiao-Wei Huang received the B.S. and Ph.D. degrees in electronic science and technology from the Beijing Institute of Technology (BIT), Beijing, China, in 2017 and 2022, respectively. Since 2022, he has been a *TeLi* Post-Doctoral Researcher with the Institute of Radio Frequency Technology and Software, School of Integrated Circuits and Electronics, BIT. His current research interests include computational electromagnetics, EM wave-plasma interactions, domain decomposition methods, and fast direct solvers for integral equations. Huang was a recipient of the Best Student Paper Award (1st place) at the 2018 International Applied Computational Electromagnetics Society (ACES-China) Symposium, and a recipient of the 2022 China National Postdoctoral Program for Innovative Talents.

Xin-Qing Sheng is a Chair Professor of the Beijing Institute of Technology. Sheng has authored and coauthored over 180 papers in referred journals, and 10 books. Sheng has authored the software of *SINOCOM* for electromagnetic simulation. His research interests include computational electromagnetics, scattering and antenna analysis, electromagnetic compatibility, microwave imaging. Sheng is a recipient of the 2001 One Hundred Talents Program awarded by the Chinese Academy of Sciences, the 2004 Cheung Kong Scholar Program awarded by the Ministry of Education of China, and the first recipient of the first prize of Beijing Science and Technology Awards in 2009.

A Note on Matrix Decomposition for Synthetic Basis Functions Method in the Analysis of Periodic Structures

Yanlin Xu[1], Ning Hu[2], Chenxi Liu[1], Hao Ding[1], and Jun Li[3]

[1]College of Electronic Science and Technology
National University of Defense Technology, Changsha 410073, China
13298656824@163.com, liuchenxi09@nudt.edu.cn, dinghao20a@nudt.edu.cn

[2]Information Engineering University
Zhengzhou 450001, China
1141832906@qq.com

[3]The Second Representative Office of Changsha Area
Changsha 410011, China
271069796@qq.com

Abstract – The synthetic basis functions method (SBFM) is discussed in this work and orthogonal triangle decomposition (QR decomposition) is adopted to extract independent items from solution space in the construction of synthetic functions. Just like singular value decomposition (SVD), accuracy of SBFM+QR improves with the growth of the number of synthetic functions. However, there is an interesting phenomenon for SBFM+QR: only one synthetic function is enough to get the same level of accuracy with method of moments (MoM) when a single body is concerned. Moreover, this feature can be further extended to periodic arrays. In other words, for periodic arrays, one synthetic function is enough to get high accuracy if SBFM+QR is adopted. This is meaningful for large-scale periodic arrays and may lead to benefits such as decreasing memory cost and improving efficiency.

Index Terms – Matrix decomposition, method of moments, periodic structures, surface integral equation, synthetic functions.

I. INTRODUCTION

Fast and accurate analysis of large-scale periodic arrays is an appealing and challenging task in computational electromagnetics. Method of moments (MoM) is a classical numerical approach well known for high accuracy. However, traditional MoM is hardly applied in the analysis of large-scale problems due to the restrictions on computational complexity and memory cost. To make MoM suitable for large-scale problems, many approaches have been proposed in the past decades [1–10]. The synthetic basis functions method (SBFM) is of special interest [11–20].

In contrast to traditional MoM, synthetic functions (SFs) are adopted in SBFM to discretize unknown vectors and to make the Galerkin test yield a high compressed matrix equation. Thus, the memory cost of SBFM will be decreased sharply. This makes it possible to analyze large-scale problems on a single PC. Similar approaches such as the sub-entire-domain (SED) basis functions method [21] and the characteristic basis functions method (CBFM) [22, 23] can be found in related literature and we are not going to introduce them in detail for the sake of brevity.

SBFM was initially presented by Matekovits et al. in 2001 in the analysis of array antennas [11]. A systematic work on SBFM was published in 2007 by Matekovits et al. which perfected the theory of SBFM [12]. Thereafter, SBFM concerned many scholars and a series of improved works were presented [13–20]. In SBFM, the construction of SFs is a core problem. Initially, Matekovits et al. defined SFs as linear combinations of a series of low order basis functions. Then, the solution space of SFs can be obtained by solving the responses of targets to excitations. Finally, singular value decomposition (SVD) can be implemented to extract independent items from the solution space which yields the expansion coefficient matrix of SFs.

In this paper, emphasis is on the matrix decomposition and orthogonal triangle decomposition (QR decomposition) is used to extract independent items from the solution space. From the results we find that, in general, accuracy of SBFM+QR improves with the growth of the number of SFs and this is coincident with the case of SBFM+SVD. We also found an interesting phenomenon: if the target is a single body with one natural excitation,

Submitted On: June 9, 2023
Accepted On: September 16, 2024

https://doi.org/10.13052/2025.ACES.J.400209

one SF is enough for SBFM+QR to get the same level of accuracy with traditional MoM. Then, based on concrete theoretical analysis, we give an explanation of the phenomenon. This feature can be extended from a single body to periodic arrays at the expense of slightly lowering accuracy. Notably, compared to SBFM+SVD, if there is one natural excitation, SBFM+QR can get a high level of accuracy with only one SF. Finally, a 10×10 circular microstrip patch antenna array is analyzed to validate effectiveness of the conclusion.

II. THEORY AND PHENOMENON

As SBFM is an improved approach of MoM, we will begin with the theory of MoM. Usually, the electric field integral equation (EFIE) can be written as:

$$\hat{n} \times L(J) = \hat{n} \times E_{\text{inc}}, \tag{1}$$

where L is the integral operator and defined as:

$$L(X) = \mathrm{j}\omega\mu \int_S [X + \frac{1}{k^2}\nabla(\nabla \cdot X)]g\mathrm{d}S. \tag{2}$$

To solve EFIE using MoM, a series of basic functions (e.g. RWG functions) are used to discretize the unknown vector $\boldsymbol{J}$ and to make the Galerkin test. Then, equation (1) can be transformed into a linear scalar matrix equation:

$$ZI = V, \tag{3}$$

where Z is impedance matrix, V is exciting matrix, and I is the current coefficients of RWG functions.

Unlike MoM, SFs are used, in SBFM, to discretize the unknown vector $\boldsymbol{J}$ and to make the Galerkin test. Then, equation (1) can be transformed into a compressed matrix equation [24]:

$$\begin{cases} W_{\text{SBF}}Y = G_{\text{SBF}} \\ W_{\text{SBF}} = P^{\text{H}}ZP \\ G_{\text{SBF}} = P^{\text{H}}V \end{cases}, \tag{4}$$

where $\boldsymbol{P}$ and Y are expansion coefficients matrix and current coefficients matrix of SFs, respectively, and Z and V are impedance matrix and exciting matrix of MoM.

Equation (4) indicates that the impedance matrix W_{SBF} and exciting matrix G_{SBF} of SBFM can be found on the basis of Z and V as long as the expansion coefficients matrix $\boldsymbol{P}$ of SFs is obtained. In other words, the core of SBFM is the calculation of SFs' expansion coefficients matrix. Here, we take a single body for demonstration.

For a specific body, assume the number of SFs and RWG functions defined on it are M and N, respectively. Usually, $M << N$. Then, SFs can be written as the linear combinations of RWG functions:

$$\begin{bmatrix} F_1 \\ F_2 \\ \cdots \\ F_M \end{bmatrix} = \begin{bmatrix} p_{11} & p_{12} & \cdots & p_{1N} \\ p_{21} & p_{22} & \cdots & p_{2N} \\ \cdots & & \cdots & \cdots \\ p_{m1} & p_{m2} & \cdots & p_{mN} \end{bmatrix} \begin{bmatrix} f_1 \\ f_2 \\ \cdots \\ f_N \end{bmatrix}. \tag{5}$$

Equation (5) can be compactly written as:

$$\{F_k\}_{M\times 1} = P^{\text{H}}_{N\times M}\{f_k\}_{N\times 1}, \tag{6}$$

where $\boldsymbol{f}$ and $\boldsymbol{F}$ stand for the RWG functions and SFs defined on the body, and $\boldsymbol{P}$ is the expansion coefficients matrix of SFs.

To get the expansion coefficients matrix $\boldsymbol{P}$, there are three steps.

Step 1: setting auxiliary exciting sources (AES).

Initially, Matekovits et al. defined AES on a series of discrete small RWG functions around the target, as shown in Fig. 1 (a). Then, in 2010, Bo Zhang et al. defined AES on an irregularly meshed surface which makes AES with diverse polarizations, as shown in Fig. 1 (b) [14]. This is beneficial to improve accuracy, and AES will be set in the second way in this work.

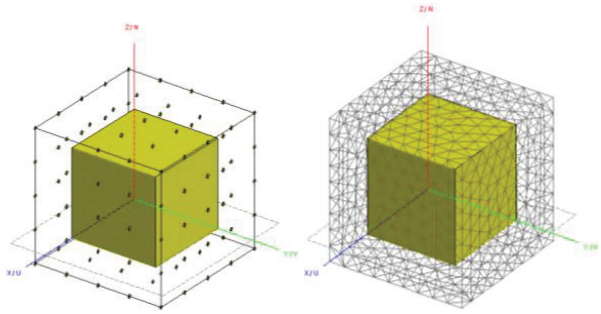

(a) (b)

Fig. 1. A cube surrounded by a series of AES: (a) AES defined on a series of discrete small RWG functions and (b) AES defined on a meshed surface.

Step 2: solving solution space.

Defining the mutual coupling impedance matrix between target and AES as V^e, the solution space $\boldsymbol{R}$ of SFs can be computed as:

$$R_{N\times(S+1)} = Z^{-1}(V + V^e), \tag{7}$$

where N is the number of RWG functions defined on the target and S represents the number of AES.

Equation (7) shows that the solution space $\boldsymbol{R}$ contains two parts:

(1) Response to natural excitations (incident wave):

$$r^1 = Z^{-1}V. \tag{8}$$

(2) Response to AES:

$$[r^2, r^3, \ldots, r^{S+1}] = Z^{-1}V^e, \tag{9}$$

where $\boldsymbol{r}^i$ (i=1, 2,…, S+1) is the i-th column of $\boldsymbol{R}$.

Step 3: extracting independent items.

To extract independent items from the solution space $\boldsymbol{R}$, SVD is usually adopted, as shown in equation (10), where ρ_i is the i-th singular value of $\boldsymbol{R}$ and $\rho_1 \geq \rho_2 \geq \cdots \geq \rho_N$:

$$R = U\rho V^{\mathrm{H}};\ \rho = \mathrm{diag}(\rho_1, \rho_2, \cdots, \rho_N). \tag{10}$$

Considering $\boldsymbol{U}$ is a unitary matrix, if $\rho_M/\rho_1 < \rho_{SBF}$, we will take the first M columns of $\boldsymbol{U}$ as the expansion coefficients matrix $\boldsymbol{P}$ of SFs, as shown in equation (11), where $\boldsymbol{I}_M$ represents an identity matrix:

$$P_{N\times M} = U_{N\times N}\begin{bmatrix} I_M \\ 0 \end{bmatrix}_{N\times M}. \tag{11}$$

The truncation error ρ_{SBF} is usually determined by operator and, in different applications, ρ_{SBF} is also different.

According to equation (4), we can get the current coefficients of SFs:

$$Y = W_{\mathrm{SBF}}^{-1} G_{\mathrm{SBF}} = (P^{\mathrm{H}} Z P)^{-1} P^{\mathrm{H}} V. \tag{12}$$

Then, based on equation (6), the current coefficient of RWG functions defined on the targets will be:

$$I = PY = P(P^{\mathrm{H}} Z P)^{-1} P^{\mathrm{H}} V. \tag{13}$$

Substituting equation (11) into equation (13) we get:

$$I = U\begin{bmatrix} I_M \\ 0 \end{bmatrix}\left\{[I_M\ 0]\,U^{\mathrm{H}} Z U \begin{bmatrix} I_M \\ 0 \end{bmatrix}\right\}^{-1}[I_M\ 0]\,U^{\mathrm{H}} V. \tag{14}$$

Equation (14) is rather interesting to us. Left multiply $[\boldsymbol{I}_M\ \boldsymbol{0}]$ represents the first M rows of a matrix, and right multiply $[\boldsymbol{I}_M\ \boldsymbol{0}]^H$ represents the first M columns of a matrix. Assign $\boldsymbol{U}^H\boldsymbol{Z}\boldsymbol{U}$=$T$, the inner part of equation (14) can be rewritten as:

$$\left\{[I_M\ 0]\,U^{\mathrm{H}} Z U \begin{bmatrix} I_M \\ 0 \end{bmatrix}\right\}^{-1} = \left\{[I_M\ 0]\,T \begin{bmatrix} I_M \\ 0 \end{bmatrix}\right\}^{-1} = T_M{}^{-1}, \tag{15}$$

where T_M is a sub-matrix composed of the first M rows and the first M column of T.

Substituting equation (15) into equation (14), we get:

$$I = U\begin{bmatrix} I_M \\ 0 \end{bmatrix} T_M{}^{-1}\,[I_M\ 0]\,U^{\mathrm{H}} V = P T_M{}^{-1} P^{\mathrm{H}} V. \tag{16}$$

From the theory of SBFM we know that, with the growth of M, current coefficients of RWG functions calculated in equation (16) will get closer and closer to that calculated by MoM.

Let us take the example in Fig. 1 (b) into consideration. There are a total of 1944 RWG functions defined on the surface of cube. Current coefficients of these RWG functions are calculated by MoM and SBFM, and the results are denoted as I_{MoM} and I_{SBF}, respectively.

Figure 2 exhibits the discrepancy of I_{MoM} and I_{SBF} when different numbers of SFs are adopted. It is obvious that, with the growth of M, current coefficients of RWG functions calculated by MoM and SBFM get closer and closer which is coincident with our cognition. However, if we use QR decomposition rather than SVD to extract independent items from solution space $\boldsymbol{R}$, as shown in equation (17), will the conclusion still be right?

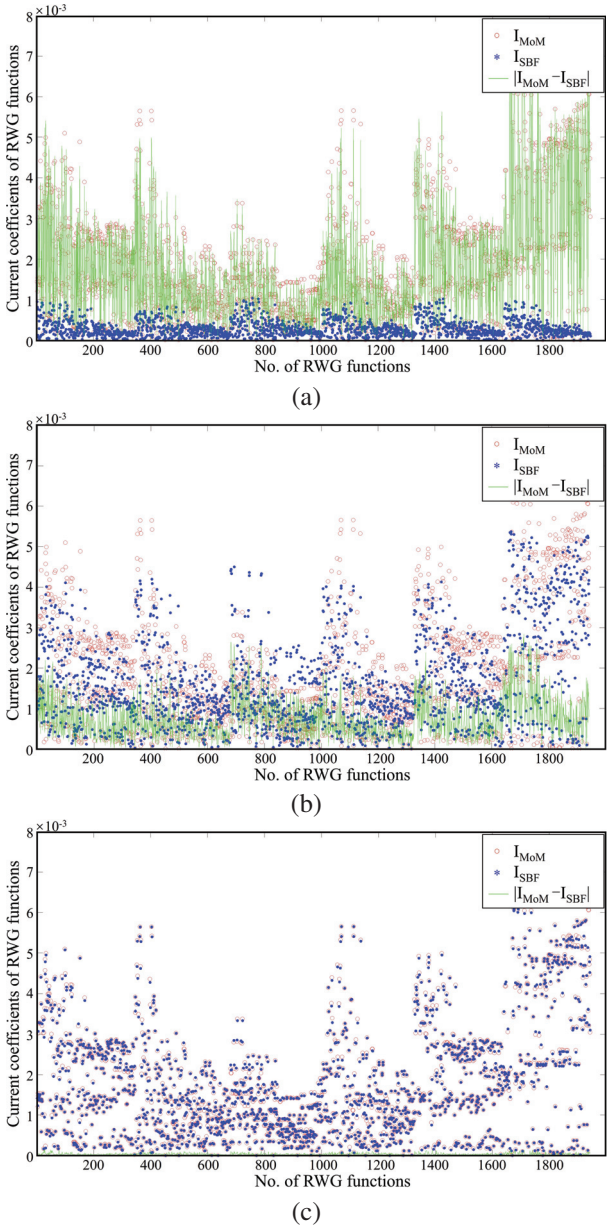

Fig. 2. Absolute current coefficients of RWG functions defined on a cube in the case of SVD: (a) M=1, (b) M=50 and (c) M=150.

$$R_{N\times(S+1)} = Q_{N\times N}\begin{bmatrix} r_{11} & & * \\ & \cdots & \\ 0 & & * \end{bmatrix}_{N\times(S+1)}. \tag{17}$$

Similar to $\boldsymbol{U}$, $\boldsymbol{Q}$ is also a unitary matrix and we will take the first M columns as the expansion coefficients

matrix $\boldsymbol{P}$ of SFs:

$$P_{N\times M} = Q_{N\times N}\begin{bmatrix} I_M \\ 0 \end{bmatrix}_{N\times M}. \tag{18}$$

In the case of QR decomposition, current coefficients of RWG functions defined on the surface of the cube are computed and the results are shown in Fig. 3. It is not difficult to see that accuracy of SBFM does not improve with the growth of M and current coefficients calculated by SBFM coincide exactly with those of MoM. Moreover, for SBFM, only one SF (M=1) is enough to get the same level of accuracy with MoM. This is somewhat interesting.

To further verify the above conclusion, two single models, sphere and cylinder, shown in Fig. 4, are analyzed using SBFM+SVD/QR. Similar to the cases in Figs. 2 and 3, MoM and SBFM are used to calculate the current coefficients of RWG functions defined on the surface of a sphere (1161 RWG functions) and a cylinder (1713 RWG functions). Figure 5 exhibits the absolute discrepancy of current coefficients calculated by different approaches. The results of sphere and cylinder are similar to that of cube. This suggests that the conclusions drawn from Fig. 3 may be universal. In summary, for a single body, if SBFM+QR decomposition is adopted, only one SF is enough to get the same level of accuracy with MoM.

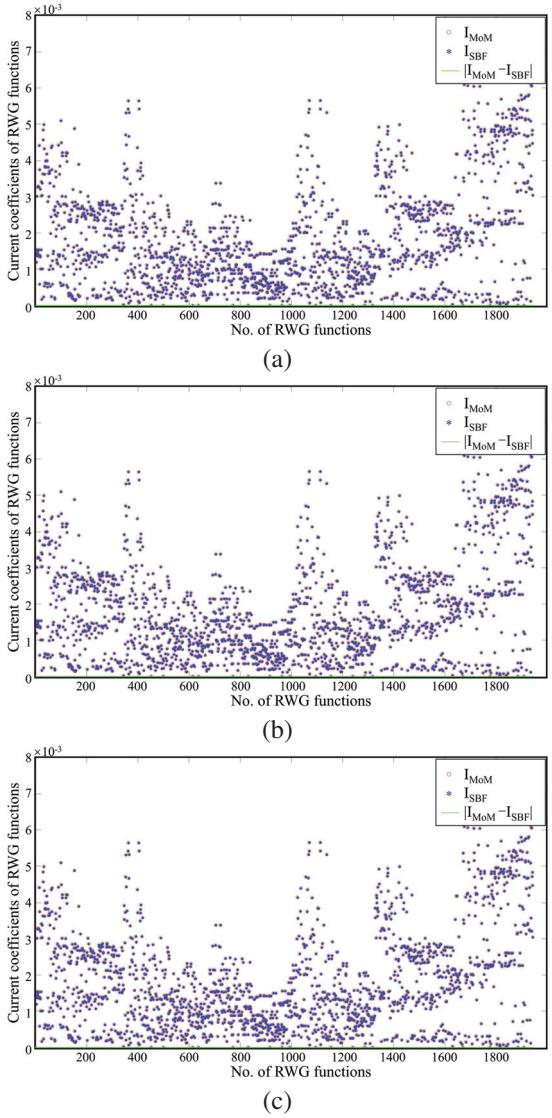

Fig. 3. Absolute current coefficients of RWG functions defined on a cube in the case of QR: (a) M=1, (b) M=50, and (c) M=150.

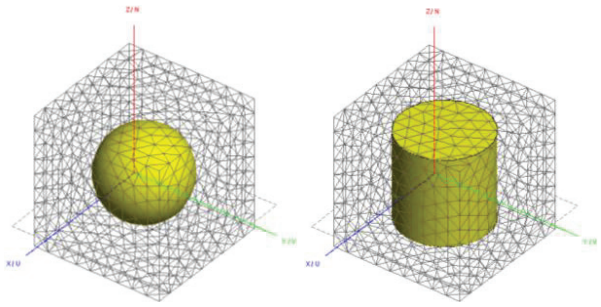

Fig. 4. A target surrounded by a series of AES: (a) sphere and (b) cylinder.

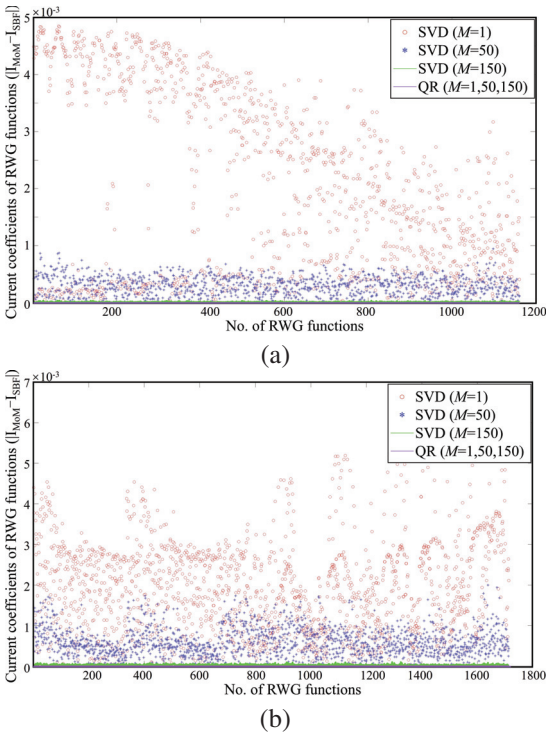

Fig. 5. Absolute discrepancy of current coefficients calculated by MoM and SBFM: (a) sphere and (b) cylinder.

III. EXPLANATION AND EXPANSION

In section II, we can see that, for a single body, if QR decomposition is adopted to extract independent items from solution space, one SF is enough to get satisfying accuracy. In this section, we give a theoretical explanation on this phenomenon.

Denote $\boldsymbol{Q}=[\boldsymbol{q}^1\ \boldsymbol{q}^2\ \ldots\ \boldsymbol{q}^N]$, where $\boldsymbol{q}^i$ (i=1, 2,..., N) is the i-th column of $\boldsymbol{Q}$. According to the principle of QR decomposition, a unitary matrix and an upper triangular matrix will be yielded after decomposition, as shown in equation (17). Then, we get:

$$q^1 r_{11} = r^1. \tag{19}$$

Substituting equation (8) into equation (19) to get:

$$q^1 = \frac{1}{r_{11}} Z^{-1} V. \tag{20}$$

If only one SF is adopted, it will be $\boldsymbol{P}=\boldsymbol{q}^1$. Then, according to equation (16), the current coefficients of RWG functions can be computed as:

$$I = q^1 \frac{1}{t_{11}} [q^1]^{\mathrm{H}} V, \tag{21}$$

where t_{11} is the element located in the first row and the first column of matrix T and $T=\boldsymbol{Q}^H Z \boldsymbol{Q}$. According to the definition of matrix T, t_{11} is computed as:

$$t_{11} = \sum_{j=1}^{N} \sum_{i=1}^{N} q_{i1} z_{ij} q_{j1}, \tag{22}$$

where q_{i1} (i=1, 2,..., N) is the i-th element of $\boldsymbol{q}^1$.

Then, substituting equation (20) into equation (21) and considering the results of $[\boldsymbol{q}^1]^H V$ is a scalar, equation (21) can be written as:

$$I = \frac{k_e}{t_{11}} q^1 = \frac{k_e}{t_{11} r_{11}} Z^{-1} V, \tag{23}$$

where k_e is a scalar and defined as $k_e=[\boldsymbol{q}^1]^H V$.

For the three models shown in Figs. 1 (b) and 4, we can compute the scalar coefficients $k_e/(t_{11}r_{11})$, as given in Table 1.

Table 1: Scalar coefficients of targets

	$\boldsymbol{k_e}$	$\boldsymbol{t_{11}}$	$\boldsymbol{r_{11}}$	$\boldsymbol{k_e/(t_{11}r_{11})}$
cube	−0.0047 +0.0002i	0.0453 −0.0016i	−0.1037	1.0
sphere	0.0005 −0.0011i	0.0053 −0.0119i	0.0887	1.0
cylinder	0.0016 −0.0019i	0.0165 −0.0193i	0.0991	1.0

Combing the results in Table 1 and equation (23), we can see that the current coefficients of RWG functions calculated by SBFM are exactly equal to that of MoM when QR decomposition is adopted which perfectly explains the phenomenon shown in Figs. 3 and 5. However, it should be noted that the conclusion only suits for a single body. This feature can give us some useful guidance and may be helpful for the analysis of periodic structures, such as frequency selective surface (FSS) and energy selective surface (ESS) [25].

Figure 6 shows the algorithm flowchart of SBFM for solving array structures.

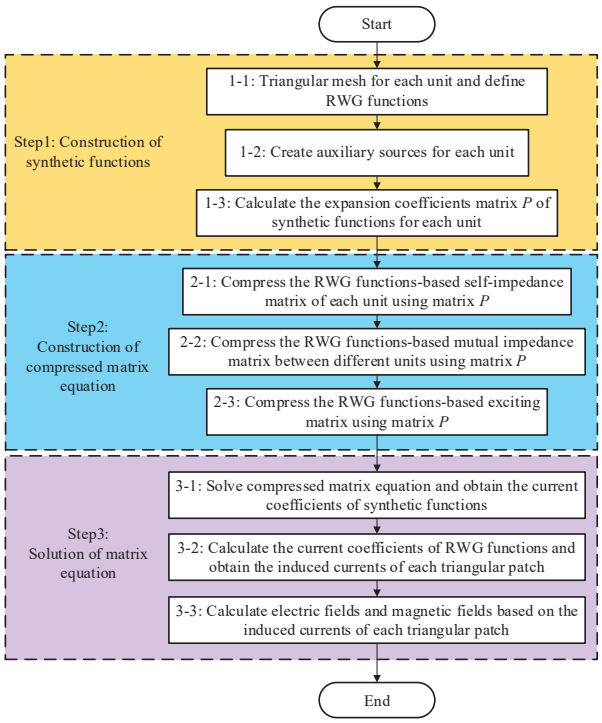

Fig. 6. Algorithm flowchart of SBFM for solving array structures.

For a periodic array composed of B elements, the compressed matrix equation of SBFM is shown in Fig. 7, where W_{bb} represents the compressed self-impedance matrix of unit b, W_{pq} represents the compressed mutual-impedance matrix between unit p and unit q, and G_b stands for the compressed exciting matrix of unit b.

The matrices in Fig. 7 can be computed as:

$$\begin{cases} W_{bb} = P_b^{\mathrm{H}} Z_{bb} P_b \\ W_{pq} = P_p^{\mathrm{H}} Z_{pq} P_q \\ G_b = P_b^{\mathrm{H}} V_b \end{cases}, \tag{24}$$

where $\boldsymbol{P}_b$ is the expansion coefficients matrix of SFs, and Z_{bb} and V_b are impedance matrix and exciting matrix of MoM.

In the case of periodic structures, to obtain the expansion coefficients matrix of SFs defined on each unit (steps 1-3 in Fig. 6), QR decomposition can be used to extract the independent items from the solution space. Moreover, this may bring benefits such as using less SFs to get a satisfying accuracy. To further validate this, a 10×10 circular microstrip patch antenna array is analyzed, as shown in Fig. 8.

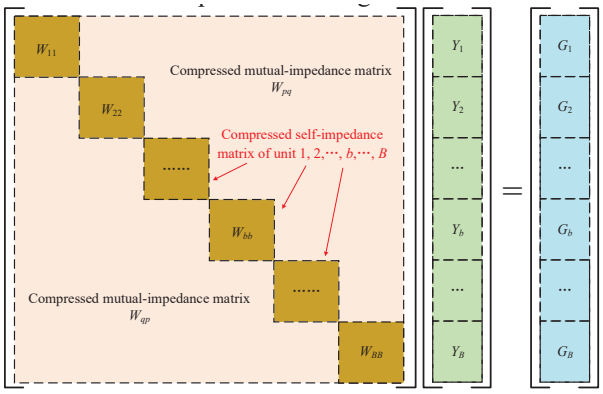

Fig. 7. Schematic diagram of the matrix equation of SBFM for array structures.

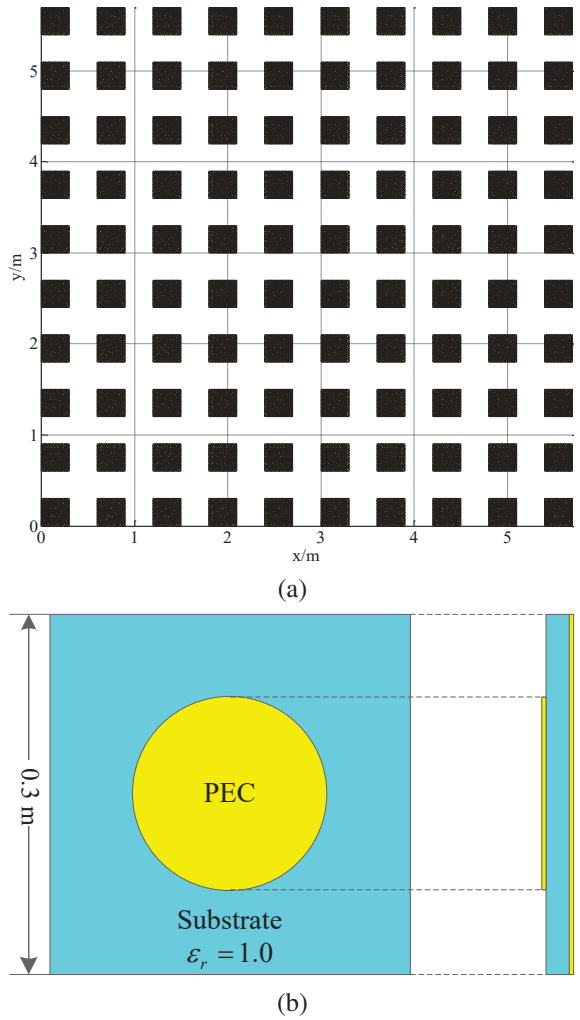

Fig. 8. A 10×10 circular microstrip patch antenna array: (a) layout of the array and (b) structure of a single unit.

Incident wave is a plane wave coming from +z axis and polarizing +x axis. Frequency of incident wave is 1.0 GHz. After triangulation, there are 100 units in the array and 628 RWG functions are defined on each unit. Thus, for the whole array, there are 62800 unknowns. Denote the distance between adjacent units by d and two cases are considered here: d=0.5λ and d=1.0λ (λ is the wavelength of the incident wave).

Bistatic RCS of the antenna array on xoz plane and current coefficients of RWG functions are calculated using MoM, SBFM+SVD, and SBFM+QR. To evaluate the accuracy of different methods, the mean error of RCS and relative residual error of current coefficients are calculated here. They are defined as equations (26) and (27), respectively:

$$\delta_{\mathrm{RCS}} = \frac{1}{N}\sum_{i=1}^{N} |\sigma_i^{\mathrm{SBFM}} - \sigma_i^{\mathrm{MoM}}|, \tag{25}$$

where σ_i represents the i-th data of BiRCS and N stands for the total number of data taken into consideration:

$$\delta_I = \frac{||I_{\mathrm{SBFM}} - I_{\mathrm{MoM}}||}{||I_{\mathrm{MoM}}||}, \tag{26}$$

where $||X||$ represents the 2-norm of vector X.

Figure 9 shows BiRCS data of the antenna array, from which we can see that the results of SBFM+QR

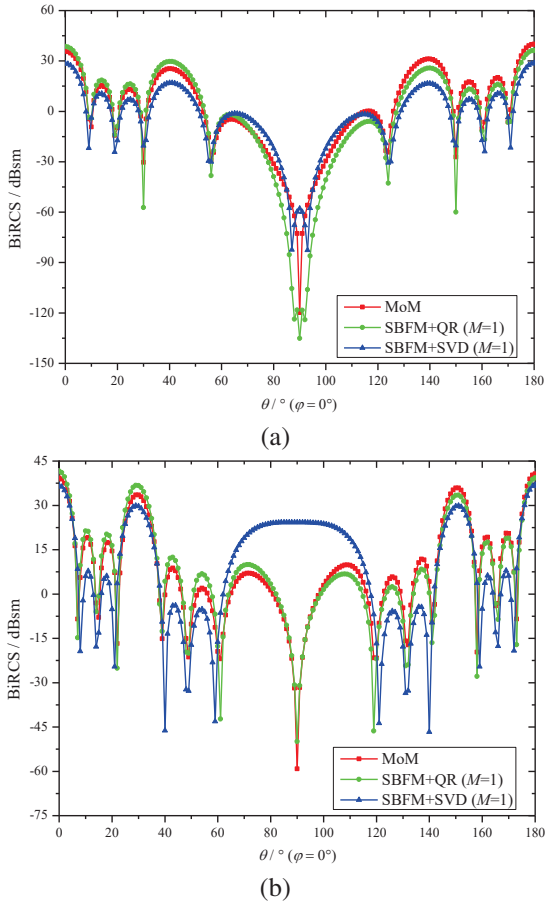

Fig. 9. BiRCS on xoz plane: (a) d=0.5λ and (b) d=1.0λ.

are closer to MoM than SBFM+SVD if only one SF is adopted.

To be more specific, Fig. 10 exhibits the convergent curves of δ_I changing with the number of SFs. In general, the accuracy of SBFM+SVD and SBFM+QR both improve with the growth of the number of SFs. However, there is a low point in SBFM+QR at M=1 in contrast to SBFM+SVD. This verifies our previous prediction: QR is better than SVD in the case of periodic arrays if only one SF is adopted. Furthermore, in terms of the fluctuation on convergent curves, QR is also less than SVD.

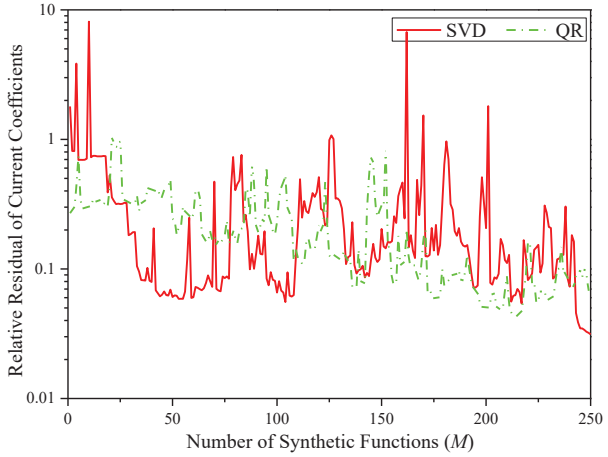

(a)

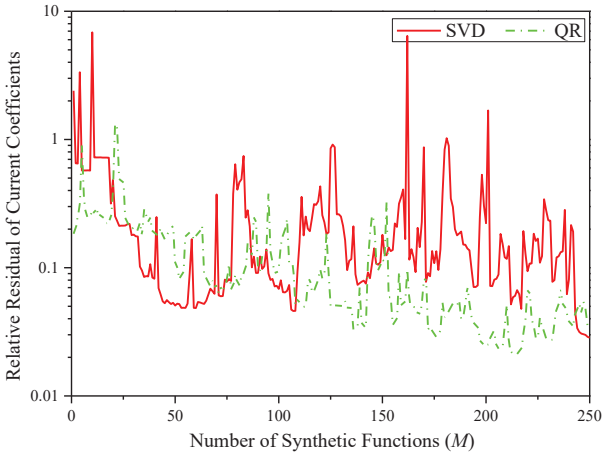

(b)

Fig. 10. Relative residual error of current coefficients changing with the number of SFs: (a) d = 0.5λ and (b) d = 1.0λ.

Table 2 shows the computational accuracy between different matrix decomposition methods. Interestingly, the accuracy of SBFM+QR at M=1 is approximately equal to SBFM+SVD at M=125 in terms of BiRCS. However, when it comes to current coefficients, accuracy of the former is apparently higher than the latter. This is easy to explain: RCS is an integral of all surface currents and accuracy is mainly determined by these strong currents. Thus, to get the same level of accuracy, δ_I usually needs more SFs than δ_{RCS}. Table 3 exhibits the elapsed time and memory cost of different methods. From the comparison between SBFM+SVD and SBFM+QR, it is not difficult to see that the decrease of the number of SFs is meaningful.

Table 2: Computational accuracy of different matrix decomposition methods

		δ_I		δ_{RCS}	
		0.5λ	1.0λ	0.5λ	1.0λ
SBFM+SVD	M=1	1.80	2.40	12.5	18.7
	M=125	0.99	0.85	4.51	3.11
SBFM+QR	M=1	0.27	0.18	4.31	4.46

Table 3: Elapsed time and memory cost of SBFM and MoM

		P	***Z***	***I***	**Total Time**
MoM		0 s	3.16 h 104.87 GB	53.76 h	56.94 h
SBFM + SVD	M=1	4.89 s	2.07 h 273.02 KB	0.02 s	2.10 h
	M=125	5.09 s	2.35 h 4.16 GB	989.59 s	2.69 h
SBFM + QR	M=1	2.92 s	2.07 h 279.86 KB	0.02 s	2.10 h

IV. CONCLUSION

SBFM and its application in periodic structures is discussed in this work. Unlike the traditional case of SVD decomposition, QR decomposition is used to extract expansion coefficients of SFs from solution space. Based on theoretical analysis, we prove that SBFM+QR can get the same level of accuracy with MoM with only one SF when a single body is concerned. Moreover, this feature can be extended to periodic arrays. For periodic arrays, only one synthetic function is enough to get high accuracy if SBFM+QR is adopted and this may lead to a series of benefits such as decreasing memory cost and improving efficiency.

ACKNOWLEDGMENT

This work was supported by the National Natural Science Foundation of China under Grant 62101564 and Hunan Provincial Natural Science Foundation of China under Grant 2022JJ20045.

REFERENCES

[1] R. Liu, G. Xiao, and Y. Hu, "Solving surface-volume integral equations for PEC and inhomogeneous/anisotropic materials with multibranch basis

functions," *Applied Computational Electromagnetics Society (ACES) Journal*, vol. 39, no. 2, pp. 108-114, 2024.

[2] W. Lu, W. Xiang, W. Wu, and W Yang, "The fast algorithms for electromagnetic analysis of the large-scale and finite periodic structures," *Chinese Journal of Radio Science*, vol. 35, no. 1, pp. 85-92, 2020.

[3] W. He, Z. Yang, X. Huang, W. Wang, M. Yang, and X. Sheng, "Solving electromagnetic scattering problems with tens of billions of unknowns using GPU accelerated massively parallel MLFMA," *IEEE Trans. Antennas Propag.*, vol. 70, no. 7, pp. 5672-5682, 2022.

[4] C. Wu, L. Guan, P. Gu, and R. Chen, "Application of parallel CM-MLFMA method to the analysis of array structures," *IEEE Trans. Antennas Propag.*, vol. 69, no. 9, pp. 6116-6121, 2021.

[5] M. Li, T. Su, and R. Chen, "Equivalence principle algorithm with body of revolution equivalence surface for the modeling of large multiscale structures," *IEEE Trans. Antennas Propag.*, vol. 64, no. 5, pp. 1818-1828, 2016.

[6] M. Yang, B. Wu, X. Huang, and X. Sheng, "The progress of domain decomposition methods for 3D electromagnetic scattering problems," *Chinese Journal of Radio Science*, vol. 35, no. 1, pp. 37-45, 2020.

[7] R. Zhao, Y. Chen, X. Gu, Z. Huang, H. Bagci, and J. Hu, "A local coupling multitrace domain decomposition method for electromagnetic scattering from multilayered dielectric objects," *IEEE Trans. Antennas Propag.*, vol. 68, no. 10, pp. 7099-7108, 2020.

[8] K. Fan, B. Wei, J. Chen, and B. He. "A spatial modes filtering FETD method combined with domain decomposition for simulating fine electromagnetic structures," *IEEE Microwave and Wireless Components Letters*, vol. 32, no. 11, pp. 1259-1262, 2022.

[9] M. Li, M. A. Francavilla, R. Chen, and G. Vecchi, "Wideband fast kernel-independent modeling of large multiscale structures via nested equivalent source approximation," *IEEE Trans. Antennas Propag.*, vol. 63, no. 5, pp. 2122-2134, 2015.

[10] Y. Xu, H. Yang, R. Shen, L. Zhu, and X. Huang, "Scattering analysis of multiobject electromagnetic systems using stepwise method of moment," *IEEE Trans. Antennas Propag.*, vol. 67, no. 3, pp. 1740-1747, 2019.

[11] L. Matekovits, G. Vecchi, G. Dassano, and M. Orefice, "Synthetic function analysis of large printed structures: the solution space sampling approach," *IEEE Antennas Propag. Society International Symposium*, no. 2, pp. 568-571, 2001.

[12] L. Matekovits, V. A. Laza, and G. Vecchi, "Analysis of large complex structures with the synthetic-functions approach," *IEEE Trans. Antennas Propag.*, vol. 55, no. 9, pp. 2509-2521, 2007.

[13] H. Yuan, S. Gong, Y. Guan, and D. Su, "Scattering analysis of the large array antennas using the synthetic basis function method," *Journal of Electromagnetic Waves and Applications*, vol. 23, pp. 309-320, 2009.

[14] B. Zhang, G. Xiao, J. Mao, and Y. Wang, "Analyzing large-scale non-periodic arrays with synthetic basis functions," *IEEE Trans. Antennas Propag.*, vol. 58, no. 11, pp. 3576-3584, 2010.

[15] W. Chen, G. Xiao, S. Xiang, and J. Mao, "A note on the construction of synthetic basis functions for antenna arrays," *IEEE Trans. Antennas Propag.*, vol. 60, no. 7, pp. 3509-3512, 2012.

[16] Y. Xu, H. Yang, and W. Yu, "Scattering analysis of periodic composite metallic and dielectric structures with synthetic basis functions," *Applied Computational Electromagnetics (ACES) Society Journal*, vol. 30, no. 10, pp. 1059-1067, 2015.

[17] Y. Xu, H. Yang, W. Yu, and J. Zhu, "An automatic scheme for synthetic basis functions method," *IEEE Trans. Antennas Propag.*, vol. 66, no. 3, pp. 1601-1606, 2018.

[18] Y. Xu, X. Huang, C. Liu, S. Zha, and J. Liu, "Synthetic functions expansion: automation, reuse, and parallel," *IEEE Trans. Antennas Propag.*, vol. 69, no. 3, pp. 1825-1830, 2021.

[19] N. Hu, Y. Xu, and P. Liu, "A numerical analysis of conformal energy selective surface array with synthetic functions expansion," *Applied Computational Electromagnetics Society (ACES) Journal*, vol. 39, no. 2, pp. 115-122, 2024.

[20] Y. Xu, C. Liu, Z. Wu, N. Hu, J. Liu, and P. Liu, "Fast electromagnetic simulation method for large-scale quasi-periodic arrays," *Sci. Sin. Inform.*, vol. 54, no. 2, pp. 430-448, 2024.

[21] W. Lu, T. Cui, Z. Qian, X. Yin, and W. Hong, "Accurate analysis of large-scale periodic structures using an efficient sub-entire-domain basis function method," *IEEE Trans. Antennas Propag.*, vol. 52, no. 11, pp. 3078-3085, 2004.

[22] V. V. S. Prakash and R. Mittra, "Characteristic basis function method: A new technique for efficient solution of method of moments matrix equations," *Microwave and Optical Technology Letters*, vol. 36, no. 2, pp. 95-100, 2003.

[23] C. S. Park, I. P. Hong, Y. J. Kim, and J. G. Yook, "Acceleration of multilevel characteristic

basis function method by multilevel multipole approach," *IEEE Trans. Antennas Propag.*, vol. 68, no. 10, pp. 7109-7120, 2020.

[24] Y. Xu, H. Yang, J. Lu, W. Yu, W. Yin, and D. Peng, "Improved synthetic basis functions method for nonperiodic scaling structures with arbitrary spatial attitudes," *IEEE Trans. Antennas Propag.*, vol. 65, no. 9, pp. 4728-4741, 2017.

[25] Z. Wu, Y. Xu, P. Liu, T. Tian, and M. Lin, "An ultra-broadband energy selective surface design method: From filter circuits to metamaterials," *IEEE Trans. Antennas Propag.*, vol. 71, no. 7, pp. 5865-5873, 2023.

Yanlin Xu received the B.S., M.S., and Ph.D. degrees in electronic science and technology from the National University of Defense Technology (NUDT), Changsha, China, in 2013, 2015, and 2018, respectively. He is currently an Associate Professor with the College of Electronic Science and Technology, NUDT. His current research interests include electromagnetic compatibility and protection, and computational electromagnetism.

Ning Hu (corresponding author) received the B.S. degree in electronic engineering and the M.S. degree in electronic science and technology from National University of Defense Technology (NUDT), Changsha, Hunan, P. R. China, in 2017 and 2019, respectively. He received the Ph.D. degree in information and communication engineering from NUDT in 2023. His research interests include electromagnetic compatibility and protection, and metamaterials and antennas.

Chenxi Liu (corresponding author) received the B.S. degree in electrical engineering and the M.S. and Ph.D. degrees in electronic science and technology from the National University of Defense Technology, Changsha, China, in 2013, 2015, and 2019, respectively. He is currently an Associate Professor with the College of Electronic Science, National University of Defense Technology. His research areas of interest include electromagnetically induced transparency analogy based on metamaterial and tunable metamaterials based on active components.

Hao Ding received the B.S. and M.S. degrees from Air Force Engineering University (AFEU), Xian, China, in 2013 and 2016, respectively, and the Ph.D. degree from the University and Institute of Microelectronics, Chinese Academy of Sciences (IMECAS), Beijing, China, and AFEU, in 2020. He is now working as a Lecturer with the National University of Defense Technology, Changsha, China. His research interests include IC and microsystem designs for electromagnetic compatibility and protection.

Jun Li received the M.S. degree from the National University of Defense Technology (NUDT), Changsha, China, in 2015. He is currently a senior engineer with the second representative office of Changsha area. His current research interests include electromagnetic compatibility antenna, and big data analysis.

Conceptual Design and Preliminary Verification of a Double-bunch Switchyard for SXFEL

Yongfang Liu, Jin Tong, Sheying Li, Yizhou Jiang, Qibing Yuan, and Bo Liu*

Shanghai Advanced Research Institute
Chinese Academy of Sciences, Shanghai 201204, China
bo.liu@sari.ac.cn

Abstract – The Shanghai soft X-ray free-electron laser (SXFEL) is the first X-ray free-electron laser (FEL) user facility in China. To improve the utilization efficiency of the linear accelerator, SXFEL plans to upgrade to double-bunch mode with a bunch time separation of 100 ns and a maximum repetition rate of 50 Hz. A new conceptual beam distribution system is designed to separate the double beam bunch-by-bunch. Conceptual design and prototype implementation of a double-bunch separation system was implemented. The beam distribution system consists of four in-vacuum kicker magnets and one Lambertson septum magnet. This paper presents the design considerations and preliminary verification of a beam bunch distribution system. Distributed magnets and excitation power supply are introduced in detail. The relevant simulation and experimental results of the magnets and pulsed power supply are introduced also.

Index Terms – Beam distribution system, double-bunch separation, kicker magnet, pulsed power supply, septum magnet.

I. INTRODUCTION

The Shanghai soft X-ray free-electron laser (SXFEL), the first soft X-ray free-electron laser (FEL) facility in China, is a fourth-generation light source [1]. The SXFEL was made available to domestic and foreign users at the end of 2022 [2]. Two undulator lines produce FEL radiation with the shortest wavelength of approximately 2 nm. The beam distribution system, which is used for deflecting beam bunches with a specified mode, is located between the linear accelerator and the undulator lines. To enhance the utilization efficiency of the SXFEL, the linear accelerator will be upgraded from single-electron bunch mode with a 50-Hz maximum repetition frequency to double-electron bunch mode [3]. The two bunches, which are separated in time by 100 ns, will be distributed to two different undulator lines by the beam distribution system [4]. The existing beam distribution system is equipped with a single 54-mrad deflection angle kicker magnet with a 30-μs pulsed width power supply [5]. Beam distribution systems are designed for the world's Most FEL. For example, the beam distribution system of SwissFEL comprises a fast kicker magnet and a Lambertson septum magnet. A resonant kicker is used to separate the two bunches separated in time by 28 ns [6–7]. SACLA deflects interval beam bunches of 16.7 ms to two undulator lines using a kicker magnet and a septum magnet [8]. The beam distribution system of LCLS-II is composed of a transmission line kicker magnet and a direct current septum magnet to distribute 929-kHz beam bunches into different undulator lines [9]. The beam distribution system of EXFEL uses two types of kicker magnets and a septum magnet [10–11]. Using a single kicker magnet, the SXFEL facility separates beam bunches of 20 ms into two undulator lines [12–13]. Nevertheless, the existing beam distribution kicker magnet of the SXFEL cannot meet the capacity requirements for an increasing or decreasing edge of less than 100 ns. To meet the requirements of the new beam distribution mode, the current beam distribution system needs to be upgraded. Figure 1 shows the configuration of the new beam distribution system. It deflects double electron bunches with an energy of 1.5 GeV to the SBP and SUD undulator lines. It comprises four kicker magnets and a DC Lambertson magnet. When the kicker magnets are activated, four kicker magnets deflect the beam bunch vertically by 5.2 mrad. Afterward, the beam bunch passes through the field-free region of the DC Lambertson magnet with a vertical distance of approximately 16 mm. Binding with the magnet downstream, the beam bunch in this case is transmitted to the SBP undulator line. When the kicker magnets are turned off, the beam bunch passes through the field region of the DC Lambertson magnet with a horizontal deflection angle of 54 mrad. In this case, the beam bunch is transmitted to the SUD undulator line. Table 1 gives a summary of the design parameters of the distribution magnets. To meet these requirements, four 300-mm lump-inductance kicker magnets with a fast leading edge pulse driver were designed in this

Submitted On: December 22, 2023
Accepted On: November 5, 2024

https://doi.org/10.13052/2025.ACES.J.400210

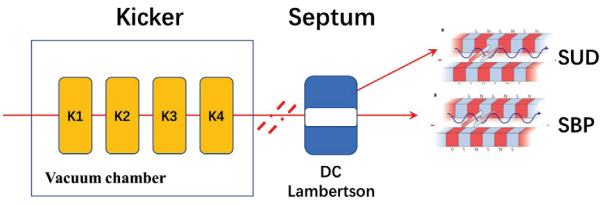

Fig. 1. Configuration of the beam distribution system: K1-K4 are kicker magnets, SUD and SBP are the two undulator lines.

Table 1: Design parameters of the distribution magnets

Parameter	Kicker Magnet	Septum Magnet
Magnet type	Lumped-inductance	Lambertson
Current shape	Trapezoidal wave	DC
Total deflection	5.2 mrad	54 mrad
Deflecting direction	Vertical	Horizontal
Leading edge	100 ns	—
Pulse repetition rate	50 Hz	—
Amplitude stability	200 ppm	50 ppm
Leakage field ratio	—	0.1%

study. A DC Lambertson magnet with a high main magnetic field and a low leakage field was selected [14–15]. This paper presents the conceptual design and preliminary verification of the magnet design and the source of excitation energy. In the present study, the purpose of employing a thyratron was to achieve a rising edge of less than 100 ns using a lumped-inductance kicker magnet with a 1-μH inductance and a Lambertson magnet, ensuring main-field uniformity and a low-leakage magnetic field. In this study, the utilization of a thyratron aims to achieve a rising edge of less than 100 ns of lumped inductance kicker magnet with 1 μH inductance and a Lambertson magnet ensuring main field uniformity and small leakage magnetic field.

II. KICKER MAGNET AND PULSED POWER SUPPLY

A. Kicker magnet design

The kicker magnet was a single-turn lumped-inductance type. Kicker inductance can be approximately calculated by equation (1):

$$L \approx \frac{\mu_0 N^2 H_{ap} L_e}{V_{ap}}, \quad (1)$$

where μ_0 denotes the vacuum permeability, N is the number of turns, H_{ap} is the distance between the go and return exciting current conductors, V_{ap} is the gap width of the ferrite core, and L_e is the effective length of the magnet. To reduce the inductance of the kicker magnet, each kicker had a length of 300 mm. Four kicker magnets of the same design were placed in one vacuum chamber. Driven by a single pulsed power supply, each kicker provided a deflection capability of 1.3 mrad, requiring a magnetic flux density of 230 gauss. The NiZn soft magnetic ferrite was proposed as the core material for its high frequency, high resistivity, and low loss characteristics. Although the in-vacuum structure could reduce the power consumption to some extent, it could cause cooling problems as well. Figure 2 shows the results of

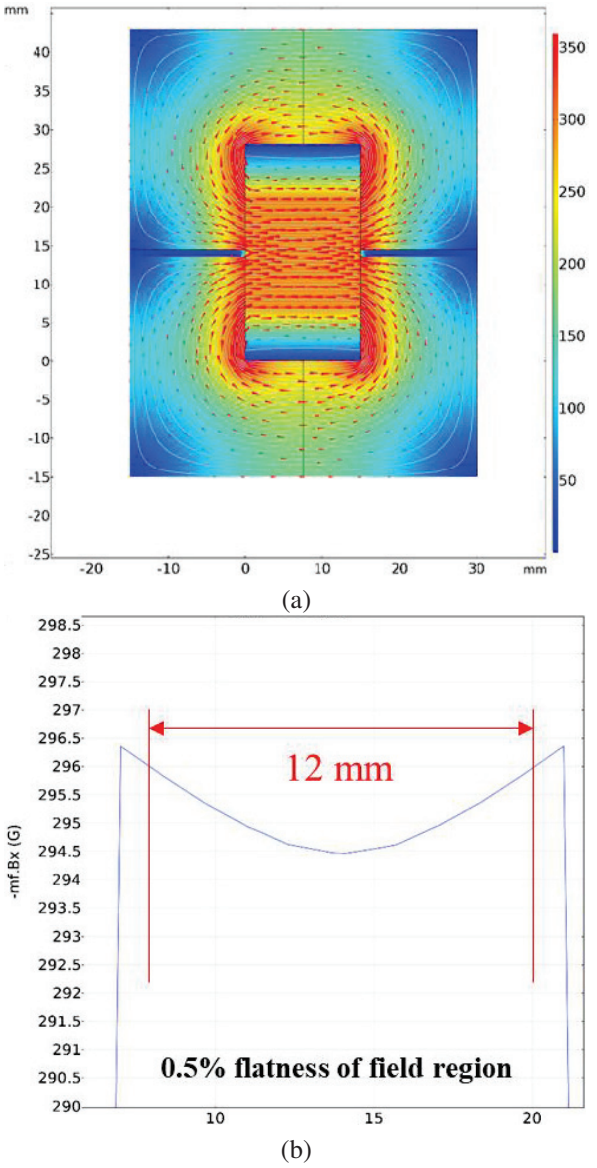

Fig. 2. Electromagnetic simulation results of cross-section: (a) magnetic field distribution for 2D and (b) good field region.

the Comsol electromagnetic simulation. The dimensions of the cross-section of each kicker magnet are shown in Fig. 2 (a). The core structure of the magnet corresponded to the window shape. Oxygen-free copper with less than 0.05% oxygen was used as the core material. Electromagnetic simulations were conducted using electromagnetic software to analyze the distribution of the magnetic flux intensity, a good field region, and integral strength along the beam direction. Figure 2 (b) shows that the flatness of a good field region is greater than 12 mm. Figure 3 displays the magnetic field distribution along the beam direction. The results of the simulations suggested that the integral strength along the beam direction could meet the requirements.

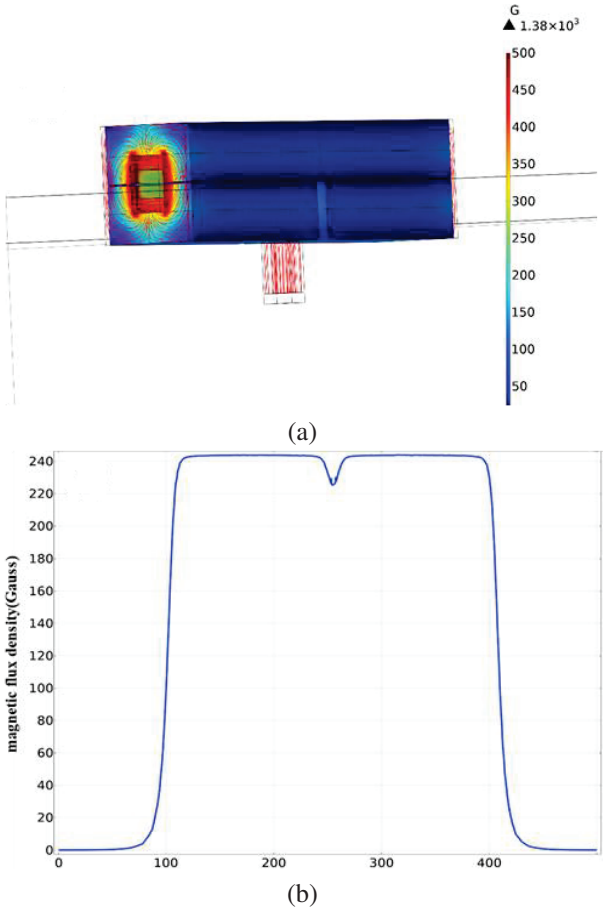

Fig. 3. Simulation results of three-dimensional analysis: (a) magnetic field distribution for 3D and (b) magnetic field distribution along the beam direction.

B. Pulsed power supply design

To separate the 100-ns beam bunch, the pulsed power supply needed to perform with a fast pulse edge. The pulsed power supply was based on the charging and discharging of pulse-forming lines controlled by a thyratron. The rate of increase in anode current was limited to 50 kA/μs. Figure 4 shows the schematic diagram of the pulsed excitation power supply. In the impedance-matching condition, the characteristic impedance of T1 was equal to R2. This time constant is expressed in equation (2):

$$\tau = \frac{L}{2Z}, \tag{2}$$

where L is the inductance of the kicker magnet and Z is the characteristic impedance of the PFL. Figure 5 illustrates the test bunch of the pulsed excitation power supply, while Fig. 6 shows the preliminary experimental result of the pulse waveform with an inductance load

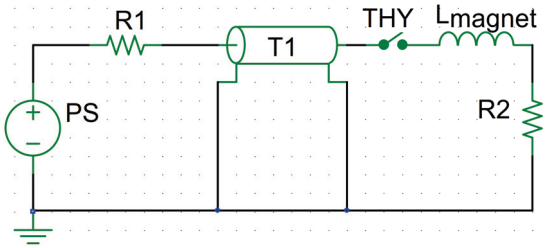

Fig. 4. Schematic diagram of the pulsed excitation power supply.

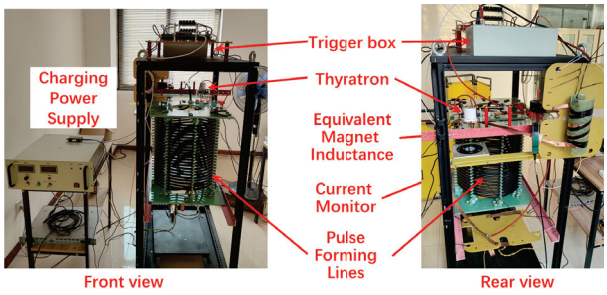

Fig. 5. Test bunch of the pulsed excitation power supply.

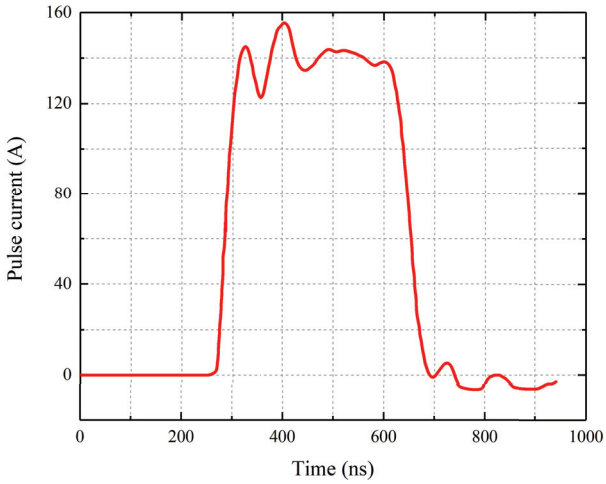

Fig. 6. Experimental result of pulse waveform.

equal to that of the kicker magnet. The leading edge was 80 ns, with an equivalent kicker magnet inductance. The pulse flat-tops could be further tuned for a better flatness.

III. SEPTUM MAGNET AND POWER SUPPLY

A. Septum magnet design

The septum magnet was of the Lambertson type. The principle of operation of the Lambertson septum was that high-permeability materials could function with almost any type of leakage magnetic field. According to the system layout and physical design of the SXFEL, the vertical distance between the deflected and undeflected beams at the entrance of the Lambertson magnet was 16 mm. The Lambertson magnet was designed to be 400 mm long. A main magnetic field of 0.7 T and a uniform range of at least 11 mm were required to deflect the electron beam horizontally by 54 mrad. The main-field uniformity in the Lambertson gap needed to be higher than 0.1% to introduce the smallest possible energy dispersion into the high-energy electron beam, whereas the leakage field integral needed to be less than 0.1%. With DC excitation current, the core of the Lambertson magnet was made of solid DT4 iron, which has good electromagnetic properties. The field-free region was designed to be a circular vacuum hole with a radius of 5 mm. At the same time, the vacuum hole was placed horizontally 7.5 mm further from the center of the bottom pole to reduce the width and relative cost of the magnet. To improve the main-field uniformity, two shims were installed on both sides of the bottom pole. The cross-section model of the Lambertson magnet was simulated using OPERA. Sufficient project margin was reserved around the coil to ensure the installation of the coil and to make the simulation as close to reality as possible. A TOSCA Magnetic Analysis in OPERA-3D was used to simulate the three-dimensional model. The simulation results are presented in Figs. 7 and 8.

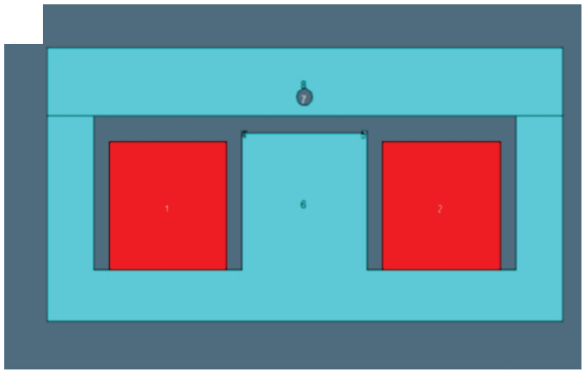

(a)

Fig. 7. *Continued.*

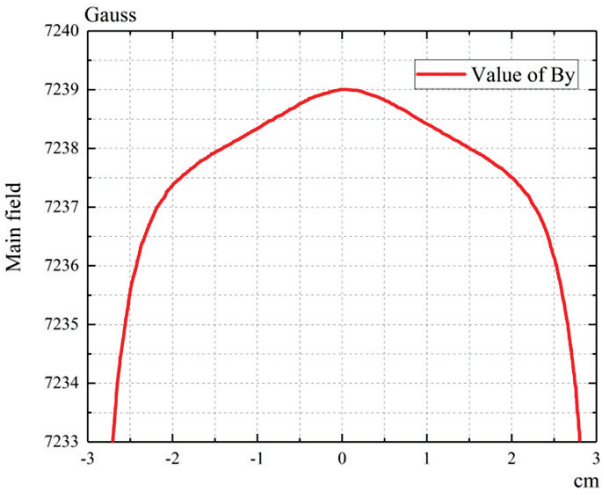

(b)

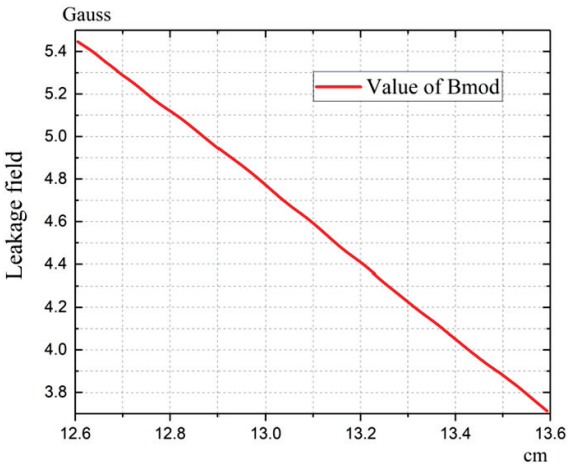

(c)

Fig. 7. Lambertson magnet simulation result of cross-section: (a) cross-section model of Lambertson magnet, (b) main field region, and (c) leakage field at the center of field-free region.

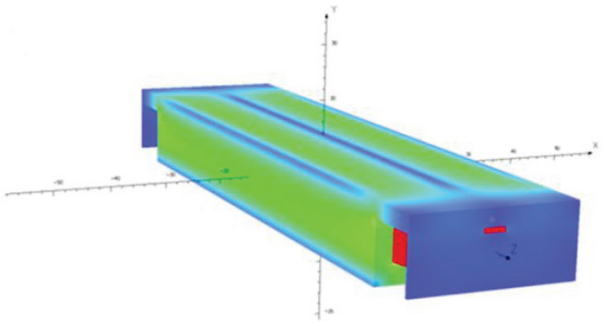

(a)

Fig. 8. *Continued.*

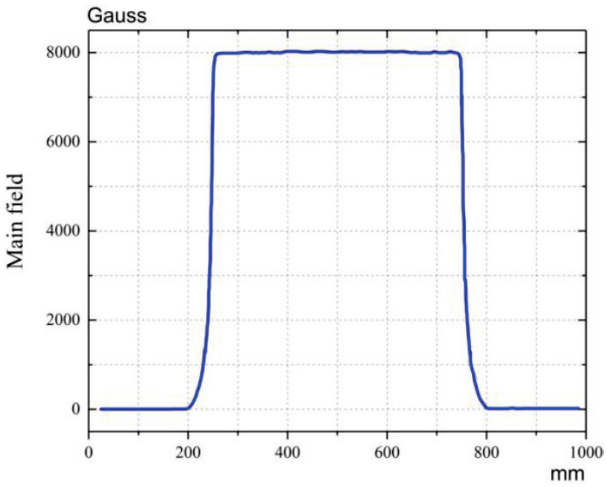

(b)

Fig. 8. Lambertson magnet simulation result of three-dimensional analysis: (a) magnetic field distribution for 3D and (b) magnetic field distribution along the beam direction in main field region.

B. DC excitation power supply

The excitation current for the Lambertson magnet was direct current (DC), provided by a DC switch power supply. Figure 9 shows the functional block diagram of the septum excitation power supply. Figure 10 pictorially shows the DC excitation power supply and presents the current measurement results. The current output stability of this power supply was less than 50 ppm.

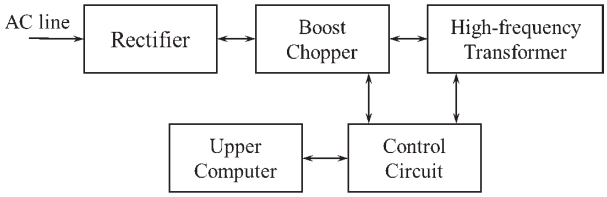

Fig. 9. Functional block diagram of septum excitation power supply.

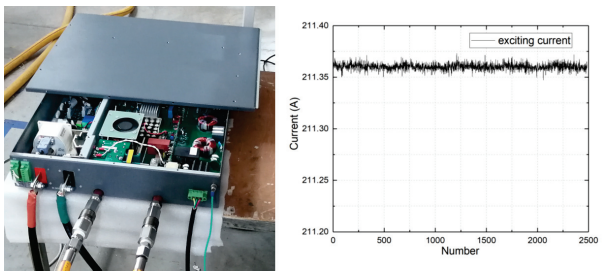

Fig. 10. The picture of DC excitation power supply and its current measurement result.

IV. CONCLUSION

This paper presented a study of the 100-ns double-beam bunch distribution system for SXFEL. The system included four vertical kicker magnets and one horizontal Lambertson magnet. The kicker magnets are based on in-vacuum lumped-inductance technology. The design parameters and simulation results of the kicker and septum were also analyzed. This study validated the feasibility of the 100-ns kicker leading edge pulsed power supply. Prototypes of the kicker and the Lambertson magnet are currently being processed and developed. Further studies on beam impedance effect and nonlinearities are being evaluated.

ACKNOWLEDGMENT

Project supported by the National Natural Science Foundation of China (No. 12005282) and Youth Innovation Promotion Association of Chinese Academy of Sciences (No. 2021283).

REFERENCES

[1] Z. Zhao, "The SXFEL upgrade: From test facility to user facility," *Applied Sciences*, vol. 12, no. 1, p. 176, 2021.

[2] Z. Zhao, D. Wang, Q. Gu, L. Yin, G. Fang, M. Gu, Y. Leng, Q. Zhou, B. Liu, C. Tang, W. Huang, Z. Liu, and H. Jiang, "SXFEL: A soft X-ray free electron laser in China," *Synchrotron Radiation News*, vol. 30, no. 6, pp. 29-33, 2017.

[3] M. H. Song, C. Feng, D. Huang, H. Deng, B. Liu, and D. Wang, "Wakefields studies for the SXFEL user facility," *Nuclear Science and Techniques*, vol. 28, no. 7, p. 90, 2017.

[4] Y.-F. Liu, H. Matsumoto, M. Gu, G.-Q. Li, and S. Li, "Design of an oil-immersed pulse modulator for X-band 50-MW Klystron," *IEEE Transactions on Plasma Science*, vol. 51, no. 3, pp. 802-807, Mar. 2023.

[5] M. Paraliev, S. Dordevic, R. Ganter, C. H. Gough, N. Hiller, R.A. Krempaská, and D. Voulot, "Commissioning and stability studies of the SwissFEL bunch-separation system," in *Proceedings of FEL2019*, Hamburg, Germany, p. 404-407, Aug. 2019.

[6] T. Hara, K. Fukami, T. Inagaki, H. Kawaguchi, R. Kinjo, C. Kondo, Y. Otake, Y. Tajiri, H. Takebe, K. Togawa, T. Yoshino, H. Tanaka, and T. Ishikawa, "Pulse-by-pulse multi-beam-line operation for X-ray free-electron lasers," *Phys. Rev. Accel. Beams*, vol. 19, p. 020703, 2016.

[7] T. Beukers, M. Nguyen, and T. Tang, "Discrete element transmission line beam spreader kickers for LCLS-II," in *2018 IEEE International*

Power Modulator and High Voltage Conference (IPMHVC), Jackson, WY, June 2018.

[8] F. Obier, W. Decking, M. Hüning, and J. Wortmann, "Fast kicker system for European XFEL beam distribution," in *Proceedings of the 39th International Free-Electron Laser Conference*, Hamburg, Germany, p. 353-356, Aug. 2019.

[9] S. Chen, R. Wang, H. Deng, C. Feng, H. X. Deng, X. Fu, and B. Liu, "Design of the beam switchyard of a soft X-ray FEL user facility in Shanghai," in IPAC2018, Vancouver, BC, pp. 4456-4459, May 2018.

[10] R. Zhao, M. Gu, and D. Wang, "A new design of Lambertson magnet with true zero field region," *Phys. Scr.,* vol. 95, p. 065216, 2020.

[11] R. Zhao, M. Gu, and D. Wang, "A new way to improve the main magnetic field uniformity of a Lambertson magnet," *Phys. Scr.*, vol. 94, p. 105804, 2019.

[12] J. Tong and Y. Liu, "Magnetic field analysis and measurement of pulsed septum magnet," *Applied Computational Electromagnetics Society (ACES) Journal*, vol. 38, no. 9, pp. 751-755, Sep. 2023.

[13] Y. Liu, Y. Wu, X. Zhou, and J. Tong, "Design of a pulse transformer for X-band klystron," *Applied Computational Electromagnetics Society (ACES) Journal*, vol. 38, no. 9, pp. 734-740, Sep. 2023.

[14] Y.-F. Liu, M. Gu, Q.-B. Yuan, R. Wang, J. Tong, and S. Li, "Development of a MHz pulsed power supply for kicker magnet in SHINE," *IEEE Transactions on Power Electronics*, vol. 39, no. 4, pp. 4291-4300, Apr. 2024.

[15] Y. Liu, X. Zhou, G. Li, R. Wang, and Q. Yuan, "Design and application of a thyristor-based half-sine pulsed power converter for eddy current septum magnet," *IEEE Transactions on Applied Superconductivity*, vol. 34, no. 8, pp. 1-5, Nov. 2024.

Yongfang Liu was born in Shandong, China, in 1987. He received the Ph.D. degree from University of Chinese Academy of Sciences (UCAS), Beijing, China, in 2020. His research interest includes pulsed power supply and pulsed magnet technologies, such as pulsed klystron modulators, linear transformer drivers (LTD), particle accelerator injection and extraction magnet, particle accelerator beam distribution magnet and irreversible electroporation pulsed power supply.

Jin Tong graduated from the University of Chinese Academy of Sciences, majoring in Nuclear Technology and Application. Since graduation, he has been engaged in the design of pulse magnets and magnetic measurement systems over years, especially for special magnets used in electron beam injection and extraction systems, such as linear/nonlinear kicker magnets, eddy current septum magnets and Lambertson cutting magnets, which had been designed and researched in large scientific facilities.

Sheying Li received her Ph.D. in electrical engineering from Karlsruhe Institute of Technology (KIT), Germany, in 2022. She is currently working in the group of pulse power supplies at Shanghai Advanced Research Institute (SARI), Chinese Academy of Sciences (CAS). Her research interests mainly include photovoltaic technology for water treatment, energy storage technology, energy management control, and dynamic system control for pulsed power supply.

Yizhou Jiang was born in Jiangsu, China, in 1999. He received the master's degree in electrical engineering from Shanghai Electric Power University in 2024. He is working in Shanghai Advanced Research Institute (SARI), Chinese Academy of Sciences (CAS).

Qibing Yuan was born in Sichuan, China, in 1977. He graduated from the University of Science and Technology of China. He received a Ph.D. degree in nuclear technology and applications from Shanghai Institute of Applied Physics, Chinese Academy of Sciences, Shanghai, China, in 2008. He is currently a professor at the Shanghai Advanced Research Institute of the Chinese Academy of Sciences. His research interest focuses on particle accelerator control technology of undulator and pulsed power supply.

Bo Liu received his Ph.D. from Institute of High Energy Physics, Chinese Academy of Sciences in 2005. He is currently a professor at the Shanghai Advanced Research Institute of the Chinese Academy of Sciences. His research interest focuses on particle accelerator based light sources.